Correlating Morphology to Performance in Conjugated Polymer Nanocomposite Thin Films

A Thesis Presented for the
Master of Science
Degree
The University of Tennessee, Knoxville

Siddharth Pradhan
August 2015

Copyright © 2015 by Siddharth Pradhan
All rights reserved.

Acknowledgements

I would like to thank my graduate advisor, Dr. Mark Dadmun (University of Tennessee - Knoxville, UTK) for guiding me through projects and supporting me with patience. Through my association with him, I have learned to value memory, connect dots and have a broader realistic perspective which also helped me in analyzing research problems. I would like to thank Dr. Ilia Ivanov (Oak Ridge National Laboratory, ORNL) for helping me with experimental setup of Electrochemical Impedance Spectrometer, EIS and guidance in my last project. I am also thankful to Dr. Bin Hu and his students for assisting in the current voltage measurements for my second project. I would like to thank the current and previous members in Dr. Dadmun's group (Dr. Huipeng Chen, Dr. Thusitha Etampawala, Halie Martin, Jason Lang, Brad Miller, Cameroon Lee, Sahar Rostam, Dr. Adam Imel, Dr. Leslie Thompson, Edward Duranty, Brian Morgan, Dr. Mehran Tehrani, Tyler McPherson) for helping me in my research (via experiments or discussions). I would also like to thank members in Dr. Ilia Ivanov's group (esp. Dr. Christopher Jacobs, Eric Muckley) for helping me in electrical measurements. I am also grateful to Thomas Malmgreen (UTK), John Dunlop (UTK), Dr. Maulik Patel (UTK) and Pamela Fleming (ORNL) for helping me in various experiments. I would like to thank Dr. Lee Riedinger for providing me support through fellowship and advise. I would also like to thank other faculty members at UTK who had taught me courses and broaden my outlook.

I want to express my gratitude to my father, Pradip Kumar Pradhan and mother, Jayashree Pradhan for providing me with emotional support and love. I would also like to thank my brother, Parth Pradhan for providing me with emotional support and having trust in me. I would like to thank my friends at UTK, Nitilaksh Hiremath, Nitin Kumar, Ravi Kumar, Ramesh Alagesan, Sagar Prasad, Vineet Kumar etc. for their companionship, advises and support. I am also appreciative to my current and previous roommates - Alan Cheehak Yi, Surendranath Somasurdaram for making me feel comfortable at home. I am also obliged to friends outside of Knoxville, Soumitry Jagadev Ray, Rutvij Kotecha, Rajiv Agarwal, Nithin Panicker etc. for their consistent friendship. I am grateful to all the people who had helped me in any possible ways and/or had goodwill for me during the process of finishing my Masters.

Abstract

The morphology and performance of thin films that consist of conjugated polymers and nanoparticles are investigated in this thesis. In the first system, the morphology of the nanocomposite that consists of low band gap alternating copolymers with a methano-fullerene are determined by neutron scattering and correlated to their photovoltaic performance as polymer solar cells. These results show that the conjugated alternating copolymers have high miscibility relative to other conjugated polymers. The analysis of the scattering data shows that the morphology of the conjugated polymer-fullerene bulk heterojunction can be described as the formation of aggregates on two length scales. Important parameters obtained via small angle neutron scattering including correlation length and volume fraction of the aggregates provide insight into the photovoltaic efficiency of film. In addition to role of polymer structure on performance, the impact of post-deposition processing by solvent annealing on the power conversion efficiency of a organic photovoltaic active layer consisting of a low band gap polymer and methano-fullerene was also studied. The impact of solvent quality for both the polymer and fullerene on morphology development in the active layer on the morphology and performance is studied. The results show the system that is annealed in chlorophenol, which is a selective solvent for the fullerene showed a maximum increase in photo-efficiency. The diffusion coefficient of the solvent into these bulk heterojunction was also obtained and optimum time for solvent annealing was deduced. Finally, the possibility of improving the mechanical and barrier properties of the hole transport layer in organic photovoltaic cells has been investigated via addition of clay platelets. The impact of the addition of montmorillonite clay to the conductivity of thin film consisting of PEDOT:PSS and clay was studied. The optimum loading of clay in PEDOT:PSS that improves these structural properties, but does not significantly alter electronic performance is found to be between 5 to 10%. The active layer and hole transporting layer of organic photovoltaic cells have also been investigated through imaging techniques to more thoroughly characterize the morphology and structure of the examined conjugated polymer nanocomposites.

Table of Contents

1 **Introduction** **1**

1.1 Polymer solar cells - - -

4 **Effect of Including Clay in PEDOT:PSS Thin Films on its Structural and Electronic Properties** **50**

4.1 Background - - -

List of Tables

Table 2.1 Density of various low band gap (LBG) polymers used for the study - - - - - - - -20

Table 2.2 Volume fraction of the [6,6]-phenyl-C_{61}-butyric acid methyl ester, PCBM aggregates at the large length scale for the 7 low band gap alternating copolymers - - - - - - -

List of Figures

Figure 1.1 Schematic of a polymeric solar cell - 2

Figure 1.2 Schematic of the charge generation in the bulk heterojunction (BHJ) of polymer solar cell - 3

Figure 1.3 Schematic of photo-induced charge transport process in a band diagram - - - - - - 3

Figure 1.4 Illustrative current voltage characteristics of an organic solar cell - - - - - - - - - - -7

Figure 2.1 Structural units from which novel low band gap polymers (LBG) can be derived - - - - - - - - - - - - - - - - - - -

Figure 3.3 Increase in the mass of a PCPDTBT:PCBM thick film with vapor annealing time on exposure to 1-bromobenzene (BB), 1,2-dichlorobenzene (ODCB), or 2-chlorophenol (CP) solvent vapor - 42
Figure 3.4 Increase in the mass of PCPDTBT:PCBM thick films with vapor annealing time as a result of exposure to BB, ODCB, or CP solvent vapor - - - - - - - - - - - - - - 42
Figure 3.5 UV-Vis (Ultraviolet-Visible) spectra for PCPDTBT:PCBM film solvent annealed in 2-CP vapor -44
Figure 3.6 UV-Vis spectra for PCPDTBT:PCBM film solvent annealed in ODCB vapor - -44
Figure 3.7 Time evolution of the EF-TEM (Energy Filtered - Transmission Electron Microscopy) images of PCPDTBT:PCBM BHJ systems that are annealed in CP and ODCB solvent vapor. The PCPDTBT is blue in these images while the PCBM shows up as yellow -45
Figure 4.1 PSS (Polystyrene Sulfonate) at top and PEDOT (Poly(ethylenedioxythiophene) at bottom in PEDOT:PSS film - 51
Figure 4.2 Schematic of Montmorillonite clay - 52
Figure 4.3 Equivalent circuit for the PEDOT:PSS + clay film - 56
Figure 4.4 Change in PEDOT:PSS film resistance due to variation in clay loading - - - - - -57
Figure 4.5 Change in the charge transfer resistance of PEDOT:PSS film interface with electrode due to variation in clay loading - 57
Figure 4.6 Change in the PEDOT:PSS film capacitance with a variation in clay loading - - 58
Figure 4.7 Change in the double layer capacitance of the PEDOT:PSS film at the film interface with electrode due to variation in clay loading - - - - - - - - - - - - - - - - - 58
Figure 4.8 Change in the exponent corresponding to the phase change, n1 with a change in the loading of clay -59
Figure 4.9 Change in the exponent corresponding to the phase change, n2 with a change in the loading of clay -59
Figure 4.10 (a) Schematic of PEDOT:PSS and clay thin film when viewed from the side (b) and schematic of PEDOT:PSS and clay thin film when viewed from top - - - - - 60
Figure 4.11 Scanning Electron Microscopy (SEM) images of the PEDOT:PSS films containing various clay loading -62

Figure 4.12 X-ray diffraction (XRD) plot of PEDOT:PSS film with 0%,1%,10% and 100% clay loading - - -

Chapter 1

Introduction

1.1 Polymer Solar Cells

It is expected that petroleum based fuels such as oil and gas will be depleted substantially by 2050.[1] Hence, it is crucial to find alternative sources for our energy needs. Solar energy is freely available but a mechanism is required to harvest it directly. Solar energy is a suitable target as the energy contained in 1 hour of solar radiation that strike earth is more than our yearly energy demand.[2] Hence, it is important to develop efficient, cheap and long lasting solar cells to harness this energy, so that it can substitute fossil fuels. Moreover, solar energy offers a non-polluting solution relative to other non-renewable sources of energy. Moreover, silicon based solar cells and other inorganic counterparts have been developed but they don't compete well with thermal power plants or oil and gas as an energy alternative because of their high processing costs.

Instead of inorganic solar cells, low band gap (LBG) polymer-based solar cells have recently become of interest, as they are cheaper[3] and faster[4-6] to manufacture than inorganic solar cells using various techniques. Organic solar cells have high optical absorption coefficients (~10^5 cm^{-1}),[7] are flexible, and as polymer films can be deposited on flexible substrates.[8] Moreover, it is estimated that the photovoltaic efficiency of polymer based solar cells can be increased up to 15%.[9] Despite these promising qualities, polymer solar cells have not yet become commercially viable because of low power conversion efficiency and poor stability. The efficiency of these polymeric solar cells depends on the low band gap polymer type, processing conditions of the solar cell, morphology of the bulk heterojunction active layer and the nature of the interface between layers among other factors.[10] Hence, it is important to understand how the morphology of the active layer (photon absorbing layer) and the charge transporting interfacial layers can be controlled and optimized. The results reported in this thesis are a step towards this goal.

Figure 1.1 depicts a typical polymeric solar cell with an active layer, a hole transport layer (PEDOT:PSS), a cathode (aluminum) and an anode (Indium tin oxide, ITO) in a circuit.

The active layer is a bulk heterojunction in polymer solar cells that consists of a mixture of an electron donor and an electron acceptor. In the most promising polymer based solar cells, the electron donor is a conjugated polymer and the electron acceptor is a functionalized fullerene. This mixture consist of multiple junctions between the donor and acceptor phases. Some polymer solar cells, also incorporate an electron transport layer, such as ZnO or TiO_2, which may also improve light absorption. In Figure 1.2, a model for the morphology of the bulk heterojunction is presented, where two phases are shown with the orange phase representing the conjugated polymer donor phase and the blue phase represents the acceptor phase. Low band gap conjugated polymers act as efficient donors of electrons as they will capture photons which excites an electron, which may dissociate from the polymer to the functionalized fullerene, that often plays the role of electron acceptor. In Figure 1.3, current generation from photon capture is shown in an energy band diagram.

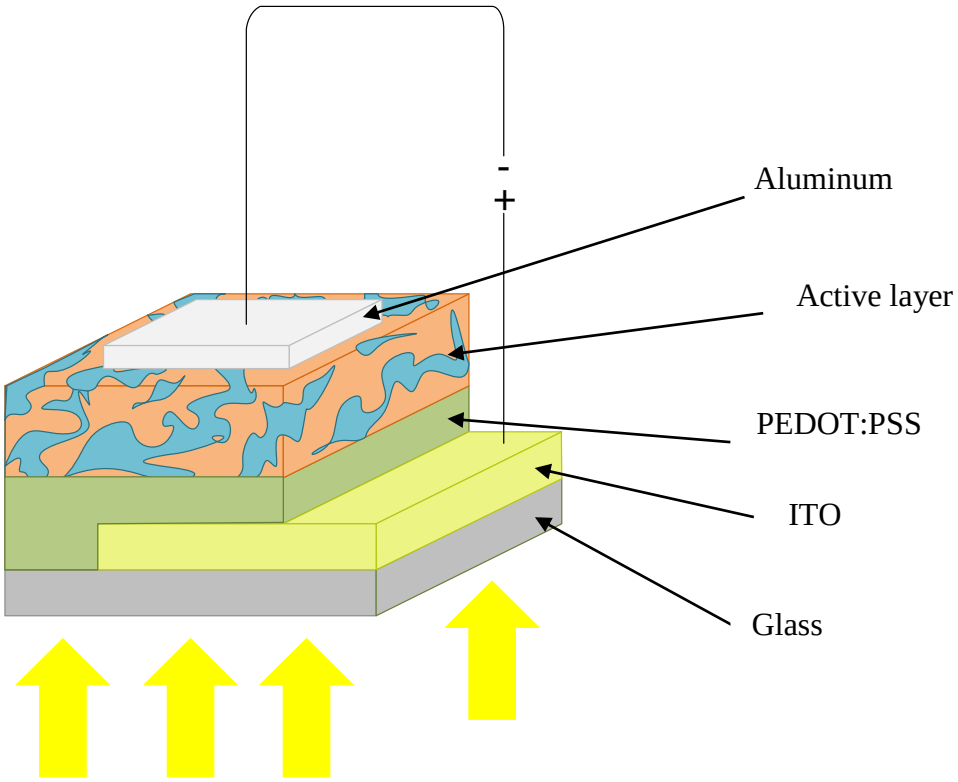


Figure 1.1. Schematic of a polymeric solar cell.

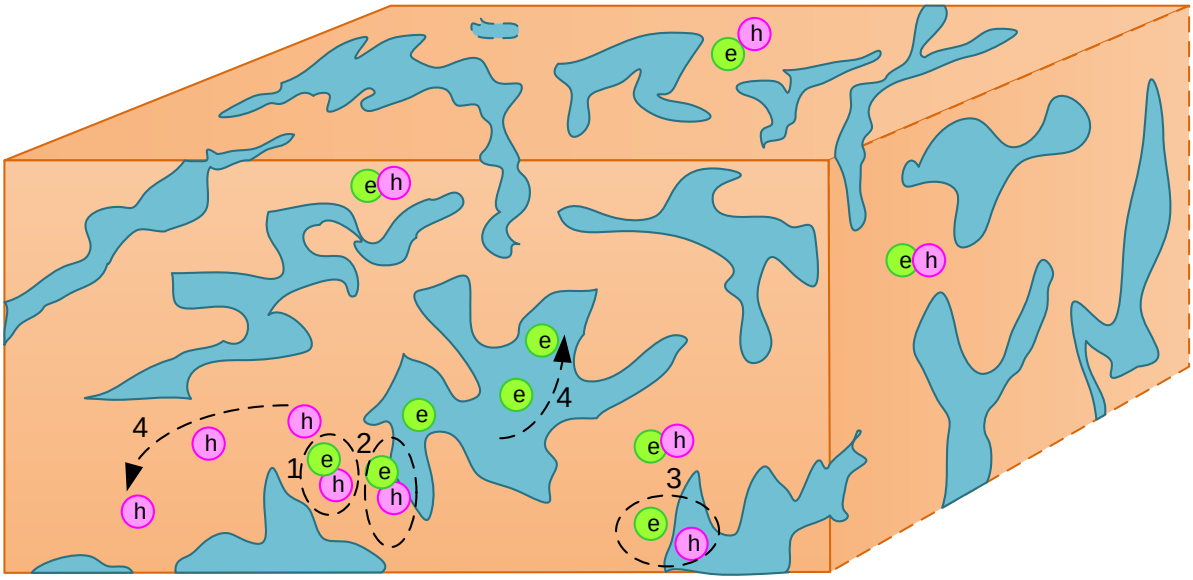


Figure 1.2. Schematic of the charge generation in the bulk heterojunction of polymer solar cell.

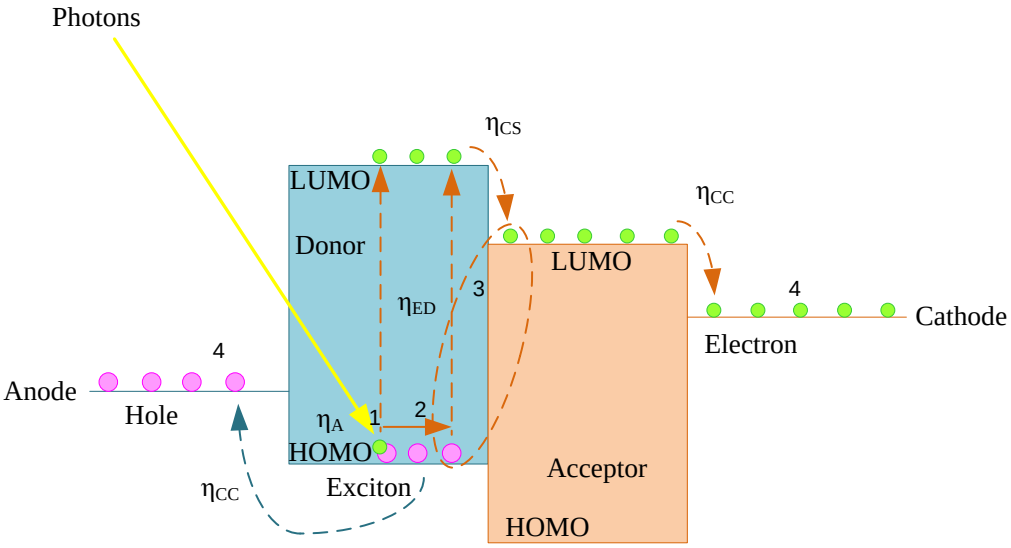


Figure 1.3. Schematic of photo-induced charge transport process in a band diagram.

1.2 Mechanism of current generation and recombination

In a typical polymer solar cell, the process from photons capture to electrons moving in the external circuit can be imagined in four steps. The first step is photon capture, which leads to exciton formation. An incident photon with energy that is larger than the band gap of the polymer will promote an electron from its highest occupied molecular orbital (HOMO) to the lowest unoccupied molecular orbital (LUMO), forming an exciton, which is a bound electron-hole pair. Excitons produced in polymer solar cells have higher binding energy than the thermal energy available at room temperature to dissociate excitons into charges, and thus require additional conditions to dissociate. For instance, the quantum efficiency of charge generation in organic semiconductors is typically in the range of 1%.[11] This low efficiency of exciton dissociation is due to the low dielectric constant of the polymer compared to exciton dissociation in inorganic materials. Therefore, the presence of an electron acceptor with high electron affinity is required to provide a pathway for the exciton to dissociate, i.e. the electron to transfer to the electron accepting fullerene.

In this process, the ratio of generated excitons to incident photons is defined as the absorption efficiency, η_A. The second step in the extraction of an electron in an organic solar cell is the diffusion of the exciton to interface between the donor and acceptor (conjugated polymer and fullerene). Hence, it is important that the electron-hole pair in an exciton doesn't recombine before reaching the donor-acceptor interface. As the exciton diffusion length (~(exciton mobility*exciton lifetime)$^{0.5}$) has been estimated to be around 10 nm,[10] the size of the phase in an efficient organic solar cell's active layer must be 20 nm or smaller. Intuitively, one way to reach this limit would be to have a mixture with a low donor amount that will result in smaller donor domain sizes, which should result in a higher probability of exciton reaching the interface. However, low amounts of donor in the active layer will also results in a decrease in exciton generation. Hence, the ratio between donor and acceptor in the organic solar cell must be optimized, where it has been found that approximately 1:1 wt. ratio of poly(3-hexylthiopehene-2,5-diyl) as donor material and methano-fullerene as acceptor material leads to optimized morphology and photovoltaic efficiency. The efficiency of this step can be quantified by the ratio of the number of excitons that reach the interface and the number of excitons generated i.e. the exciton diffusion efficiency, η_{ED}.

The third step in the extraction of an electron from an exciton is the dissociation of the exciton into a free electron and a free hole, which occurs at the biphasic donor-acceptor interface. The ratio of the number of excitons that dissociate at the interface and the number of excitons that reach the donor-acceptor interface quantifies the efficiency of this step, and is defined by η_{CS}. The final step in this process is the transport of free electrons and holes in the acceptor and donor phase to the electrodes generating electrical current. Free electrons and holes transport with the acceptor and donor phases, respectively, with the aid of an internal electric field that is created by the use of electrodes with different work function. Additionally, free electrons and free holes may recombine at a donor-acceptor interface before reaching the electrodes. The ratio of charges that are collected at the electrode to the number of free charges that are generated quantifies the efficiency of this process and is defined by the charge carrier collection efficiency, η_{CC}. The external quantum efficiency, η_{EQE}, is defined as the ratio of number of electrons collected by the solar cell to the total number of photons of a given energy (or wavelength) incident on the solar cell. Mathematically, this is a product of the efficiency of the four steps in the process

$$EQE(\lambda) = \eta_A(\lambda) * \eta_{ED}(\lambda) * \eta_{CC}(\lambda) * \eta_{CS}(\lambda) \quad (1.1)$$

All the four steps involved in current generation is shown in Figure 1.2 and Figure 1.3. In addition to limited photon capture and energy level mis-alignment, various kinds of recombination are possible in polymer solar cells leading to further reduction in the power conversion efficiency. These include the relaxation of excitons that fail to diffuse to an interface, the recombination of geminate pairs formed at the interface which fail to fully dissociate and the recombination of dissociated carriers generated by different absorption events (non-geminate recombination). Non-geminate recombination processes includes the recombination of charges at the wrong electrode (surface recombination) or in the bulk. These recombination processes may occur via both the Langevin and Schokley-Reed-Hall mechanisms. Previous results have shown that from short circuit conditions to maximum power point, geminate recombination dominates whereas from the maximum power point to open circuit condition (high charge density), non-geminate recombination (bimolecular recombination) losses dominate.[12, 13] Charge separation rather than their extraction is suggested as a process to outcompete geminate recombination in a solar cell.[14] A very good review of charge transport and recombination in polymer based solar cells can be found in references [15, 16]. Bimolecular recombination will occur during step 4

whereas monomolecular recombination will occur at step 2 in Figure 1.2. Both the electron and hole mobility in the two materials should be high (>10^{-4} $cm^2V^{-1}s^{-1}$) and balanced to prevent the build-up of charge.[17]

1.3 Current Voltage Characteristics

Current-voltage measurement is a crucial test to monitor solar cell performance. Typical characteristics of the current-voltage measurement is shown in Figure 4. In this Figure, the open-circuit voltage, V_{OC} is related to the energy difference between the LUMO level of the acceptor and the HOMO level of the donor.[11]

$$V_{OC} = \frac{(|E_{HOMO}^{Donor}| - |E_{LUMO}^{PCBM}|)}{e} - 0.3V \tag{1.2}$$

Hence, it is preferred to have a donor (i.e. conjugated polymer) with a low band gap, which will increase the absorption of the solar radiation while such a donor polymer will result in high difference between its HOMO and the LUMO of the acceptor. The short circuit current density, J_{SC} is equal to the integral of the product of the cell response and the incident solar spectral irradiance as shown below.

$$Jsc = q \times \int \eta EQE \times S(\lambda) \times d\lambda \tag{1.3}$$

For organic photovoltaics, the maximum electrostatically allowed photocurrent that can be extracted is given by:

$$J_{SC} = q\left(\frac{9\varepsilon_0\varepsilon_r \mp_h}{8q}\right)^{1/4} G^{3/4} V_0^{1/2} \qquad [16] \tag{1.4}$$

where G is the generation rate of excitons, $\mp_h$ is the hole mobility, $\varepsilon_0\varepsilon_r$ is the dielectric permittivity of the film and V_0 is the compensation voltage. V_0 is slightly higher than V_{OC} and increases as V_{OC} increases. The overall photocurrent is given by

$$J_{ph} = eGL\left(\frac{k_D(\frac{V_{eff}}{L})}{k_D(\frac{V_{eff}}{L}) + k_F}\right)\left[\coth\left(\frac{eV_{eff}}{2kT}\right) - \left(\frac{2kT}{eV_{eff}}\right)\right] \qquad [18] \tag{1.5}$$

where this equation is the product of three terms: (1) the saturated photocurrent term (eGL), (2) the probability of charge separation at the donor-acceptor interface $\left(\frac{k_D(\frac{V_{eff}}{L})}{k_D(\frac{V_{eff}}{L}) + k_F}\right)$ and (3) the Sokel-Hughes term for charge extraction $\left[\coth\left(\frac{eV_{eff}}{2kT}\right) - \left(\frac{2kT}{eV_{eff}}\right)\right]$. L is active layer thickness, k_D

is the electric-field dependent rate of charge separation in electron-hole pairs, k_F is recombination rate, and V_{eff} is the effective applied voltage.

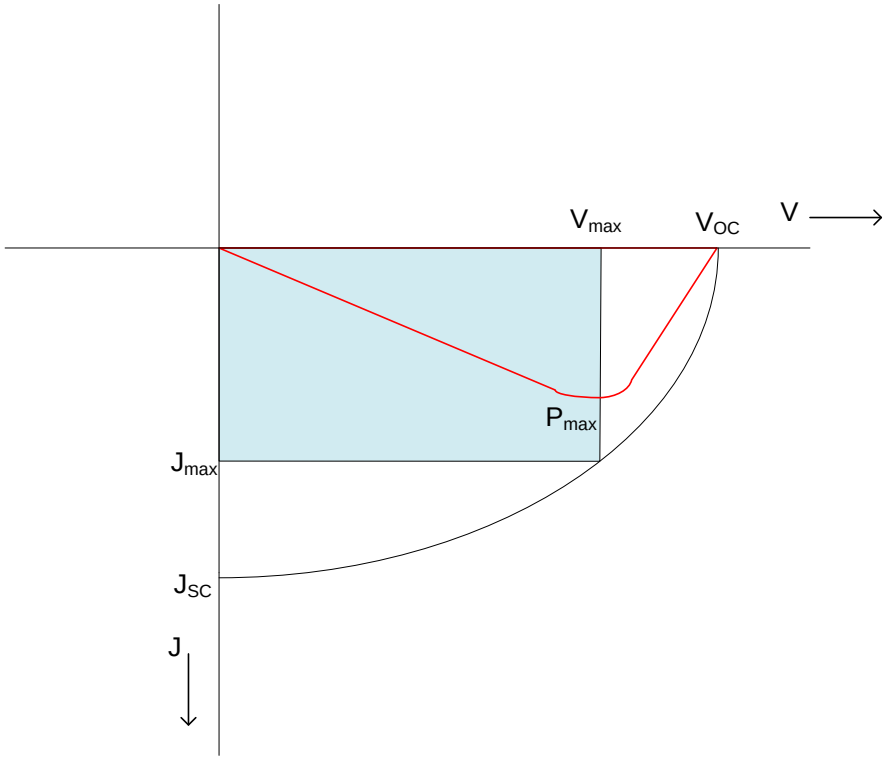


Figure 1.4. Illustrative current voltage characteristics of an organic solar cell.

In polymer based solar cells, an increase in the interfacial surface area between the polymer and fullerene increases the area available for exciton dissociation, which, in turn, leads to higher current. Another important characteristic of the solar cell that can be extracted from the current-voltage curve is the Fill factor, which is the ratio of V_{max}*J_{max} defined by the maximum power point, P_{max} and the product of open circuit voltage and short circuit current, V_{OC}*J_{SC}. It has been found that close π–π interplanar spacing and polymeric arrangement at the electrode surface where with π face of the polymer lying flat on the electrode results in higher fill factor.[19]

The power conversion efficiency, η of a given organic solar cell is this defined as:

$$\eta = ((J_{SC} * V_{OC} * FF)/P_{in}) * 100 \quad (1.6)$$

V_{OC} may be limited by the fullerene bandgap and non-fullerene acceptor materials are under development to achieve voltages beyond 1 V. For conjugated polymer-fullerene active

layers, the voltage cannot be raised above ~1 V because of insufficient driving force for hole transfer leading to increased recombination of excitons on the fullerene. It has been found that when I_{SC} rises, V_{OC} decreases. Hence, it is important to target an optimized system with high V_{OC}, high I_{SC} and FF to get high power conversion efficiency.[16]

1.4 Bulk Heterojunction (BHJ) Active Layers

The active layer is an important aspect in any solar cell, as this is where photon absorption creates an electron. Most polymer based solar cells are based on the bulk heterojunction concept, where a bulk heterojunction is a mixture of donor acceptor materials with randomly distributed interfaces ("heterojunctions") throughout the film. The photovoltaic performance of an active layer based on a bulk heterojunction can be improved by using conjugated polymer with an optimized band gap and energy level alignment[11, 20] with the acceptor to increase photon capture and open circuit voltage. The performance of the BHJ may also be improved by increasing the miscibility of donor and acceptor[21, 22] as the increased miscibility will increase the interfacial area between the two phases to increase exciton dissociation. An ideal donor polymer in a BHJ should have a high extinction coefficient and high hole mobility.

The morphology of the donor-acceptor bulk heterojunction also plays a key role in its efficiency. More interfaces between donor and acceptor phases results in an increase in charge generation. Therefore, an ideal morphology of BHJ devices has been historically imagined as a nanoscale phase separated structure with domains that are less than the width of exciton diffusion length (~ 20 nm) that are interconnected with similar acceptor domains to provide percolation pathways for electron and hole transport.[23, 24] However, it has been found that the morphology of bulk heterojunction is not as simple as this model. There appear to exist at least three phases, which consist of an amorphous mixed polymer phase that contains fullerene (miscible phase), a pure fullerene phase and pure crystalline polymer phase.[25-27] Higher ordering of the polymer via $\pi-\pi$ stacking results in an increase in hole mobility. Hence, higher polymer crystallinity is desirable. However, highly crystalline polymers are difficult to process and PCBM will be less miscible in such polymers. Hence, a balance between PCBM miscibility, polymer crystallinity

and continuous pathways is needed to create a morphology that can perform efficiently as an organic photovoltaic active layer.

The formation of this morphology often requires physical processing of BHJ post film deposition, as this processing can guide its morphology,[28, 29] control the aggregation of the donor and acceptor molecules[30, 31] and induce crystallinity in the polymer.[32] The active layer morphology can be modulated by varying the monomer structure by altering the characteristics of the backbone or side chains,[11, 33] by varying the solvent from which the film is deposited,[34, 35] by using appropriate solvent additives in the solution prior to deposition,[36] by changing the ratio of polymer and fullerene,[37, 38] or treatment of the film after deposition. Post deposition treatments include thermal annealing[27] and solvent annealing[36, 38, 39]. Connecting morphological parameters of the bulk heterojunction, such as the surface to volume ratio, domain size, polymer crystallinity, domain size and composition to overall photovoltaic characteristics of the organic solar cell is important to guide the synthesis of novel polymer and improve the processing of BHJ active layers to ensure better physical and chemical behavior of the resultant solar cell. The optimum nanoscale morphology of the active layer must be a balance between a large interfacial area and continuous pathways available for charge transport.[24]

1.5 Materials

Donor materials: Among polyalkenes, polyacetylene is a conjugated polymer with a low band gap (1.5 eV), though aromatic conjugated polymers are more popular as they tend to be more easily processed. It has been seen that in polyacetylene, the band gap decreases with a decrease in bond length whereas in aromatic conjugated polymers, band gap decreases as quinoid character increases.[40] In aromatic conjugated polymers, thiophene and benzene are the most common aromatic donor units. The thiophene unit has a higher electron donating ability than benzene, and more delocalization and planarity compared to the benzene unit.[41] Combination of the thiophene unit, the benzene unit and an electron withdrawing or electron donating group on the same polymer chain can provide a mechanism to control the electron rich or electron poor units in the conjugated polymer. Among aromatic conjugated polymers, the alkylthiophenes and poly(p-phenylene vinylene)s are the most commonly studied systems e.g. Poly(3-hexylthiophene-2,5-diyl) (P3HT), Poly[2-methoxy-5-(2-ethylhexyloxy)-1,4-phenylene

vinylene](MEHPPV), Poly[2-methoxy-5-(3′,7′dimethyl octyloxy) -1,4-phenylene vinylene] (MDMO-PPV).[16]

Acceptor materials – The most commonly used materials for acceptors are fullerene and its derivatives. The most common example is [6,6]-phenyl-C_{61}-butyric acid methyl ester (PC61BM), with [6,6]-phenyl-C_{71}-butyric acid methyl ester ($PC_{71}BM$) and indene-C_{60} bisadduct (ICBA) as two additional fullerenes that have been studied as electron accepting molecules in bulk heterojunction active layers.

1.6 Goals and Overview

The motivation behind our research work is to correlate the morphology of thin films based on conjugated polymer nanocomposites to their performance in photovoltaics and electrical conduction. The relation between morphology of photovoltaic films based on low band gap alternating copolymer and their performance is still poorly understood. Moreover, the change in percolation pathways in thin films consisting of conducting polymer due to varying clay loading has not been explored. Therefore, next three chapters (Chapters 2, 3 and 4) in this research work involves projects with following aims.

1. Investigating morphology of thick films based on a mixture of various kinds of low band gap alternating copolymer and fullerene and correlating structural parameters with the photocurrent induced.
2. Correlating the development of morphology of thin films based on a specific alternating copolymer and fullerene due to solvent exposure with photovoltaic performance.
3. Probing the change in resistance of thin conducting film as a result of clay inclusion and associate it with change in film morphology.

Chapter 2 introduces a morphological model based on available data and predicts photocurrent generation and interacting forces between alternating copolymer and fullerene. Chapter 3 measures diffusion coefficient of various solvent vapors in a bulk heterojunction film and relate it with the photovoltaic performance and structural studies. Finally, chapter 4 introduces a model to explain the electrical behavior of a conducting film as a result of varying humidity and clay loading which is further corroborated via structural analyses.

Chapter 2

Correlating the Morphology of Low Band Gap Conjugated Polymer based Bulk Heterojunctions to Photovoltaic Performance

2.1 Background

Among low band gap (LBG) polymers, push-pull copolymers with alternating electron rich and electron deficient units have been identified as effective donors in organic photovoltaic active layers[20]. Coupling the electron rich unit with an electron poor unit reduces the band gap, where the electron rich unit usually consists of benzene and thiophene units or their combination. Structural units that compose the conjugated polymer are most often derived from dibenzene and dithiophene units, and can be categorized into three parts dibenzene bridged units, dithiophene bridged units and thiophene-benzene fused units. The dibenzene-based monomers are two benzene units bridged by a carbon, silicon or nitrogen atom as shown in Figure 2.1 and are the weakest donors.

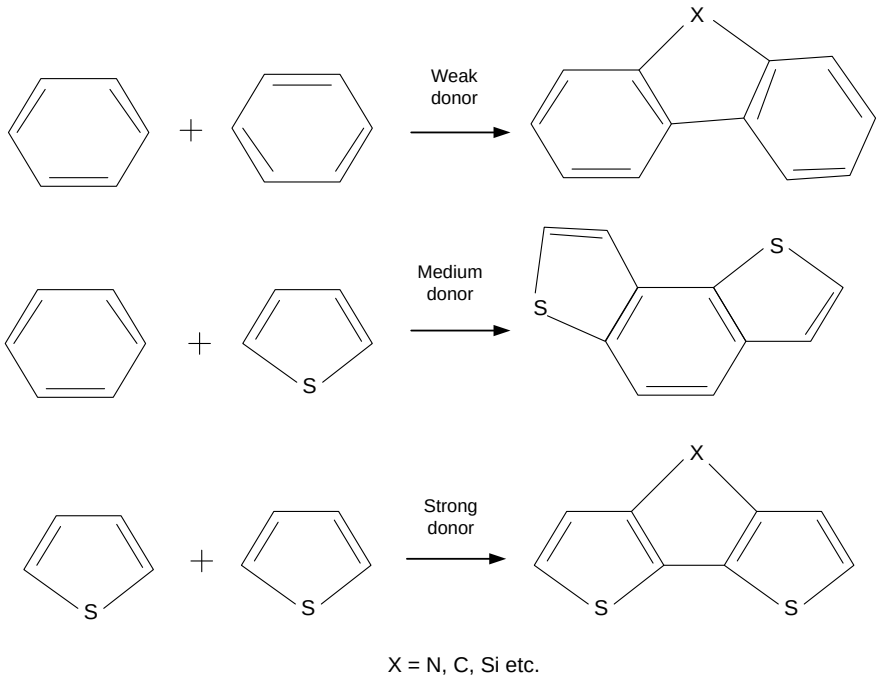


Figure 2.1. Structural units from which novel low band gap polymers can be derived.

Due to the electron deficient nature of the benzene unit, they are the weakest donors. Polymers based on these donor units have low lying HOMO energy levels and hence high V_{OC}. Similarly, two thiophene units can be bridged to give a donor, as shown in Figure 2.1. Donor units based on dithiophene units have strong orbital mixings with electron poor unit and produce push-pull copolymers with higher planarity relative to dibenzene units. Donor-acceptor polymers based on benzene have poor orbital mixing and hence higher bandgap and low J_{SC}. The reverse is true for thiophene based polymers. Effective acceptor units in these polymers will contain electron withdrawing groups such as an imine group -C=N (e.g. benzothiadiazole unit), a carbonyl group -C=O (e.g. a thieno[3,4-c]pyrrole-4,6-dione unit). The electron accepting property of the acceptor units in the polymer can be determined by measuring their LUMO energy levels, where a lower LUMO level translates to a stronger electron acceptor.[41]

Push-pull conjugated polymers have attracted significant interest as donor materials in organic photovoltaic active layers as their intrinsic optical and electronic properties can be readily tuned by controlling the intramolecular charge transfer from the electron rich (or donor) unit to electron poor unit (acceptor) within the polymer chain. As indicated in Figure 2.2, the HOMO(LUMO) of the donor (D) unit of the polymer interacts with the HOMO(LUMO) of acceptor (A) unit of the polymer to generate two new molecular orbitals upon formation of the covalent bond or molecular orbital hybridization. As a result, the band gap is reduced.[20, 42] The performance of such polymers in organic solar cell active layers can be further modulated by varying the monomer structure on the backbone or side chains.[11, 33]

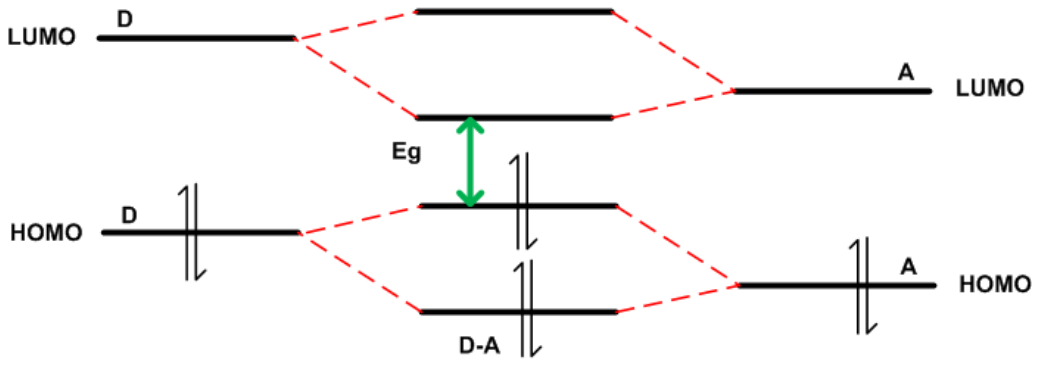


Figure 2.2. Molecular orbital interaction of donor and acceptor units in push-pull conjugated copolymers.

Hence, the V_{OC} of the active layer can be modulated by varying the structure of the conjugated polymer for a given fullerene. However, the J_{SC} varies with the choice of conjugated polymers and acceptor combination or by tuning the morphology of the resultant BHJ. This is because tuning the morphology of the BHJ will impact the exciton extraction and hence J_{SC}. Therefore, a study that correlates the chemical structure of LBG alternating copolymer with the morphology of its bulk heterojunction with PCBM has been completed, where the results are described below and correlated to photocurrent generation, where applicable.

2.2 Polymer design and properties

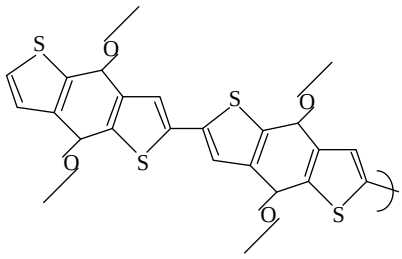
In this project, the morphology of bulk heterojunctions that consist of a series of LBG polymers with PCBM were examined and their monitored by small angle neutron scattering. Seven low band gap alternating copolymers have been studied. The monomer units of each polymer have an electron rich unit, few side chains and may or may not have an electron poor unit. Therefore, a comparative study of impact of electron rich unit, electron poor unit and side chain on the resultant BHJ active layer morphology is crucial in understanding the correlation between conjugated polymer structure, active layer mixing behavior and photovoltaic performance. As shown in Figure 2.3, the electron rich units used for this study are benzodithiophene (BDT) and bis-benzothiophene (BBDT). The electron poor units that have been examined in these low band gap copolymers are cyclopentathiophenedione (CTD), thienoisoindoledione (TID) and thienopyrroledione (TPD). The side chains that have been used are ethylhexyl (EH) and a linear dodecane (C12). Each of these units and the polymers made from them are shown in the Figure 2.3.

Relative to their performance, the Benzodithiophene (BDT) containing polymers have exhibited high power conversion efficiency in previous studies.[43-46] This has been attributed to the fact that the BDT has a larger more planar conjugated structure, can readily stack by formation of π-π bonds, which results in very high mobility.[47] Polymers with the BBDT unit have high thermal stability and hole mobility.[48] The presence of the TPD unit in the polymer imparts rigidity to the polymer, but also has improved solubility and open circuit voltage in the resultant BHJ.[49, 50] Because of these favorable characteristics, there have been quite a few studies on the performance of polymer solar cells that contain TPD based polymers.[50-55] The inclusion of the TID unit in the polymer also imparts good solubility and thermal stability.

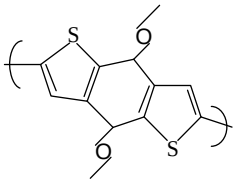
2.2.1 Polymers used for this study

Figure 2.3. Illustration of molecular structure of various low band gap polymers and their constituent units.

Electron rich unit

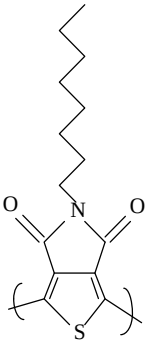


BBDT

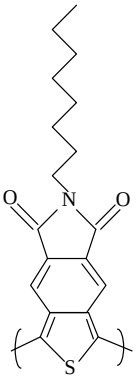


BDT

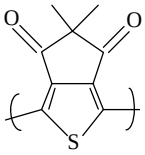
Electron poor unit



TPD

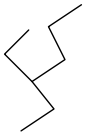


TID

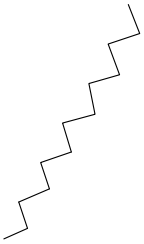


CTD

Side chain unit



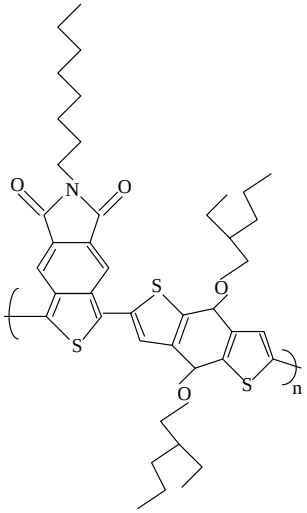
EH



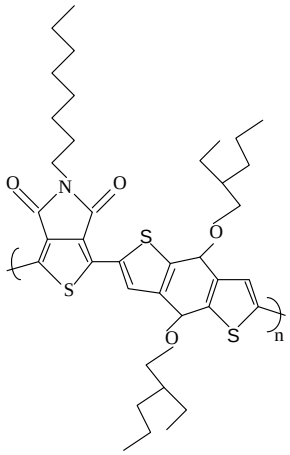
C12

Polymers made of the monomer consisting of combination of above mentioned donor and/or acceptor and side chains.

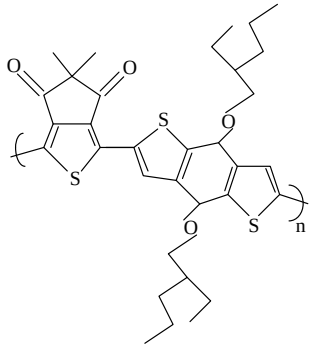
Figure 2.3 continued



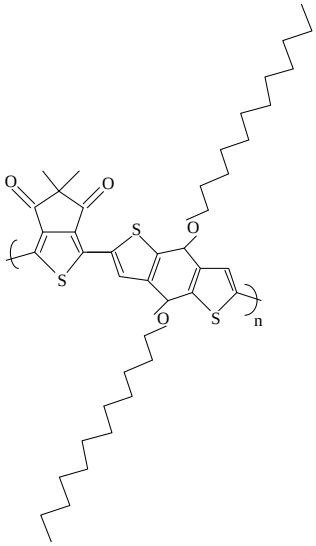
P-TID-BDT(EH)



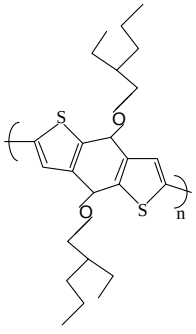
P-TPD-BDT(EH)



P-CTD-BDT(EH)

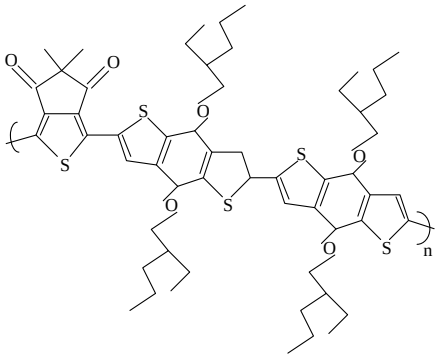


P-CTD-BDT(C12)

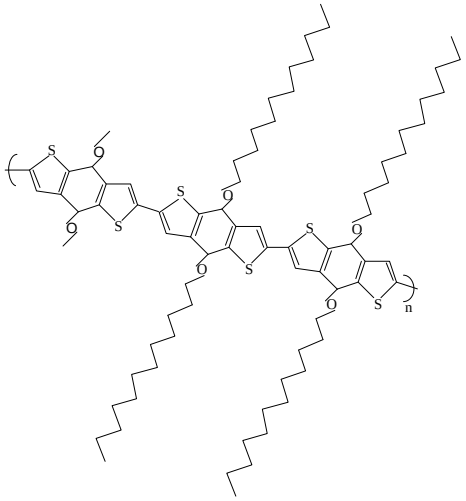


P-BDT(EH)

Figure 2.3 continued



(P-CTD-BBDT(EH))



P-CTD-BBDT(C12)

Figure 2.3 continued

Organic solar cells that are based on conjugated polymers that contain the TID unit exhibit improved short circuit current and fill factor relative to those that contain the TPD unit, but these cells usually exhibit lower power conversion efficiency TPD based solar cells, because of a lower V_{OC}.[56] The CTD moiety has only been identified as a potential donor recently,[57] so there are fewer studies of these materials. The impact of the presence of the side chain on the polymer on the performance of the resultant solar is also of interest as the side chain will impact the solubility of polymer in solvent and its packing behavior in the bulk. This translates to modification in the electron and hole mobility, and photovoltaic performance of the resultant active layer.[58-60] A shorter side chain favors higher hole mobility, as it will allow better packing of the polymer. A branched side chain inhibits π-π stacking, and thus limits the polymeric ordering that usually translates to improved hole mobility.

2.3 Morphology of the Bulk Heterojunction

Important morphological characteristics of the bulk heterojunction, including domain size, amount of interphase surface area, and composition of the coexisting phases can be determined using small angle scattering techniques. X-ray scattering does not provide sufficient contrast between a conjugated polymer and fullerene to complete a full analysis of the BHJ morphology, because of similar atomic content of the polymer and the methano-fullerene. Neutron scattering, on the other hand, provides sufficient contrast between the polymer and fullerene. The large difference in neutron scattering length density of the hydrocarbon based polymer and the PCBM stems from the paucity of hydrogen on the fullerene. Hence, small angle neutron scattering method was used to determine the important morphological characteristics of bulk heterojunction that consist of low band gap conjugated polymers and PCBM. Other imaging techniques e.g. Atomic Force Microscopy and Transmission Electron Microscopy have been used to provide qualitative information about the phase separation[43, 53, 56, 61, 62] in active layers based on these low band gap polymer, however neutron scattering provides improved resolution and detail of the phase separated structure of the resultant conjugated polymer-fullerene mixture.

2.4 Experiments

Materials - [6,6]-Phenyl-C_{61}-butyric acid methyl ester (PCBM > 99.5%) was purchased from Sigma-Aldrich, and seven low band gap alternating copolymers namely P-BDT(EH), P-CTD-

BDT(EH), P-CTD-BBDT(EH), P-TPD-BDT(EH), P-TID-BDT(EH), P-CTD-BDT(C12) and P-CTD-BBDT(C12) were procured from the group of Dr. Nikos Kopidakis, NREL (National renewable energy laboratory). PCBM and low band gap polymers were mixed in 1:1 ratio by weight and dissolved in dichloromethane such that the solid composition is ~10 wt %. Solutions were then deposited dropwise on 11 mm diameter quartz disk windows. This procedure yielded films that were ~0.7 mm thick on top of quartz windows.

Small angle neutron scattering - The small angle neutron scattering (SANS) patterns of these samples were obtained on the General purpose SANS instrument at the High Flux Isotope Reactor at the Oak Ridge National Laboratory. The SANS data for thermally annealed samples were also obtained on same instrument. The samples were thermally annealed for 20 min at 160 °C. A neutron wavelength of 4.72 Å was used and two sample to detector distances of 1.7 m and 18.5 m were used to provide a q range from 0.00285 up to 0.54 $Å^{-1}$, where $q = (4\pi \sin\theta/2)/\lambda$, where λ is the neutron wavelength and θ is the scattering angle. The raw data were corrected for scattering from the empty cell, detector dark current, and detector sensitivity. The corrected data were then normalized to an absolute intensity using a Porasil-A standard. The contribution from incoherent scattering and thermal density fluctuation was eliminated yielding the absolute coherent scattering.

Density measurement - The scattering length densities of the LBG alternating copolymers were determined using the atomic composition of the polymer and their density,[63] which was measured using pycnometer. The densities of the low band gap polymers were determined using a gas displacement pycnometer, model 1340 Accupyc pycnometer. The densities of the LBG alternating copolymers are presented in Table 2.1 along with densities of P3HT and PCBM as reference.

2.5 Structural Model of BHJ Morphology

The structural model that is used to analyze the SANS data includes PCBM clusters at both large (meso) length scales as well as at small (nano) length scales, which is illustrated in Figure 2.4. This model is used as the scattering data itself could not be adequately fit to a model that contains PCBM clusters on only one of these length scales. The scattering data were thus fit using two Debye Anderson Bueche (DAB) models,[64, 65] one for each length scale. The large length scale corresponds to approximately 800-2100 Å, while the small length scale corresponds

Table 2.1. Density of various low band gap alternating copolymers used.

Materials	Density (g/cm^3)
P3HT	1.1[66]
PCBM	1.5[21]
P-TPD-BDT (EH)	1.502
P-BDT(EH)	1.414
P-CTD-BDT(EH)	1.518
P-CTD-BBDT(EH)	1.447
P-CTD-BDT(C12)	2.075
P-CTD-BBDT(C12)	1.394
P-TID-BDT(EH)	1.574

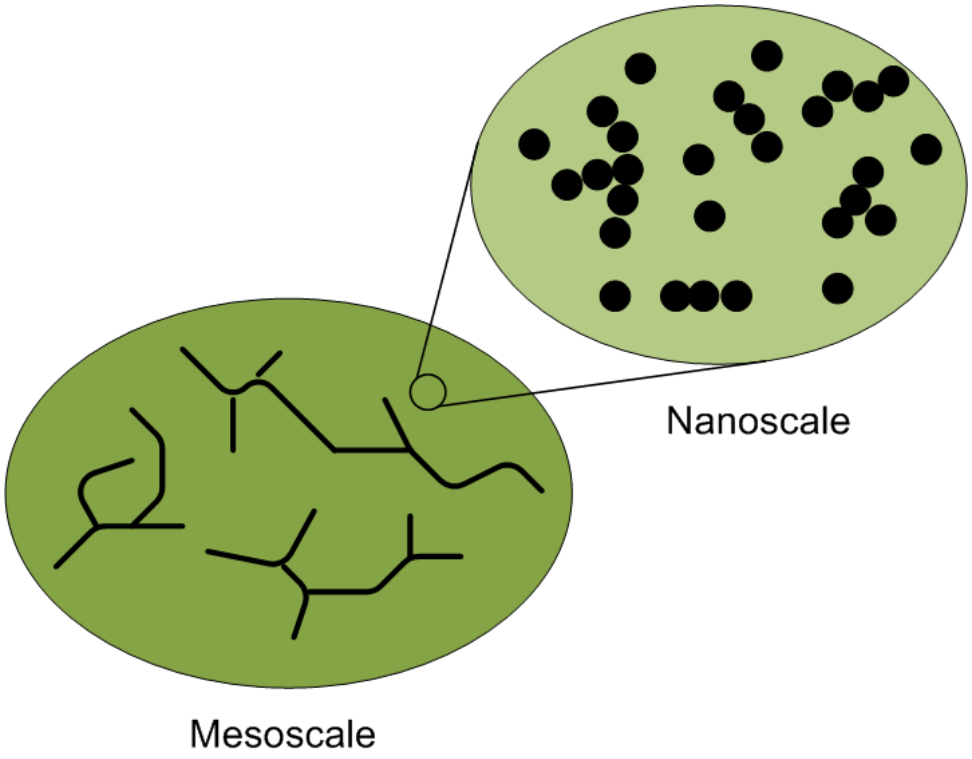


Figure 2.4. Figure illustrating scaling model that describes the morphology of the low band gap PCBM active layers. Black dots represent individual PCBM molecule at small length scale which may combine to form smaller clusters. At large length scale, black network structure shows PCBM clusters interconnected into large networks.

to approximately 30-210 Å. At the large length scale, the model consists of 2 phases, where the dispersed phase consists of a pure PCBM aggregated phase and the continuous phase consists of a miscible mixture of the conjugated polymer and fullerene. The structural information that is garnered from the model at small length scales provides information on the dispersion of the PCBM within the large length scale miscible phase, as illustrated in Figure 2.4.

Fits of the scattering data to the DAB model for the large length scale (low q) is shown in Figure 2.5, while the fits of the data at small length scales (high q) is shown in Figure 2.6 for the BHJ with the polymer P-BDT(EH). In both Figures, m1 is the scale factor for the fit, which is equal to $8\pi(\Delta SLD)^2\varphi(1-\varphi)$, where φ is the volume fraction of the PCBM aggregate, ΔSLD is scattering length density contrast between the two phases. Similarly, m2 is the correlation length, ξ, of the phase separated structure, which is a measure of the average spacing between two phases. In both Figures 2.5 and 2.6, the scattering curves for the as-cast and thermally annealed films are present. SANS fits for other low band gap alternating copolymers studied is present in Appendix (Figure A1 - A12). As can be seen in Figures 2.5 and 2.6, there is very little change in the structure of the film with annealing, an observation that is true for all of the polymers studied. As previously mentioned, many low band gap polymers do not exhibit a measurable glass transition temperature,[67] which means that this thermal annealing protocol does not provide the BHJ components the required mobility to evolve to a more thermodynamically stable structure. Therefore, the results of the analysis is only presented for the as cast data.

The volume fraction of PCBM in the miscible phase and the volume fraction of the PCBM aggregates at both length scales are determined from the fit of the scattering data to the DAB model. In this analysis, any crystalline polymer that exists is included in the miscible phases, where this assumption is based on the absence or limited presence of a crystalline peak in the scattering data. Moreover, the difference between the scattering length density contrast (ΔSLD) of the crystalline polymer with PCBM to that of the amorphous polymer is only ~ 10%[68] because ΔSLD ~ mass density, ρ. Hence, the presence or absence of polymer crystallinity will only modify the reported results negligibly. The ultimate results of this assumption is that the actual mixing of PCBM at both length scales will be little less than that which is reported at both length scales.

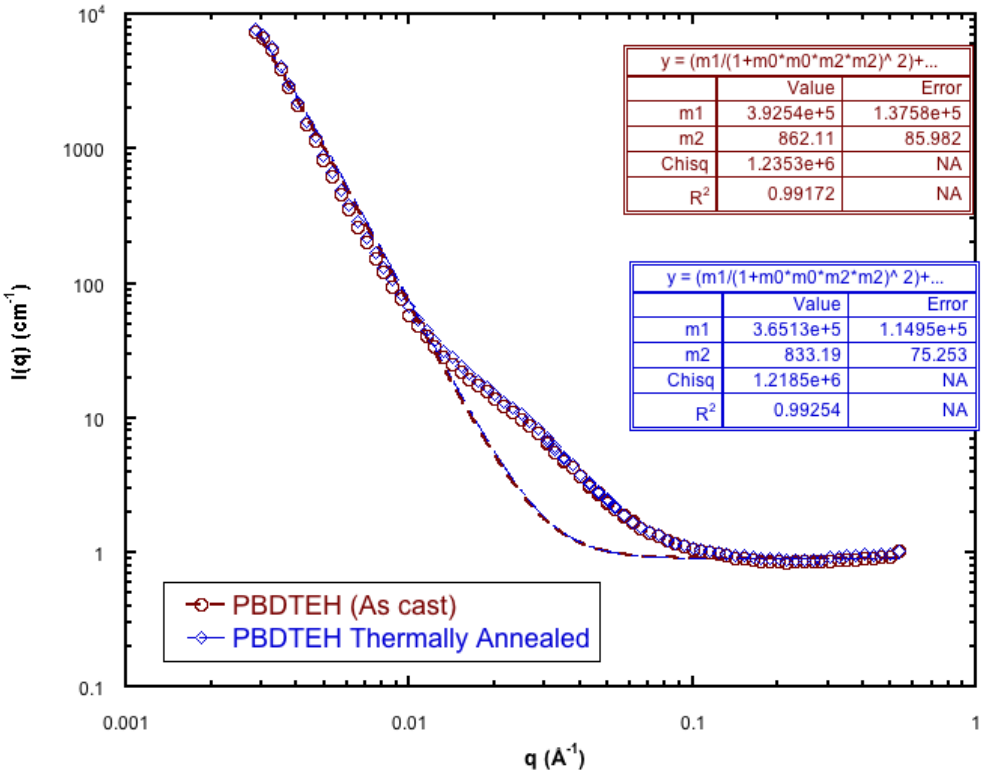


Figure 2.5. Fit of the scattering data of P-BDT (EH) to the DAB model at the global length scale of the phase separated bulk heterojunction.

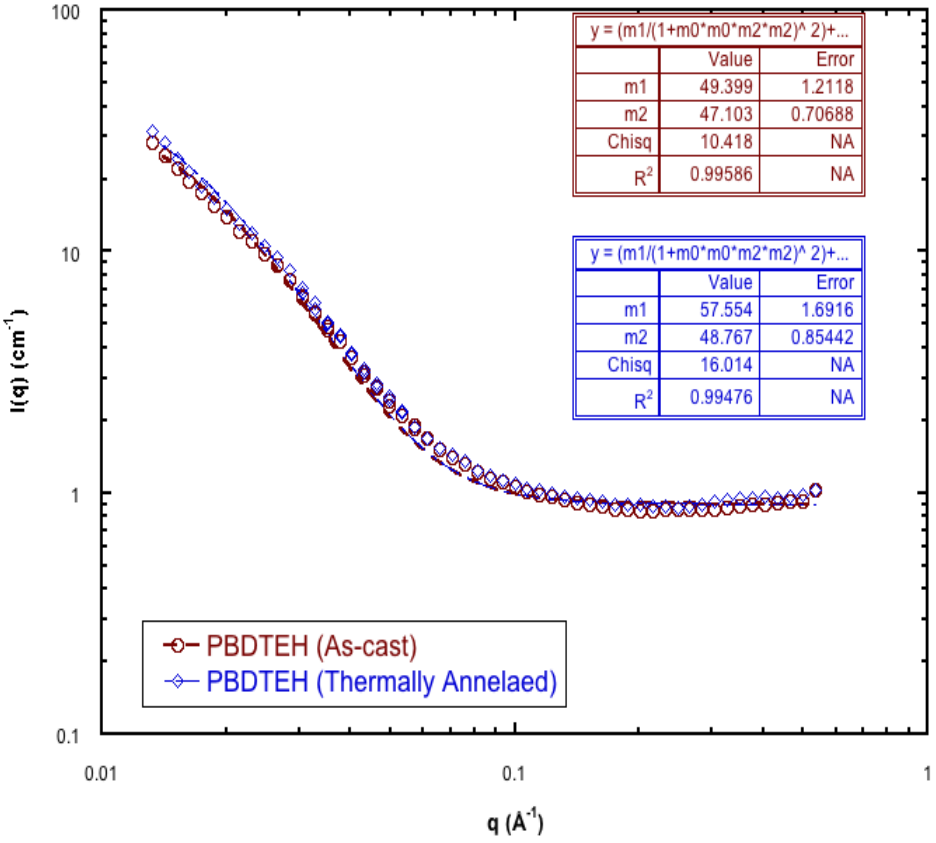


Figure 2.6. Fit of the scattering data of P-BDT (EH) to the DAB model at the local length scale of the phase separated bulk heterojunction.

2.5.1 Formalism to determine morphology parameters

The formalism to determine the volume fraction of the PCBM aggregates and the volume fraction of PCBM in the miscible phase at both length scales from the parameters that are derived from the fitting of the scattering data to the DAB model is described below. In this analysis, let the volume fraction of PCBM be φ_1 at large length scales (low q). Then, the volume fraction of the miscible phase at this length scale is 1- φ_1. Let the volume fraction of PCBM in the miscible phase at low q be $\varphi_{1,m}$. At small length scales (high q), let the volume fraction of PCBM be φ_2. Then, the volume fraction of the miscible phase at this length scale is 1- φ_2. Further, let the volume fraction of PCBM in the miscible phase at small length scales be $\varphi_{2,m}$. With these definitions, and the model shown in Figure 2.4, the volume fraction of the PCBM aggregates at the small and large length scales, the interfacial area between phases, and the

volume fraction of PCBM in the mixed phase at both large and small length scales and distance between PCBM molecules in the miscible phase can be determined from the parameters that evolve from the fits of the scattering data to the DAB model as explained below.

Mass Balance Equations

1) Mass of PCBM = Mass of polymer (as the weight ratio in the sample is 1:1)

Let the volume of the PCBM aggregates be V_1 and the volume of the miscible phase be V_2. Hence,

$$V_1(\rho_{PCBM}) + V_2(\varphi_{1,m})(\rho_{PCBM}) = V_2(1-\varphi_{1,m})(\rho_{polymer})$$

Dividing this equation by $(V_1 + V_2)$, we get

$$\varphi_1(\rho_{PCBM}) + (1-\varphi_1)(\varphi_{1,m})(\rho_{PCBM}) = (1-\varphi_1)(1-\varphi_{1,m})(\rho_{polymer}) \quad (2.1)$$

2) In the model, the mass of PCBM in the miscible phase at low q is equal to the mass of PCBM that is in the in miscible phase at high q and mass of PCBM aggregates at high q. So,

$$V_2(\varphi_{1,m})(\rho_{PCBM}) + V_2(\varphi_2)(\rho_{PCBM}) + V_2(1-\varphi_2)(\varphi_{2,m})(\rho_{PCBM})$$

Dividing this equation by $V_2(\rho_{PCBM})$, we get

$$\varphi_{1,m} = \varphi_2 + (1-\varphi_2)(\varphi_{2,m}) \quad (2.2)$$

Scale Factor Equations

The fitting of the scattering data to the Debye Anderson Brumburger (DAB) model provides a scale factor, A, that is proportional to the contrast between the two coexisting phases and the volume fractions of the two phases, as shown in Equation 2.3 and 2.4.[69]

1) At low q,

$$A = 8\pi\,(\Delta SLD)^2\varphi_1(1-\varphi_1) \quad (2.3)$$

where $\Delta SLD = SLD_{PCBM\ aggregate\ phase} - SLD_{Mixed\ phase} = 4.4\times10^{-6} - [(\varphi_{1,m})4.4\times10^{-6} + (1-\varphi_{1,m})\,SLD_{polymer}]$

2) Similarly, at high q,

$$A = 8\pi(\Delta SLD)^2\varphi_2(1-\varphi_2) \quad (2.4)$$

where $\Delta SLD = SLD_{PCBM\ aggregate\ phase} - SLD_{Mixed\ phase} = 4.4\times10^{-6} - [(\varphi_{2,m})4.4\times10^{-6} + (1-\varphi_{2,m})\,SLD_{polymer}]$

Using Equations 2.1, 2.2, 2.3 and 2.4, the parameters that evolve from the fits of the scattering data to the DAB model can be manipulated to determine the values of φ_1, φ_2, $\varphi_{1,m}$ and $\varphi_{2,m}$ for the active layers that consist of the 7 LBG alternating copolymers of interest and PCBM.

The correlation length of each bulk heterojunction is directly obtained from the fit of the scattering data to the Debye Anderson Brumburger (DAB) two phase model. The two phase system is characterized by a single length scale, the correlation length, which is a measure of the average spacing between the phases. For the current system, it correlates to the size of the PCBM aggregate phase. The DAB model assumes smooth interfaces between two phases. The specific interfacial area, S/V between the two phases can also be determined from the fit, as it is a function of correlation length and the volume fraction of the two phases as $S/V = 4\varphi(1-\varphi)/\xi$. The volume fraction of the PCBM aggregate phase and the correlation lengths at both low (nano) and large (meso) length scales will be indicative of the ability of the bulk heterojunction to efficiently allow charge transport. Similarly, the amount of interfacial area between two phases that exist at both length scales will provide insight into the propensity for this morphology to allow exciton dissociation into free charge carriers.

2.6 Results and Discussion

The relationship between the structural information that is derived from the analysis of the scattering data and photovoltaic performance is complex. For instance, the volume fraction of the PCBM clusters will impact the electron transport of the bulk heterojunction, where a larger volume fraction will portend better transport. However, it is important to emphasize that the scattering data do not provide information on connectivity of the phase. Therefore, while it is expected that a higher volume fraction of PCBM clusters at larger length scales will result in better electron transport, this correlation is not without complexity.[30] Similarly, at smaller length scales, a smaller volume fraction of the PCBM clusters is desirable for improved electron transport, as these clusters are not well connected. Finally, the correlation length provides a measure of the average domain size of the polymer rich phase and PCBM aggregate phase; this parameter provides a measure of the electron and hole transport pathway length size.

The interfacial area between the polymer and fullerene is a crucial parameter in the performance of an organic solar cell active layer as this provides a direct measure of how much area is available to dissociate excitons and create individual charge carriers. Therefore, a higher surface area to volume (S/V) ratio is desired at large length scale to enable the dissociation of excitons. At low length scales, an ideal structural model consists of individual PCBM distributed

in the miscible phase, to minimize PCBM aggregates at smaller length scale that do not connect to the larger PCBM aggregates at the large length scale. In this case, these aggregates at small length scale can serve as charge traps where generated charges will not be able to contribute to the resultant current and end up being trapped or recombine. Similarly, hole mobility depends on polymer ordering and backbone planarity. Hence, higher polymer crystallinity is desirable. Nevertheless, very high polymer crystallinity is undesirable as it will limit the miscibility of PCBM in the polymer as the PCBM is only miscible in the polymer amorphous phase.

The results based on the fits of the scattering data to the DAB model and the formalism described earlier are presented in Tables 2.2 to 2.7. Table 2.2 presents the volume fraction of the PCBM aggregates at large length scale for all the films consisting of PCBM and the LBG polymer. Clearly, the volume fraction of the PCBM aggregates is very low in the polymers containing TPD or TID (electron poor) unit, indicating a substantial mixing of PCBM in these polymers. Table 2.3 shows the correlation length of the two phases at large length scale, where the correlation length is similar for all the polymers except for P-CTD-BDT(EH). It is interesting that there is no specific trend in the correlation length with the presence or absence of electron poor units (CTD, TPD, TID) or structure of the electron rich units (BDT, BBDT) or structure of the side chains (EH, C12).

Table 2.2. Volume fraction of the PCBM aggregates at the large length scale, φ_1 for the 7 low band gap (LBG) alternating copolymers.

LBG copolymer	**φ_1 (volume %)**
P-CTD-BDT(EH)	19
P-CTD-BBDT(C12)	13.7
P-BDT(EH)	7
P-CTD-BBDT(EH)	6
P-CTD-BDT(C12)	4.2
P-TPD-BDT(EH)	2.4
P-TID-BDT(EH)	1.6

The surface area to volume ratio at large length scale is calculated from the data that emerges from fitting the scattering data to DAB model using Equation 2.5.[64]

$$\frac{S}{V} = \frac{4\varphi_1(1-\varphi_1)}{\xi} \tag{2.5}$$

As stated above, an increase in S/V will improve exciton dissociation, where Table 4 lists this data for all the polymeric systems based on the data that is tabulated in Table 2.2 and 2.3. Inspection of Table 2.4 show that in the P-CTD-BBDT(C12)/PCBM based BHJ, exciton dissociation is 1.5-2 times more probable than the active layers based on P-CTD-BBDT(EH), P-CTD-BDT(EH), P-CTD-BDT(C12) or P-BDT(EH). Based on the S/V values, exciton dissociation is least probable in the BHJ active layers based on P-TPD-BDT(EH) and P-TID-BDT(EH) where their S/V ratios are 4-8 times lower than that of P-CTD-BBDT(C12).

Based on the S/V ratio, it appears that the presence of the electron rich BBDT units in the LBG alternating copolymer improves the amount of interfacial area between the PCBM aggregates and the polymer rich phase. When comparing the role of side chain, the results indicate that the linear C12 side chain offers a morphology with more interfacial area than the branched EH (ethyl hexyl) as side chains. The presence of the electron poor CTD units in the LBG alternating copolymer lead to an increase in the interfacial area relative to other electron poor units (TPD and TID).

Meanwhile, the interfacial area of the BHJ that contains P-TPD-BDT(EH) is 50% higher than the P-TID-BDT(EH) BHJ. Thus, one would expect that the charge generation is more efficient in the BHJ that includes P-TPD-BDT(EH) than the one with P-TID-BDT(EH), which should translate to improved photovoltaic performance. Previous results do in fact indicate that polymer solar cells consisting of P-TPD-BDT(EH) has higher photocurrent than those that are based on P-TID-BDT(EH).[56, 70]

The correlation lengths that are reported in Table 2.3 show that this parameter is greater than 500 Å for all the BHJ systems studied here. As the typical photovoltaic films are a few hundred nm thick, these correlation lengths should be sufficient to allow efficient charge transport across the film. In particular, the P-CTD-BDT(EH) based system exhibits the largest domain sizes, with a correlation length that is more than twice that of the other polymers studied (Table 2.4). Hence, S/V ratio of P-CTD-BDT(EH) is low even if the volume fraction of large aggregates is high compared to others (Table 2.2). Similarly, the volume fraction of the PCBM

Table 2.3. Correlation lengths of the bulk heterojunctions at large length scale, ξ for the 7 LBG alternating copolymers.

LBG copolymer	**ξ (Å)**
P-CTD-BDT(EH)	1885
P-BDT(EH)	862
P-CTD-BBDT(C12)	735
P-TID-BDT(EH)	700
P-TPD-BDT(EH)	614
P-CTD-BBDT(EH)	553
P-CTD-BDT(C12)	490

Table 2.4. The surface area to volume ratio at large length scale for the bulk heterojunctions of the 7 LBG alternating copolymers.

LBG copolymer	**S/V ($Å^{-1}$)**
P-CTD-BBDT(C12)	0.00064
P-CTD-BBDT(EH)	0.0004
P-CTD-BDT(C12)	0.00033
P-CTD-BDT(EH)	0.00033
P-BDT(EH)	0.0003
P-TPD-BDT(EH)	0.00015
P-TID-BDT(EH)	8.9E-05

aggregates in the P-CTD-BBDT(C12) based BHJ system is large but also has a modest correlation length (~700 Å), which translates to a larger S/V ratio of P-CTD-BBDT(C12). The volume fraction of PCBM in the mixed phase of the BHJ at large and small length scales are shown in Tables 2.5 and 2.6 respectively.

The copolymers, (P-TPD-BDT(EH) and P-TID-BDT(EH)), exhibit higher PCBM mixing relative to that of the other polymers at both length scales, as presented in Tables 2.5 and 2.6. The volume fraction of PCBM in these polymers is above 45% at large length scale, which is near maximum mixing possible for these systems. This unique property can be attributed to the presence of large alkyl side chains on the electron poor unit (TPD or TID), which may provide poor polymer-polymer packing and enable polymer-fullerene mixing. It is also interesting that these polymers contain a nitrogen in their structure, as the lone pairs of the nitrogen are known to form strong non-covalent interactions with carbon nanotubes and fullerenes. Thus, it appears that the inclusion of the nitrogen atom provides a thermodynamic interaction between the polymer and fullerene that translates to improved mixing behavior. Based on the volume fraction of PCBM in the amorphous polymer at the local length scale, the distance between PCBM molecules, H, that reside individually in the miscible phase can be estimated from Equation 2.6:

$$\frac{H}{D} = \left(\frac{\varphi_m}{\varphi}\right)^{1/3} - 1 \qquad (2.6)$$

where D is particle diameter (10 Å for C_{60}, 15 Å for $PC_{60}BM$) and φ_m is the maximum random packing fraction of a sphere (~0.64).[63] φ is the volume fraction of PCBM in the miscible phase at the local length scale, which is denoted as $\varphi_{2,m}$ earlier. A smaller value of H improves the possibility of charge transport between fullerenes in the mixed phase, which is required to allow transport to the PCBM aggregates that connect to the electrodes. Values of H for all the LBG alternating copolymers is tabulated in table 2.7. As all of these values are between 2 and 4 Å, it is expected that this charge transport between fullerenes in the miscible phase will be similar for all systems. It has been seen earlier that H value greater than ~11 Å is detrimental to electron transport in the amorphous phase.[63]

The low band gap polymers examined here do exhibit small amount of crystallinity, which can be characterized by the area under the crystal peak that occurs at high q. Please refer the appendix to see 100 peak for LBG alternating copolymers. There is no 100 peak for P-BDT(EH) based on Figure 2.5 and Figure 2.6. The area under this peak is proportional to the

Table 2.5. The volume fraction of PCBM in the mixed phase at the large length scales for the 7 LBG alternating copolymers.

LBG copolymer	**$\varphi_{1,m}$ (volume%)**
P-TID-BDT(EH)	47.5
P-TPD-BDT(EH)	45.9
P-CTD-BDT(C12)	43.1
P-CTD-BBDT(EH)	42.9
P-BDT(EH)	41.6
P-CTD-BBDT(C12)	36.6
P-CTD-BDT(EH)	35.1

Table 2.6. The volume fraction of PCBM in the mixed phase at the small length scale for the 7 LBG alternating copolymers.

LBG copolymer	**$\varphi_{2,m}$ (volume %)**
P-TID-BDT(EH)	46.5
P-TPD-BDT(EH)	43
P-BDT(EH)	38.7
P-CTD-BBDT(EH)	38.3
P-CTD-BDT(C12)	37.7
P-CTD-BDT(EH)	33.5
P-CTD-BBDT(C12)	33.4

Table 2.7. The average distance between PCBM molecules in the mixed phase at small length scale for the 7 LBG polymers.

LBG copolymer	H (in Å)
P-CTD-BDT(EH)	3.6
P-CTD-BBDT(C12)	3.6
P-BDT(EH)	2.8
P-CTD-BBDT(EH)	2.5
P-CTD-BDT(C12)	2.5
P-TPD-BDT(EH)	2.1
P-TID-BDT(EH)	1.9

Table 2.8. Area under the crystalline peak for the 7 LBG polymers.

LBG copolymer	Area under peak
P-CTD-BDT(C12)	0.015
P-CTD-BDT(EH)	0.011
P-CTD-BBDT(EH)	0.0071
P-TPD-BDT(EH)	0.0063
P-CTD-BBDT(C12)	0.0049
P-TID-BDT(EH)	0.002
P-BDT(EH)	0

amount of polymer crystallinity, and this value is reported in Table 2.8. These values provide insight into the deviation of the calculated PCBM volume fraction value from the actual PCBM volume fraction in the mixed phase. Clearly, P-CTD-BDT(12) exhibits the maximum amount of crystallinity, which appears to be the results of the linear side chains to interdigitate as illustrated in Figure 2.7. These values indicate that the amount of polymer crystallinity in these samples is quite low, and thus the PCBM volume fraction in the mixed region, reported are accurate. As P-CTD-BDT(C12) shows the maximum amount of ordering, this polymer will exhibit the largest deviation of calculated volume fraction of PCBM in the miscible region.

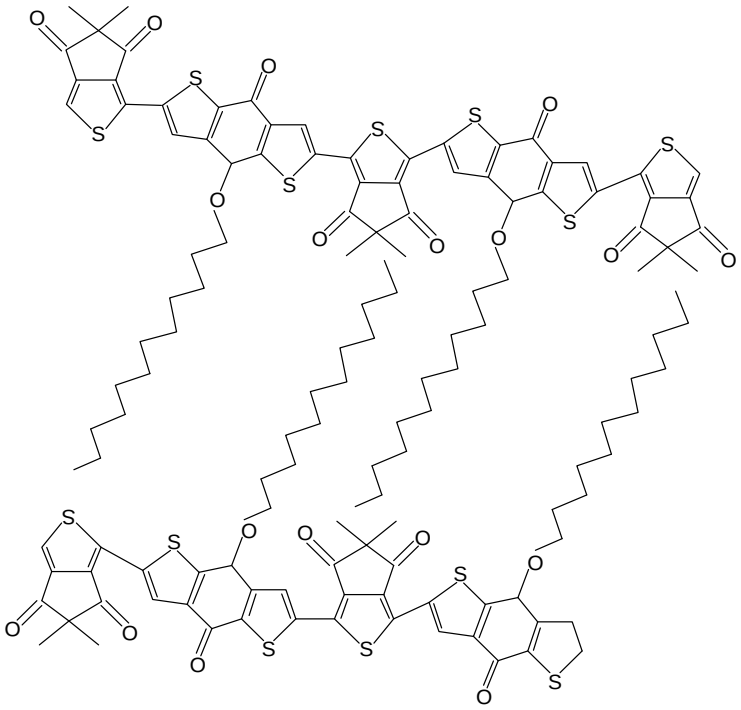


Figure 2.7. Illustration of packing of P-CTD-BDT(C12).

2.7 Conclusion

Manipulating the miscibility of PCBM in a low band gap conjugated polymer and its crystallinity can have a profound impact on the photovoltaic performance of the resultant BHJ as characterized by the current voltage characteristics (J_{SC} and FF) of conjugated polymer:PCBM bulk heterojunction OPV active layer. Based on the morphological studies presented here, the BHJ active layers that are based on P-CTD-BBDT(C12) or P-CTD-BBDT(EH) should exhibit

improved high current and hence, efficiency as a result of the increased polymer/fullerene interfacial area. Furthermore, it can be proposed that BHJ containing LBG alternating copolymers with BBDT as electron rich unit will exhibit higher current than BDT. Similarly, it can be suggested that BHJ containing LBG alternating copolymers with C12 as side chain will have higher short circuit current relative to EH. The morphological results also suggest that the BHJ active layers based on P-TPD-BDT(EH) and P-TID-BDT(EH) will exhibit poorer current due to a decrease in polymer/fullerene interfacial area. So, it can be said that LBG alternating copolymers containing nitrogen in the electron poor units (TPD and TID) will have low photo-current. Volume fraction of PCBM in the mixed region of LBG alternating copolymers and PCBM is much higher (> 35 volume %) than other LBG polymers[21] e.g. P3HT (~ 22 volume %).[71] The distance between PCBM molecules in the miscible phase at the local length scale is less than 4 Å in all the films, which suggests that that charges generated in this phase will be able to transport to the continuous PCBM aggregates and allow charge extraction.

Hence, the structural results presented in this study can be correlated to the photovoltaic performance of these active layers. The results clearly show that the volume fraction of the PCBM aggregate at both length scales, the correlation length at both length scales, the volume fraction of PCBM in mixed regions of both length scales and hence overall photovoltaic performance of the bulk heterojunction films can be controlled by changing specific structure of the push-pull low band gap polymer. Further control of the morphology may be possible by further processing, including post deposition solvent annealing or deposition from solvents with solvent additives. Hence, an interesting future study would be to examine the effect of processing conditions on morphology and efficiency of films based on these novel polymers.

Chapter 3

Impact of Solvent Quality on The Morphology and Performance of Solvent-Annealed Low-Band Gap Bulk Heterojunction OPV Active Layers

3.1 Background

In addition to chemical structure of LBG alternating copolymer, the morphology of bulk heterojunction can also be modified by post processing. Various processing modifications have been applied to improve morphology and properties of polymer based solar cells including thermal annealing, [27, 72, 73] solvent annealing, [25, 26, 74] and solvent additives prior to deposition. [30, 36, 75, 76] Although the addition of solvent additive to solvent prior to spin coating results in improved solar cell performance, the morphology of this film immediately after deposition is locked in and is directed by the film formation process. The fast solvent evaporation that occurs during spin coating kinetically traps the morphology and blocks the evolution of the morphology to more thermodynamically stable structures. Therefore, guiding the morphology of film using post processing techniques such as thermal or solvent annealing provides an additional mechanism to direct the morphology to a more optimal structure. Thermal annealing is a common, energy intensive technique. Unfortunately, in most bulk heterojunction systems consisting of amorphous LBG alternating copolymer and a fullerene, thermal annealing usually induces a decrease in power conversion efficiency.[76-79] Therefore, solvent annealing, wherein the BHJ film is exposed to an atmosphere of solvent vapors that can diffuse into the film to allow it to evolve to a more thermodynamically favorable structure, can be applied to improve device morphology and hence, efficiency. Moreover, LBG alternating copolymers usually have high glass transition temperatures (T_g) or no observable T_g[67] and therefore, thermal annealing cannot induce mobility to the system without degradation. In addition, in thermal annealing, the structure develops in seconds and hence phase separation and crystallization happens simultaneously, making it difficult to precisely control the bulk morphology.[80] Solvent annealing has been found to be a more tunable process to control the morphology of a bulk

heterojunction due to the different solubilities of each component in the vapor annealing solvent. Hence, annealing low band gap polymer and PCBM bulk heterojunctions in the vapor of selective solvents can enable precise control of the morphology.[26] Previous work in our group [26] examined the change in the morphology an OPV performance of a low band gap conjugate polymer (PCPDTBT):fullerene BHJ with solvent annealing in solvents with varying solvent quality for the polymer and fullerene. The three solvents are 2-chlorophenol (CP), bromobenzene (BB) and o-dichlorobenzene (ODCB), where CP is selective to PCBM, BB is selective to PCPDTBT and ODCB is a mutual solvent for both components. Figure 3.1 shows the chemical structure of PCPDTBT, CP, BB and ODCB. Table 3.1 shows solubility of PCPDTBT and PCBM in CP, BB and ODCB. These results showed that annealing the BHJ in the CP vapor provided the greatest performance improvement, while the BHJ that was annealed in BB showed no change in OPV performance. These performance characteristics were also correlated to the morphology of the OPV active layer as determined by neutron scattering. The films in this previous study were annealed for 4 hours. In order to understand the evolution of the structure and performance with solvent annealing time, the current study correlates the solvent vapor diffusion into the film to the changes in film morphology and evolution of photovoltaic performance with solvent annealing time.

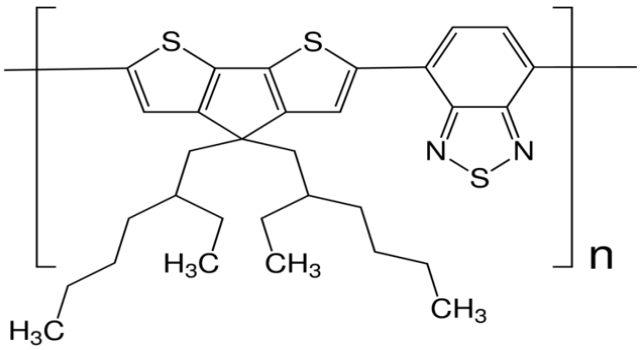


Figure 3.1.(a). Image showing the chemical structure of PCPDTBT.

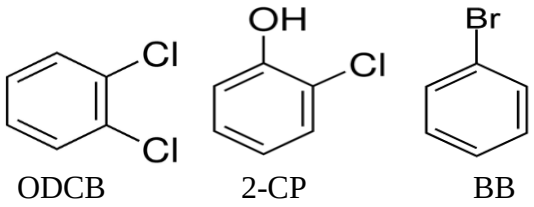


Figure 3.1.(b). Image showing chemical structure of solvents used for solvent annealing.

Table 3.1. Solubility of PCPDTBT and PCBM in the solvents studied.

Solvents	**Solubility (mg/ml)**	
	PCPDTBT	PCBM
1 - Bromobenzene (BB)	89	33
1,2 - Dichlorobenzene (ODCB)	21	36
2 - Chlorophenol (CP)	0.2	128

[26]

3.2 Measurement of Solvent Vapor Diffusion into the OPV Active layer

Diffusion is the process by which matter is transported from one part of a system to another as a result of random molecular motion, which is driven by a concentration gradient. The diffusion coefficient or diffusivity, is a proportionality constant between the molar flux due to molecular diffusion and the gradient in the concentration of the diffusing species. Fick's first and second law of diffusion describes the diffusion process.

$$\text{Fick's first law : } \mathrm{F} = -\mathrm{D} \times \frac{\partial \mathrm{C}}{\partial \mathrm{x}} \tag{3.1}$$

In Fick's first law, F is the rate of transfer per unit area of cross-section, C is the concentration of diffusing substance, x the space coordinate measured normal to the cross-section, and D is the diffusion coefficient.

$$\text{Fick's second law : } \frac{\partial \mathrm{C}}{\partial \mathrm{t}} = \mathrm{D} \times \frac{\partial^2 \mathrm{C}}{\partial \mathrm{x}^2} \tag{3.2}$$

Fick's second law is applicable if diffusion is one-dimensional i.e. if there is a gradient of concentration only along the x-axis and D is independent of the concentration of the diffusing species. t in equation 3.2 is time.

The diffusion coefficient of the solvent vapor into the BHJ film during solvent annealing determines the solvent absorption rate. There are generally two methods to measure the diffusivity of a gas into a solid, i.e., the time lag method and the $t^{1/2}$ method. The first method is applicable in steady state, while the second one can be applied to the transient diffusion of the small molecule into a flat film by absorption.

Based on a model of a flat film placed in a solvent vapor environment, where only one surface of the film can absorb vapor, an equation relating total weight % increase of the film as a function of time is given by [81].

$$\frac{M_t}{M_{\square}} = 1 - \sum_{n=0}^{n=\square} \frac{8}{(2n+1)^2\pi^2} e^{\left[-\frac{D(2n+1)^2\pi^2 t}{l^2}\right]} \quad (3.3)$$

where Mt is the weight increase at time t, M_N is total weight increase, and l is the film thickness. For $M_t/M_N < 0.6$, i.e. at the initial stage of the sorption process, the above equation can be further simplified to

$$\frac{M_t}{M_\infty} = \left(\frac{16D}{\pi l^2}\right)^{1/2} t^{1/2} \quad (3.4)$$

During the solvent uptake process, the film thickness increases due to swelling. Therefore, a calibration equation can be applied to account for this swelling as described in Equation 3.5.

$$D_A^B = D^v(1 - R_v)^2 \quad (3.5)$$

In Equation 3.5, D_A^B is the diffusivity under fixed film thickness, D^v is the diffusivity with swelling, and R_v is the volume fraction of the vapor in the film.

3.3 Experiments

Materials - PCBM was purchased from Nano-C, and PCPDTBT (Poly [2,6-(4,4-bis-(2-ethylhexyl)-4H-cyclopenta[2,1-b;3,4-b'] dithiophene)-alt-4,7 (2,1,3-benzothiadiazole)]) (MW = 41K, PDI = 2.3) was purchased from 1-Materials. Both are used without further purification. To fabricate the PCPDTBT/PCBM films, PCPDTBT (7mg/ml) and PCBM (14 mg/ml) were dissolved in o-dichlorobenzene (ODCB). Prior to spin coating, the silicon wafers were cleaned by immersion in a 3:1 (v/v) mixture of concentrated sulfuric acid and 30%(v/v) hydrogen peroxide, heated to ~70°C for >2 hours, and rinsed with copious amounts of high purity water and dried under a stream of nitrogen. The photovoltaic active layer PCPDTBT:PCBM mixture was fabricated by spin casting a thin film from the PCPDTBT/PCBM solution at 800 rpm for 5s, followed by 300 rpm for 5 min. Solvent annealing of the film was carried out in an upright column containing a reservoir of the solvent at the bottom. Three solvents bromobenzene (BB), 1,2-dichlorobenzene (ODCB), and 2-chlorophenol (CP) were used in this work.

UV-Vis spectroscopy - (UV-Vis) spectra were recorded with a Thermo Scientific Evolution 600 UV-Vis spectrophotometer in the wavelength range of 300-900 nm.

Energy Filtered - Transmission Electron Microscopy - Energy filtered - transmission electron microscopy (EF-TEM) was completed on a Zeiss Libra 200 MC by Halie Martin, a

graduate student with experience in EF-TEM in our lab. The experiment allows the discrimination of the polymer from the fullerene because the two components absorb electrons at different energies. Thus, the energy of the electrons that impinged on the sample were filtered to bands that were 8 eV in width. PCPDTBT absorbs at approximately 21-22 eV, a center energy of 19 eV with a range of kinetic energy between 15-23 eV was used to monitor the presence of PCPDTBT in the film. Similarly, the PCBM domains absorb around 26 eV, electrons with kinetic energies centered at 30 eV was used to image PCBM domains. These samples were prepared by spin coating PEDOT:PSS on a surface at 2000 rpm for 60s. Then, this film was heated at 120°C for 20 min. Then, a PCPDTBT:PCBM solution was spin coated at 4000 rpm for 30s on the top of PEDOT:PSS layer. To prepare the PCPDTBT:PCBM solution for spin coating, ~7 mg of PCPDTBT, ~14 mg of PCBM and ~1 ml of ODCB was used. The resultant PCPDTBT:PCBM layer was float coated on a carbon grid for EF-TEM evaluation.

Photovoltaic device fabrication and characterization - Indium tin oxide (ITO) glass substrates were first washed with detergent and then cleaned in an ultrasonic bath using DI water, acetone and isopropyl alcohol (IPA). The cleaned substrates were subsequently treated with UV ozone for 20 minutes. Filtered PEDOT:PSS (Baytron P4083) was spin cast on the UV-treated ITO glass at 4000 rpm for 40s. After baking the PEDOT:PSS films in air at 140 °C for 20 min, the active layer was spin cast at the same condition as above. Solvent annealing of the active layers were carried out at the same conditions as described earlier for 0.5 hr, 1 hr, 2 hr, 5 hr and 10 hr for solvent ODCB and 2-CP. After solvent annealing, the film was vacuum heated at 60°C for 10 min to ensure that there is no solvent left in the film. Finally, to create the OPV device, 40 nm of Ca and 60 nm of Al were thermally deposited on the film through a shadow mask. Current-voltage (I-V) characterization of the polymer photovoltaic cells was conducted using a Thermal Oriel 96000 300-W solar simulator under the illumination of AM 1.5G, 100 mW/cm^2. The device fabrication and characterization experiments were conducted by members of Prof. Bin Hu's laboratory.

Solvent annealing - In the solvent annealing process, solvent is added to the bottom of a 100 cm long vertical column and allowed to equilibrate for 6 hours, as shown in Figure 3.2. This forms a linear vapor pressure gradient along the length of the column. In this column, the solvent vapor pressure is zero at the top of the column and 100 cm down from the top represents 100% solvent vapor pressure. The amount of solvent vapor that the PCPDTBT/PCBM film is exposed

to is thus determined by the amount of time that the sample is in the column as well as the height at which sample resides. The samples in this study were left at a height that is 90% down the column i.e. they were exposed to 90% solvent vapor pressure.

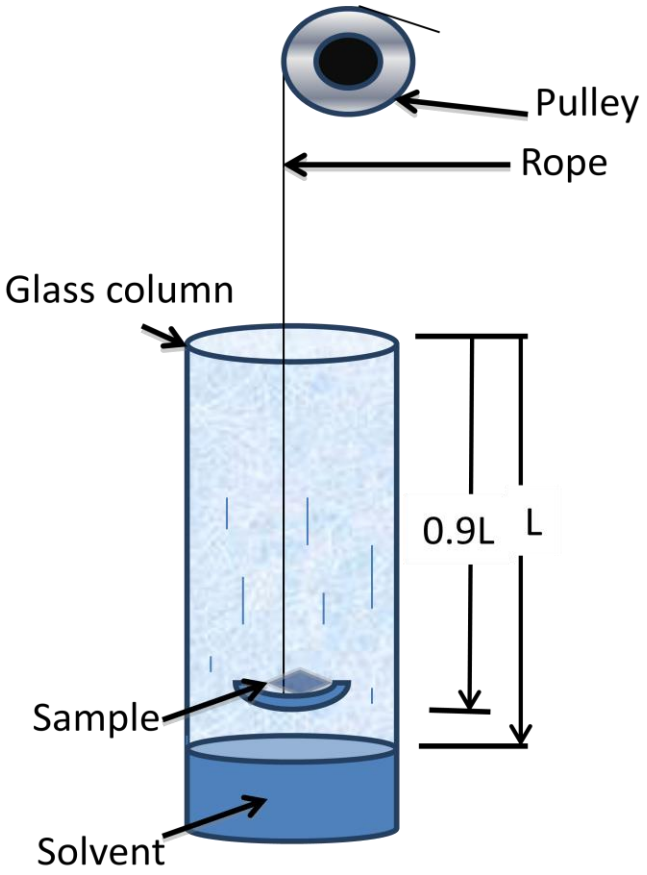


Figure 3.2. Schematic of solvent annealing apparatus.

Diffusivity measurement – To monitor the diffusion of the solvent vapor into the BHJ film, glass wafers of ~ 1cm^2 were cut. Solutions of PCPDTBT:PCBM in chloroform were prepared by mixing 22 mg of PCPDTBT and 44 mg of PCBM in ~2 ml of chloroform. The solution was the heated overnight at ~50°C to ensure that the PCPDTBT and PCBM are completely dissolved. Subsequently, the solution was drop cast on glass wafer to make thick films. The films were vacuum dried overnight before solvent annealing for various time intervals. Same sample was used for solvent annealing purpose for various time intervals. Hence, after weighing the solvent annealed sample, it was vacuum dried by heating for ~15 - 40 min at 60 °C based on the time of exposure of film to solvent. Usually, heating was done until dried film weight was almost same

as the pre-annealed film. The dried sample was also weighed in order to verify if there is weight loss during vacuum drying. This weight was used for calculating weight gain after solvent annealing for next time interval. This procedure was followed for obtaining weight gain at different time intervals until the weight gain in % became almost constant.

3.4 Results and Discussion

Table 3.2 summarizes the time evolution of the percent weight increase of the bulk films during solvent vapor annealing in three unique solvents. According to Equation 3.4, the diffusivity of the solvent vapor in the BHJ film can be determined from the slope of the first few points on each curve satisfying the condition $M_t/M_\infty < 0.6$. After applying equation 3.5, the corrected diffusivity is also calculated. Based on the data presented in Table 3.2, the PCPDTBT:PCBM film will absorb ~14%, ~5% and 8% of their weight when exposed to the solvent vapor of BB, CP and ODCB respectively. This is understandable based on the solubility of PCPDTBT in these solvents as shown in Table 3.1, where BB is the best solvent, ODCB is still a good solvent and CB is a poor solvent. The thickness of the bulk films prior to exposure to

Table 3.2. Weight% increase of the PCPDTBT:PCBM film with exposure time to solvent vapors for three solvents.

1-Bromobenzene		**2-Chlorophenol**		**o-Dichlorobenzene**	
Time (hr)	**Wt% increase**	**Time (hr)**	**Wt% increase**	**Time (hr)**	**Wt% increase**
0	0	0	0	0	0
0.0833	2.05	0.25	0.6	0.0833	0.97
0.25	4.33	0.5	1.16	0.25	1.74
0.5	5.54	1	1.63	0.5	2.96
1	7.88	2	2.09	1	4.08
2	11.57	5	3.13	2	5.36
5	12.73	7	3.7	5	7.05
8	13.62	10	4.18	7	7.8
23.9	13.73	11.75	4.26	9	8.27
44.5	13.77	21.6	4.71	12.85	8.38
60.3	13.88	40.2	5.25	62.2	8.47
		43.2	5.33		
		70.67	5.39		

the ODCB, CP and BB solvent vapors were 0.37 mm, 0.27 mm and 0.26 mm respectively. The increase in thickness with solvent vapor exposure was approximately 10% for all samples. Figure 3.3 shows the weight increase of the film on exposure to the vapor of BB, ODCB and CP. Based on the slope of the initial absorption rate as shown in Figure 3.4, D^v for the vapor of BB, ODCB and CP are $4.34*10^{-9}$ m^2/hr $5.97*10^{-9}$ m^2/hr and $1.04*10^{-9}$ m^2/hr. Assuming fixed film thickness, D_A^B for BB, ODCB and CP are $3.52*10^{-9}$ m^2/hr, $4.84*10^{-9}$ m^2/hr and $0.84*10^{-9}$ m^2/hr respectively. It appears that the poor solubility of PCPDTBT in CP dramatically limits the diffusion of the solvent vapor into the BHJ film. On the other hand, the modest solubility of PCPDTBT and/or PCBM in ODCB and BB provides a mechanism for the relatively unhindered diffusion of solvent vapor into the BHJ film for these two solvent vapors. Although the similar solubility of PCPDTBT and PCBM in ODCB appears to provide a slight increase in the diffusion rate of this solvent into the BHJ film relative to that of the BB vapor.

According to Equation 3.4, the time needed for the solvent vapor to diffuse across a film is proportional to the square of film thickness. The thickness of the bulk film that is used to monitor the vapor diffusion is several thousand times thicker than the thin film that is used in polymer based solar cells. Thus, assuming a film thickness of 200 nm for an active layer in an polymeric solar cell, the time needed for BB, CP or ODCB to diffuse across this film and saturate it will be much less than a second (a few hundredths of a second for CP and a few thousandths of a second for ODCB and BB). Hence, the time required for diffusion across this thin film is low. Thus any time dependence of the morphology development that occurs during solvent vapor annealing is not the result of the rate at which the solvent saturates the thin film, but rather is the evolution of the morphology in the presence of the solvent. These results also provide a quantifiable measure of how much solvent resides in these saturated active layers during solvent vapor annealing.

Previous results in our group show that the morphology and performance of an OPV active layer will evolve with solvent vapor annealing time, and thus we sought to monitor the time evolution of the OPV performance with solvent vapor annealing time. As our previous results show that annealing in BB solvent vapor reduces the efficiency of the polymer based photovoltaic films with annealing [26], we focused on the systems that are annealed in CP and ODCB solvent vapor only.

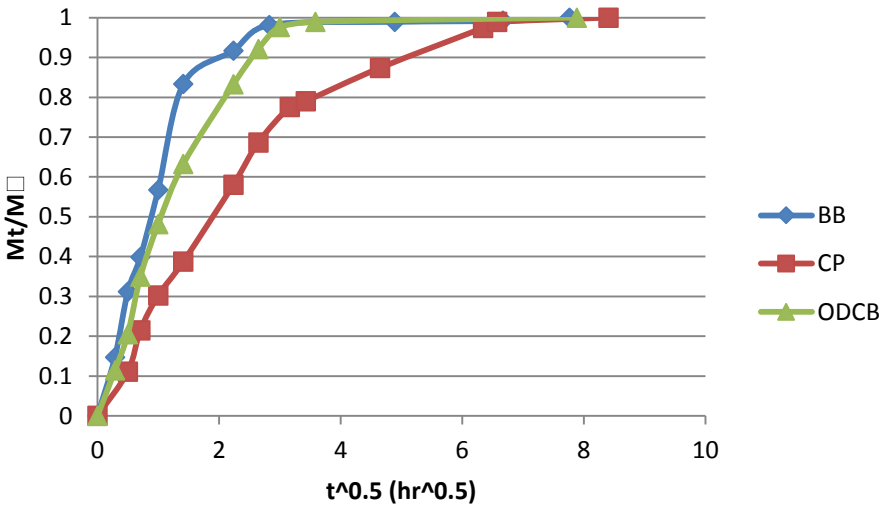


Figure 3.3. Increase in the mass of a PCPDTBT:PCBM thick film with vapor annealing time on exposure to BB, ODCB, or CP solvent vapor.

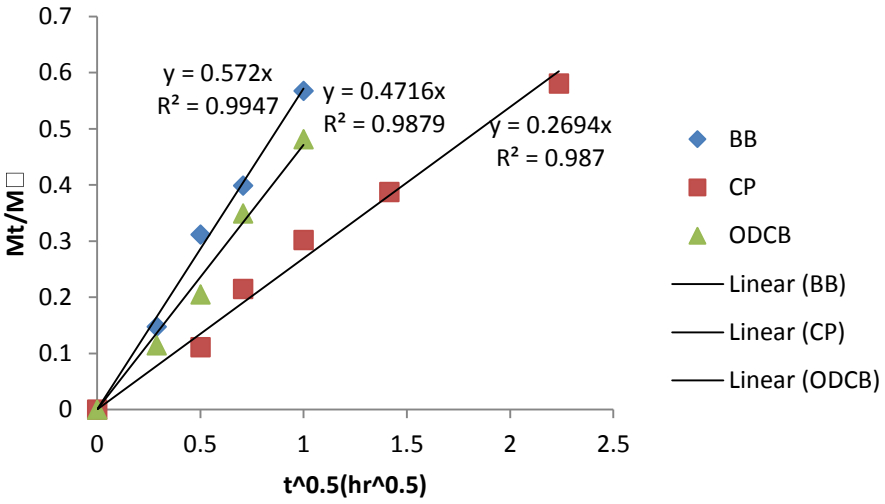


Figure 3.4. Increase in the mass of PCPDTBT:PCBM thick films with vapor annealing time with exposure to BB, ODCB, or CP solvent vapor.

Figure 3.5 shows the change in the UV-Vis measurements of PCPDTBT:PCBM films that are annealed in CP solvent vapor, exhibiting a modest peak shift that indicates a slight change in polymer orientational ordering. However, the peak intensity drops with annealing time. It is difficult to explain the downward shift. It may be due to increase in disorder. The UV-Vis spectra of the sample that is annealed in ODCB vapor is shown in Figure 3.6, and shows a slight red shift as annealing time progresses. The red shift may be ascribed to either an interchain delocalization or a planarization of the polymer backbone. This results in an increased □□□ conjugation length and higher degree of ordering of the polymer chain.

The changes in the morphology of the samples as determined by EF-TEM are shown in Figure 3.7. These results show that the sample that is annealed in ODCB is very well dispersed does not after 1 hour of solvent vapor annealing, and shows a modest amount of PCBM aggregation (yellow in the images) after 10 hours of solvent vapor annealing. The BHJ that is annealed in CP vapor, however, shows much more structure with clear PCBM (blue) and PCPDTBT (yellow) domains that evolve after 4 hours of solvent vapor annealing, and continue to coarsen with further annealing time. This structural evolution may be attributable to the increased mobility of PCBM because of the high solubility of PCBM in CP, relative to that in ODCB.

In order to correlate the effect of solvent annealing on efficiency of solar cells, the current voltage characteristics of the BHJ as a function of solvent vapor annealing times were measured. These results are presented in Tables 3.3 and Table 3.4, which indicate that there is a significant increase in power conversion efficiency with solvent vapor annealing time for both solvents, but that the increase is more dramatic in the sample that is annealed in CP vapor. Closer inspection of the data shows that the V_{OC} in all cases are nearly same ~0.6V, but that the increase in performance is due to the slightly higher J_{SC} and FF of the sample that is annealed in the CP vapor relative to the one that is annealed in the ODCB vapor. As the presence of CP leads to formation of larger PCBM domain and the presence of ODCB leads to polymer ordering, it may be concluded that PCBM aggregation is more important than polymer ordering.

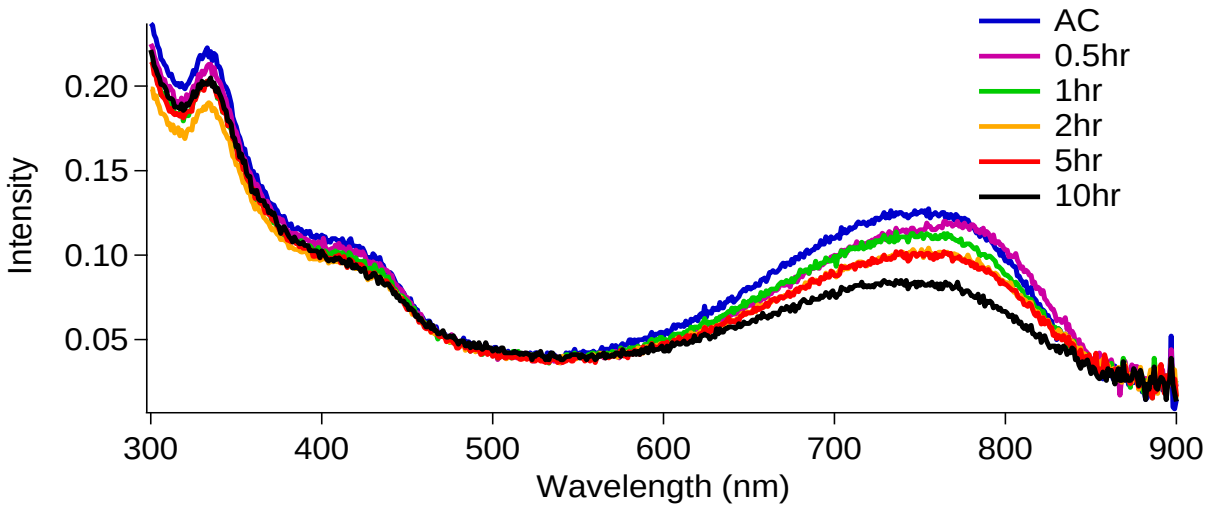


Figure 3.5. UV-Vis spectra for PCPDTBT:PCBM film solvent annealed in 2-CP vapor.

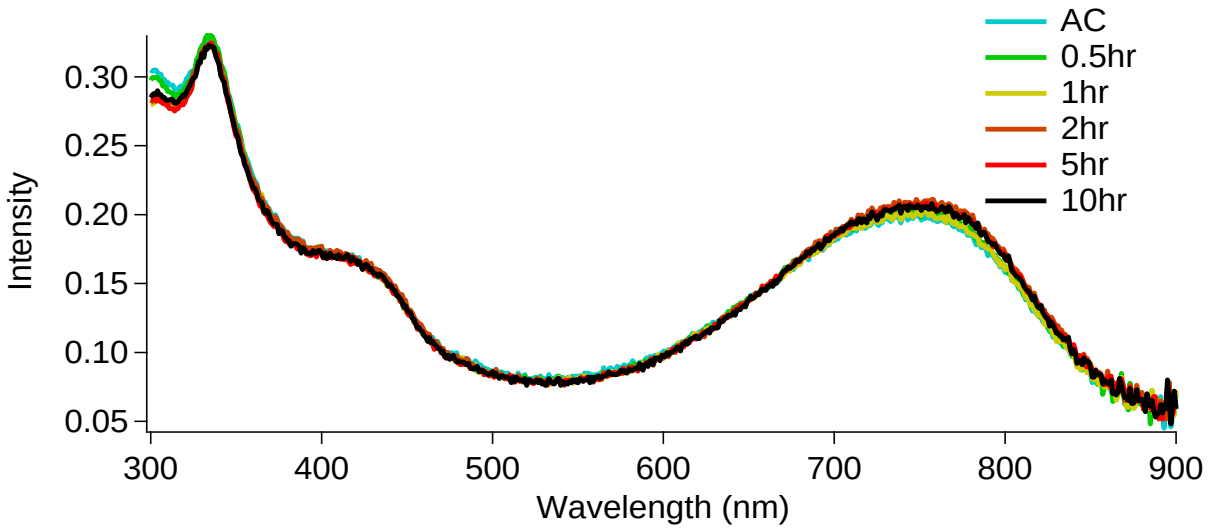
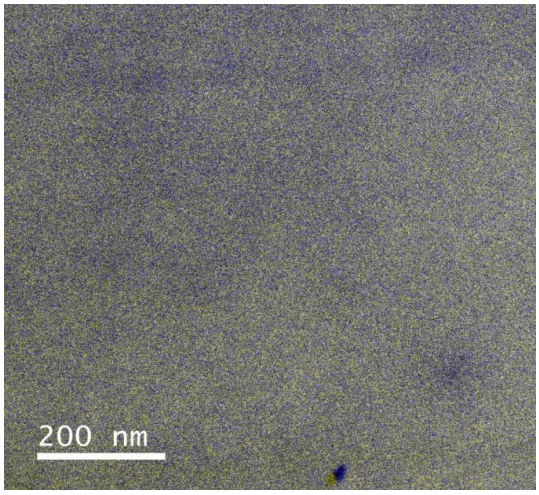
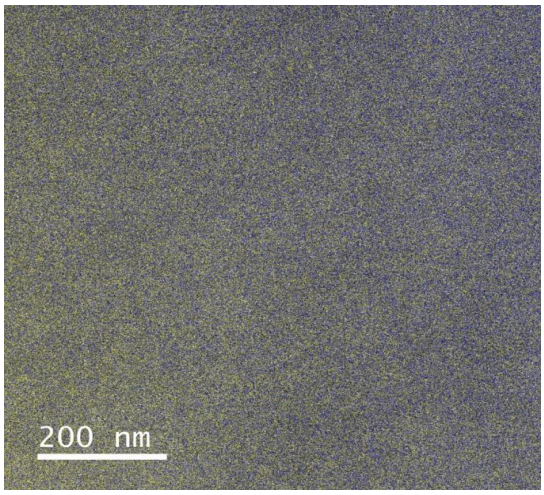


Figure 3.6. UV-Vis spectra for PCPDTBT:PCBM film solvent annealed in ODCB vapor.

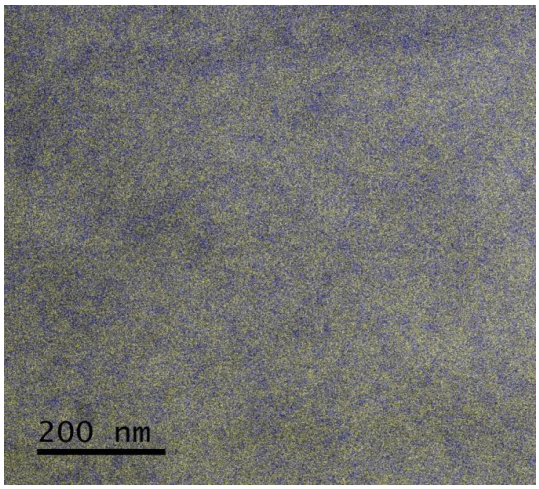
Figure 3.7. Time evolution of the EF-TEM images PCPDTBT:PCBM BHJ systems that are annealed in CP and ODCB solvent vapor. The PCPDTBT is blue in these images while the PCBM shows up as yellow.



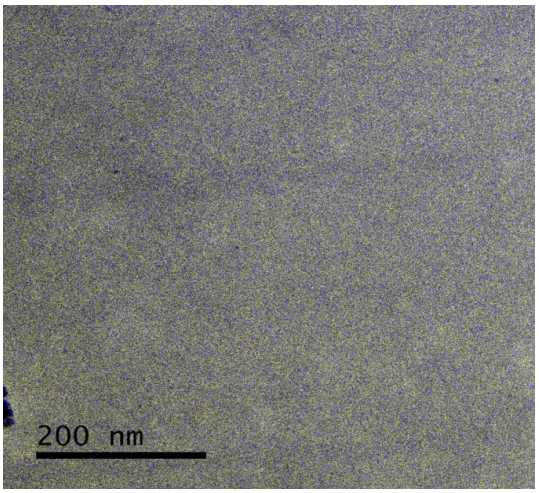
(a) EF-TEM microscopic image of the PCDPTBT:PCBM BHJ thin film that is annealed for 1 hr in ODCB vapor.



(b) EF-TEM microscopic image of the PCPDTBT:PCBM BHJ thin film that that is annealed for 2 hr in ODCB vapor.

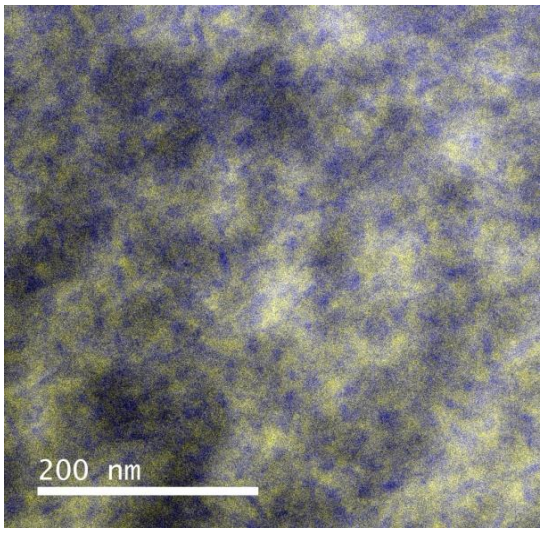


(c) EF-TEM microscope image of the PCPDTBT:PCBM BHJ thin film that is annealed for 10 hr in ODCB vapor.

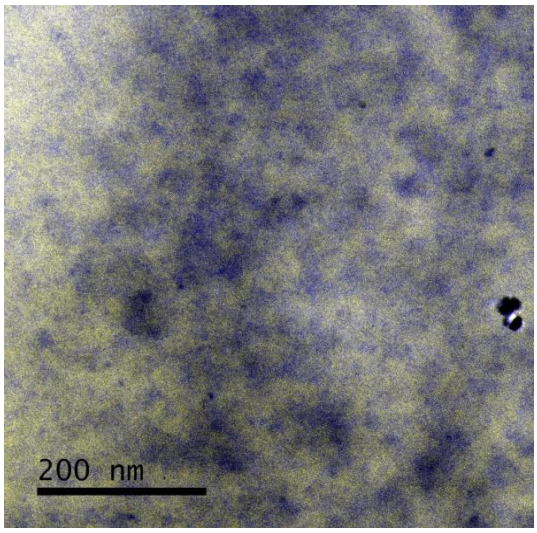


(d) EF-TEM microscopic image of the PCPDTBT:PCBM BHJ thin film that that is annealed for 1 hr in CP vapor.

Figure 3.7 continued.



(e) EF-TEM microscopic image of the PCPDTBT:PCBM BHJ thin film that is annealed for 4 hr in CP vapor.



(f) EF-TEM microscopic image of the PCPDTBT:PCBM BHJ thin film that is annealed for 10 hr in CP vapor.

Figure 3.7 continued

Table 3.3. Time evolution of the I-V characteristics for the BHJ that is annealed in ODCB vapor.

Annealing time (in hr)	J_{SC} (in mA)	V_{OC} (in V)	FF	PCE (in %)
0	6.87	0.6	0.48	1.98
0.5	6.32	0.59	0.51	1.91
1	7.14	0.59	0.51	2.16
2	6.36	0.59	0.51	1.92
5	8.51	0.59	0.51	2.71
10	9.15	0.59	0.51	2.92

Table 3.4. Time evolution of the I-V characteristics of the BHJ that is annealed in the CP vapor.

Annealing time (in hr)	J_{SC} (in mA)	V_{OC} (in V)	FF	PCE (in %)
0	6.87	0.6	0.48	1.98
0.5	8.57	0.61	0.62	3.25
1	10.3	0.61	0.57	3.59
2	8.67	0.61	0.62	3.28
5	10.8	0.61	0.58	3.84
10	11.5	0.61	0.58	4.05

3.5 Conclusion

The results in this chapter show that it takes less than a second for solvent vapor to diffuse across and saturate the OPV active layer thin film, but that the morphology and performance of the active layer evolve for hours during solvent vapor annealing. In the systems that are studying, the desired time for solvent annealing for optimized efficiency appears to be between 5-10 hours. This proves that change in film morphology progresses slowly over time. As CP annealed BHJ performs better than ODCB annealed system, it can be concluded that PCBM aggregation is more important than polymer ordering. Exposure of film to 2 successive solvents with preferential solubility to PCBM and PCPDTBT may be an interesting method to provide further control of the structure of the BHJ film and may further improve the power conversion efficiency. Structural analysis using small angle neutron scattering would also be interesting to provide additional structural information of the morphology evolution that occurs with solvent vapor annealing.

Chapter 4

Effect of Including Clay in PEDOT:PSS Thin Films on its Structural and Electronic Properties

4.1 Background

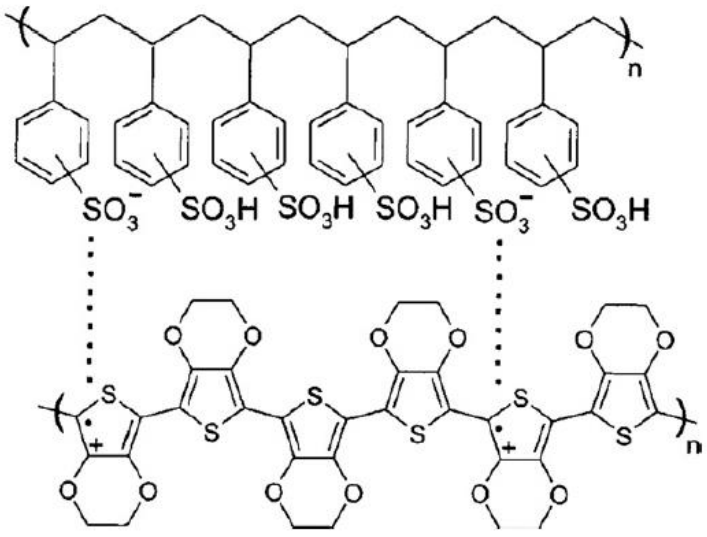
In the final project, the impact of clay loading in a conducting polymer thin film has been studied and linked to the morphology of conducting pathways. The conducting polymer under consideration in this project is PEDOT:PSS (Poly(ethylenedioxythiophene):polystyrene sulphonate). PEDOT:PSS is an electrically conducting polymer that is used primarily as hole transport layer in organic optoelectronic devices (solar cells, light emitting diodes etc.) on the top of the anode.[82] Other applications for PEDOT:PSS include antistatic coatings, electroluminescent devices (as a transparent conductor), capacitors (as conducting layer), sensors, transistors,[83] write-once read-many-times (WORM) memory,[84] neuroprostheses,[85] and as a substitute for Indium Tin Oxide (ITO) as an anode.[86] PEDOT:PSS has high electrical conductivity (~e.g. 1 Scm^{-1} for PEDOT:PSS = 1:2.5),[87] optical transparency (75% for visible light)[86] and thermal stability. Because PEDOT has low solubility in many solvents, it is combined with the water soluble polyelectrolyte, poly(styrene sulfonated) (PSS), thus making PEDOT:PSS processable.[88] The ionomer, PSS, also works as a charge balancing dopant. Figure 4.1 illustrates the doping of PEDOT by the PSS. It is believed that PEDOT:PSS films have two phases: a PEDOT rich phase distributed in the surrounding PSS phase, producing a granular morphology.[89] In their as-cast state, previous results show that these conducting films consists of PEDOT:PSS in coiled, linear or expanded coil conformations.[87] It is believed that the PEDOT/PSS (PEDOT rich phase) domains have a diameter that is $\geq$ ~20 Å,[90-93] compressed/flattened [94] and separated by a PSS layer whose thickness varies based on the ratio of PEDOT to PSS. It is also believed that the top layer of the film differs from that of the bulk, with a higher PSS content on top,[88, 95] where this layer has a thickness of ~10 Å for a PEDOT:PSS with a 1:6 PEDOT:PSS ratio.[95] The charge transport in the PEDOT:PSS film is given by Equation 4.1[96]

$$\sigma = \sigma_0 \exp[-\left(\frac{T}{T_0}\right)^{\frac{1}{2}}] \quad (4.1)$$

The conductivity pre-factor $\sigma_0 \sim c_{PEDOT}^{3.5}$ where c_{PEDOT} is the weight fraction of PEDOT in the PEDOT:PSS. In Equation 4.1, T is the temperature, T_0 is the characteristic temperature of PEDOT:PSS, and σ_0 is the conductivity pre-factor. It has also been found that the transport properties of the PEDOT:PSS film can be best described by variable range hopping (VRH) conduction through a percolation network of quasi-1D filaments.[97] This suggests that the current in a PEDOT:PSS film flows through quasi-1D PEDOT rich filaments which are embedded in a PSS rich matrix. Between these filaments, the charges must hop from one filament to another. Furthermore, the hopping sites may be single or aggregated PEDOT oligomers along an extended PSS chain.[97] The out-of-plane conductivity, α of PEDOT:PSS thin films has been described phenomenologically by the function

$$\alpha \sim \left[e^{[(\frac{d_0}{d})^{1/2}]} + R_s\right]^{-1} \quad (4.2)$$

where d is the diameter of a circular film, d_0 is a characteristic length scale of the PEDOT:PSS film, which is 100 μm for PEDOT:PSS with a 1:6 composition and $R_s \sim 6\ \Omega$ is a series resistance that accounts for the contact resistance between the electrode and the PEDOT:PSS.[98]



[99]

Figure 4.1. PSS(top) and PEDOT(bottom) in PEDOT:PSS film.

In order to improve the mechanical and barrier properties of polymer films, nanoscale clays have been introduced into the polymer. [100-109] Among various clay types, Montmorillonite (MMT) clay is a commonly studied clay, as it is easily exfoliated. MMT is a clay mineral consisting of stacked silicate sheets (thickness ~ 1 nm) with high aspect ratio and plate-like morphology. Chemically, MMT consists of two fused silicate tetrahedral sheets sandwiching an edge-shared octahedral sheet as shown in Figure 4.2. In the octahedral sheet, Al and Mg atoms are present in octahedral sites, which coordinate to O atoms and hydroxyl groups, forming the central layer of each clay sheet. In the tetrahedral sheet, Si and Al atoms occupy tetrahedral sites, also coordinating to O atoms. The sheets have a permanent negative charge due to isomorphous substitutions occurring mainly in the octahedral layer (e.g. Mg substituting Al in octahedral sheet, Al substituting Si in tetrahedral sheet). The outer edge of the sheet has a positive charge, though it is overpowered by the negative surface charge of the sheet and hence, has limited role in aggregation.[110] The charges of the sheets are balanced by Na^+ or Ca^{2+} cations intercalated between the silicate layers. [111]. MMT sheets balanced by Na^+ cations are most easily exfoliated in water. Hence, Sodium Montmorillonite (Na^+MMT^-) clay is used in this experiment.

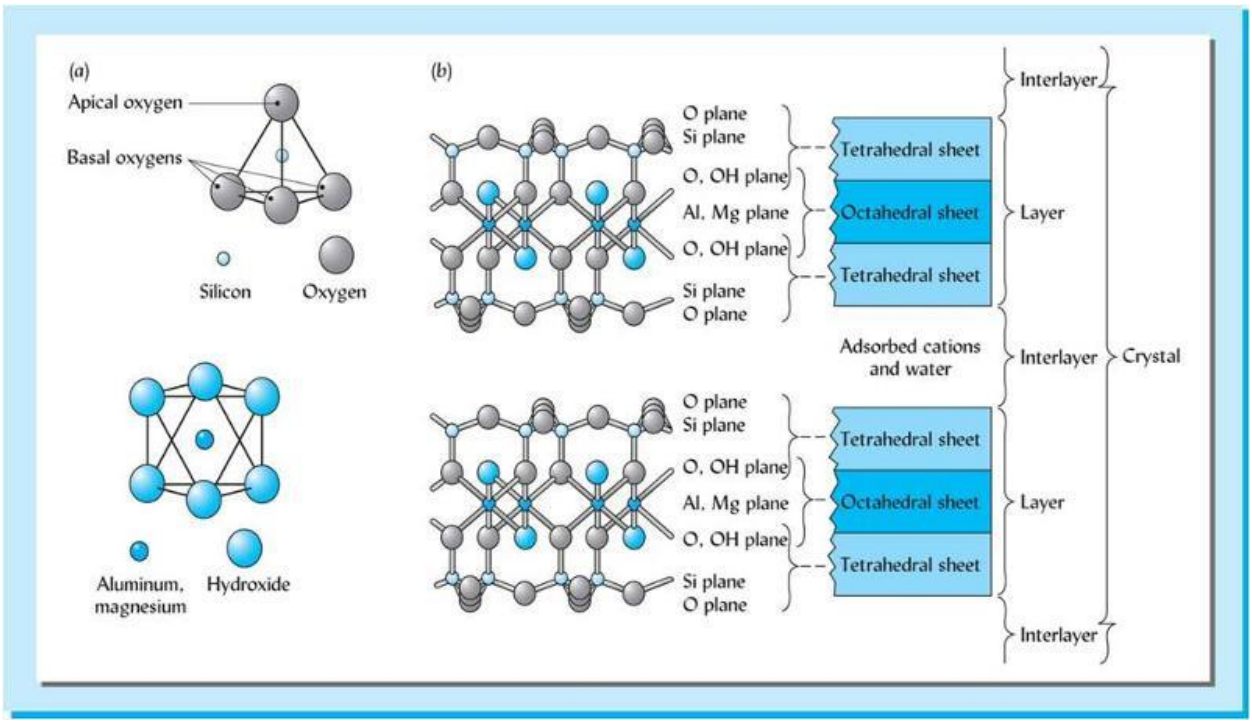


Figure 4.2. Schematic of Montmorillonite clay.[112]

Inclusion of the clay in PEDOT:PSS may therefore limit the transport of water in the PEDOT:PSS layer, which may improve the stability of the active layer in OPV solar cells where PEDOT:PSS is the hole transport layer. However, the inclusion of the clay may detrimentally impact the charge transport properties of the PEDOT:PSS, and therefore there is a need to understand the impact of the presence of the clay on the conductivity of the resultant nanocomposite. Therefore, experiments were completed to monitor the impact of the presence of clay in PEDOT:PSS thin films on their electrical conductivity and as a barrier to water vapor.

4.2 Experiments

Materials - PEDOT:PSS (CLEVIOS 4083) was purchased from Heraeus and Sodium Montmorillonite ($Na^{+}MMT^{-}$) clay was procured from Southern Clay. The ratio of PEDOT to PSS in this material is 1:6. Solutions that were used to fabricate thin films consist of 1.3-1.7 wt% in water with pH in the range of 1.5-2.5. In a separate solution, the clay is dispersed in water at 2.67 wt. %. To form the nanocomposite thin film, the PEDOT:PSS solutions was mixed with diluted clay solutions such that the after drying, films were created with the clay wt.% with respect to PEDOT:PSS of 0, 0.1%, 0.5%, 1%, 3%, 5%, 7% and 10%. The combined solution of PEDOT:PSS and clay was ultrasonicated for ~3 hours before spin coating.

Electrochemical Impedance Spectroscopy (EIS) - The combined solution of PEDOT:PSS and clay was spin coated onto a conductive grade ~1 in. × ~1 in. silicon wafer. The silicon wafers were ultrasonicated with highly pure water, then acetone and finally with alcohol each for ~20 minutes before film deposition. Then, these cleaned wafers were ozonized using a UV-Ozone cleaner (UVO Cleaner 48) for ~15 minutes to remove residual organic contaminants. On these cleaned wafers, rectangular bottom electrodes were vacuum deposited using a patterned mask using Varian 3118. The bottom electrode consisted of a 5 nm layer of Ti on the wafer which is further coated with a 50 nm layer of Au. Electrode deposition was then followed by spin coating the PEDOT:PSS and clay thin film at 2000 rpm for 90 seconds. The thickness of the PEDOT:PSS film was measured via Ellipsometry and determined to be ~70 nm. These films were then annealed at 120°C for 15 min to evaporate any residual water. The electrode dimensions of the top and bottom electrode are 1100 μm × 6100 μm. The gap between the electrodes top of the film is 400 μm, which allows for in-plane measurement of the conductivity.

Scanning electron microscopy (SEM) measurements – To image the dispersion of the clay in the PEDOT:PSS, the PEDOT:PSS nanocomposite film was spin coated on a silicon wafer. This wafer was then cut, air blown and glued to an SEM stub. The film did not require additional sputtering before imaging because of the good electrical conductivity of PEDOT:PSS films. A Zeiss Auriga SEM in the UT Microscopy Center was used to image the nanocomposite dispersion.

X-ray diffraction (XRD) measurements - The PEDOT:PSS and clay nanocomposite film was spin coated onto a cleaned silicon wafer at 2000 rpm for 90 seconds for XRD measurements. A Philips X'Pert diffractometer was used in this experiment, where it was utilized in the grazing incidence mode, which enables the efficient measurements of the local molecular ordering in thin films. The range of angle scanned in these experiments was from 0° to 40°.

Humidity measurements – The thin nanocomposite films that were monitored by EIS were subsequently heated for ~40 hrs at 120°C. Then, these nanocomposites that contain 0%, 0.1%, 5% and 10% clay were exposed to humidity in the range of 5%, 8%, 16%, 24% and 32% relative humidity. To control the level of exposure to humidity, each film was kept inside a small chamber (Linkam Stage LTS420) that contained probes which allowed the completion of the EIS measurement in various environments. The humidity in this chamber was controlled by the introduction of air with the targeted level of relative humidity (RH). The RH in the chamber was monitored using Fluke 971 temperature humidity meter. The system was allowed to equilibrate for approximately 2-3 minutes at each relative humidity before taking EIS measurements. In this analysis, relative humidity was increased monotonically until 32% and was done in air.

Quartz Crystal Microbalance (QCM) - To monitor the uptake of water upon exposure to a humid environment, quartz crystal microbalance measurements were completed. In these studies, the PEDOT:PSS solutions with 0 or 10% clay were spin coated at 2000 rpm for 90s onto 5 MHz quartz crystals. The oscillator, a SRS QCM 200 Controller, monitors the change in resonant frequency of the quartz crystal, which is dependent on the change in mass of the film on the crystal.

4.3 Results and discussion

The composition of the PEDOT:PSS used in this study has a 1:6 ratio of PEDOT:PSS by weight as it was found earlier that the percolation required for high conductivity requires a

PEDOT:PSS composition that is below 1:6 for thick films.[113] Another paper showed the percolation threshold for PANI (polyaniline)-PSS composite is quite low and the percolation threshold for polypyrrole coated on an insulating polymer is ~0.2 volume % for thin films with thickness of 20 nm.[114] For thick films, the probability of percolation, however, is less compared to thin films across the electrodes.

Further experiments also found that the simplest equivalent circuit that models the electrical behavior of PEDOT:PSS films with varying amounts of clay consists of a pseudo-capacitor and a resistor in parallel, which is in series with another pseudo-capacitor in parallel with another resistor, as shown in Figure 4.3. This model was also used to model another solid polymer electrolyte, although the relaxation processes are probably different in PEDOT:PSS.[115] In another study, EIS monitored the behavior of a Pt/PEDOT:PSS electrode with $Fe(CN)_6$ as an electrolyte. The model used in this work was also attempted to fit the data collected in this study, but with very little success. Using previous studies as guidance, and taking into account the fact that our system consists of conducting polymer PEDOT in association with a solid electrolyte (PSS^-Na^+/PSS^-H^+), the simplest model circuit interpretation for circuit elements shown in Figure 4.3, is as follows. CPE1 corresponds to the film's capacitance created by interfaces between the PEDOT rich phase and the PSS chains and also has contributions from the interface between the clay platelet and the PEDOT rich phase.[116] Moreover, the interface between the negatively charged clay or negatively charged PSS ion and the positively charged sodium ion may also lead to capacitance. The constant phase element (CPE) also describes the capacitance of the inhomogeneous film. R1 corresponds to film's resistance. CPE2 corresponds to the capacitance related to the formation of a double layer at the film surface. CPE2 is another constant phase element due to the non-uniformity of the double layer and R2 corresponds to the resistance at the film surface, which is related to ion diffusion and charge transfer at this interface. This model is required for all samples, including the pure PEDOT:PSS (i.e. 0% clay).[117] A Warburg diffusion component, which corresponds to ion movement, was not included in the model as there was no tail in the low frequency region and the range of frequency used to probe the system here was not as low as in the previous papers.[113, 117] The lowest frequency probed here was 100 mHz, which is sufficiently higher than the 1 mHz frequency probed in previous work. The lack of a low frequency tail may also be attributed to the fact that a thin film (nm) was used here compared to the thick films (μm) examined in previous studies.[117]



Figure 4.3. Equivalent circuit for the PEDOT:PSS + clay film.

The impedance corresponding to the CPE can be defined as $Z(\omega) = Q^{-1}(j \times \omega)^{-n}$ where Q becomes equal to capacitance when n = 1. Similar to a capacitor, the CPE keeps the phase constant with varying frequency, but the phase shift differs from 90°. The resistances or capacitances of each circuit elements are graphed below in Figures 4.4-4.9. At each clay loading, the values reported in these figures are the average of at least 3 different samples.

Previous studies have reported the in-plane conductivity of a PEDOT:PSS thin film at room temperature (300 K) as 17 Sm^{-1}[97] and ~8.5×10^{-3} Sm^{-1}.[92] In the current experiment, the in-plane conductivity of the PEDOT:PSS film without clay was found to be ~15×10^{-2} Sm^{-1}. This value is calculated from $\sigma = Rwh/l$, where R is the film resistance, w is the width of the electrode in contact with film, h is the thickness of film, and l is the gap between the two electrodes.[113] This variation could be because of the different thickness, dimension of electrode and gap between electrodes. Moreover, in the previous work,[97] the electrodes used for the in-plane conductivity measurement are at the film bottom, while in our experiment and in reference [92], they are on the top of the film.

The data in Figure 4.4 shows that the film resistance doubles (from ~3.5×10^{7} Ω to ~7.4×10^{7} Ω) with the inclusion of 0.1% clay. This can be understood as due to an increase in pathway length that an electron must take in order to transport between the electrodes with the inclusion of the clay. Figure 4.10 illustrates the more tortuous pathway that is required due to the presence of the clay. Interestingly, as the clay concentration is increased up to 5%, the resistance varies only slightly, but continue to increase only above 5% clay loading. This is attributed to the percolation behavior of polymer clay nanocomposites, where ~ 5% clay loading is defined as the percolation limit. Below this limit, there exist open pathways for the electron to transport across the film without encountering a clay particle. Above this limit, however, the percolation of the clay nanoparticles introduces additional barriers to electron transport across the film. This behavior is exemplified by the steady increase in resistance with an increase in clay loading to

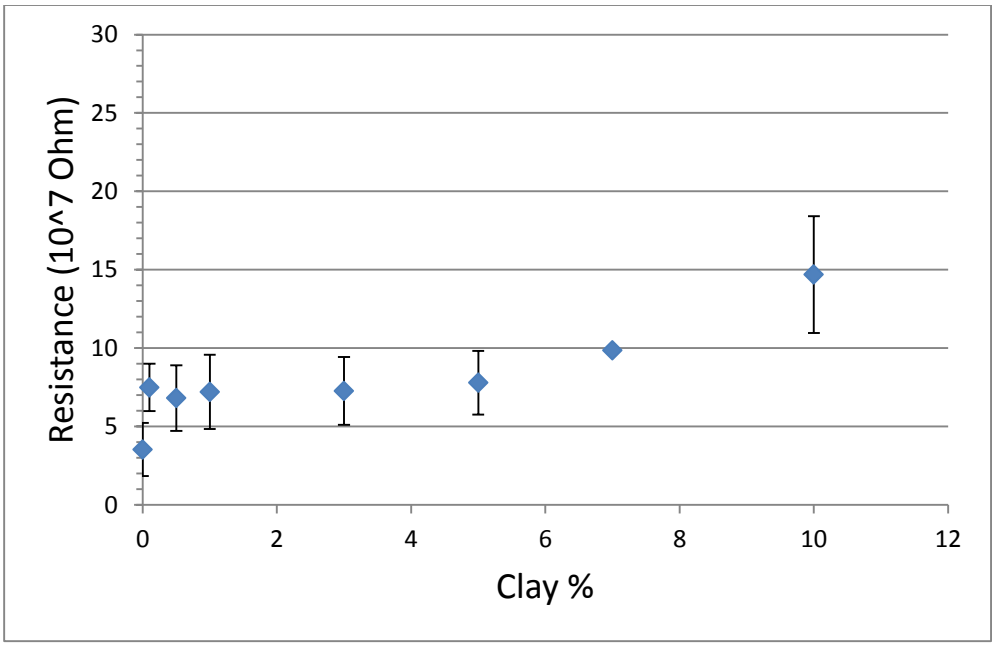


Figure 4.4. The change in PEDOT:PSS film resistance with clay loading.

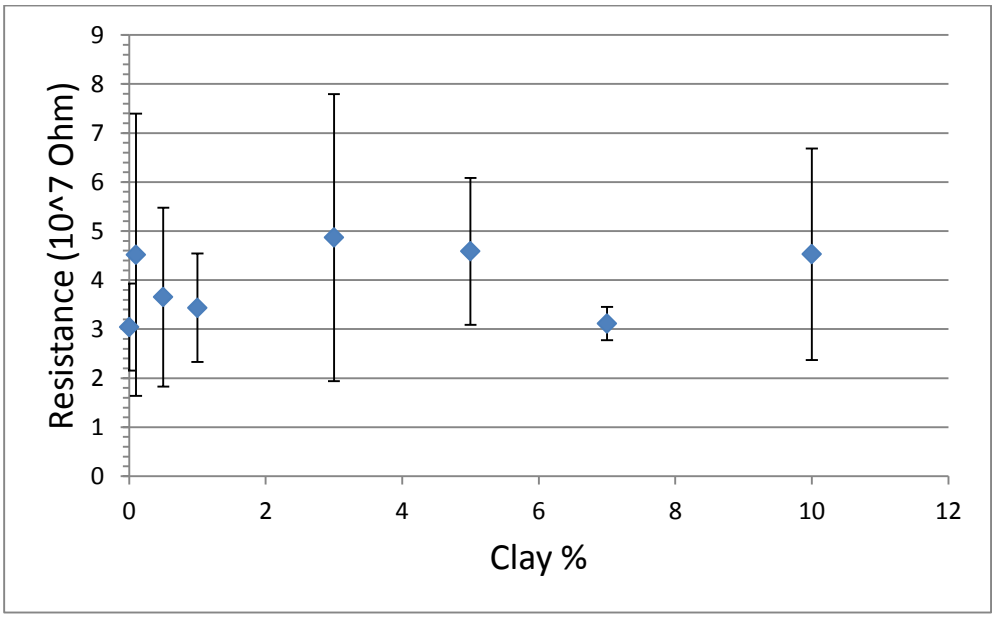


Figure 4.5. The change in the charge transfer resistance of the film interface with electrode with variation of clay loading.

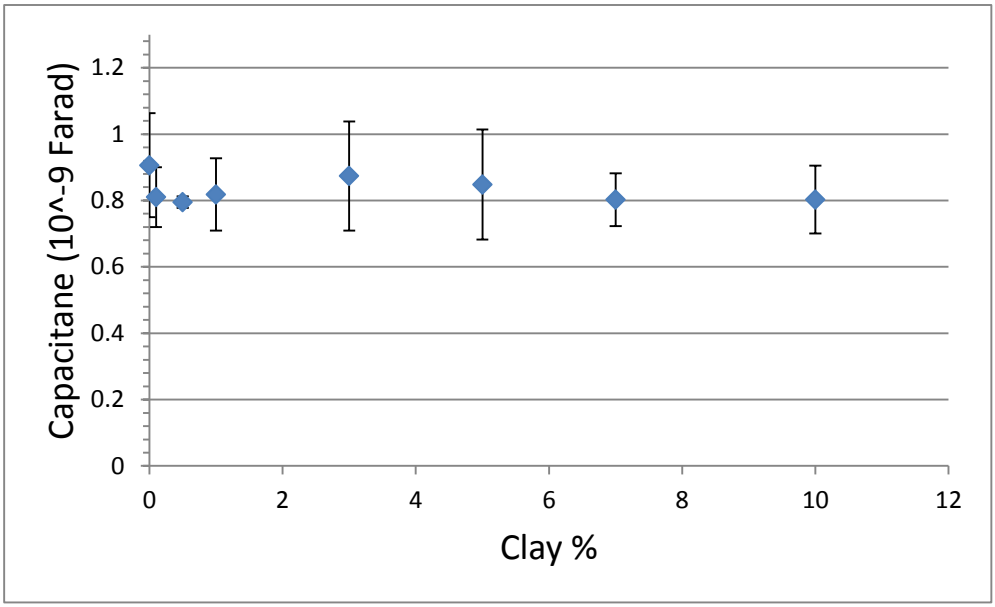


Figure 4.6. Change in the film capacitance with variation of clay loading.

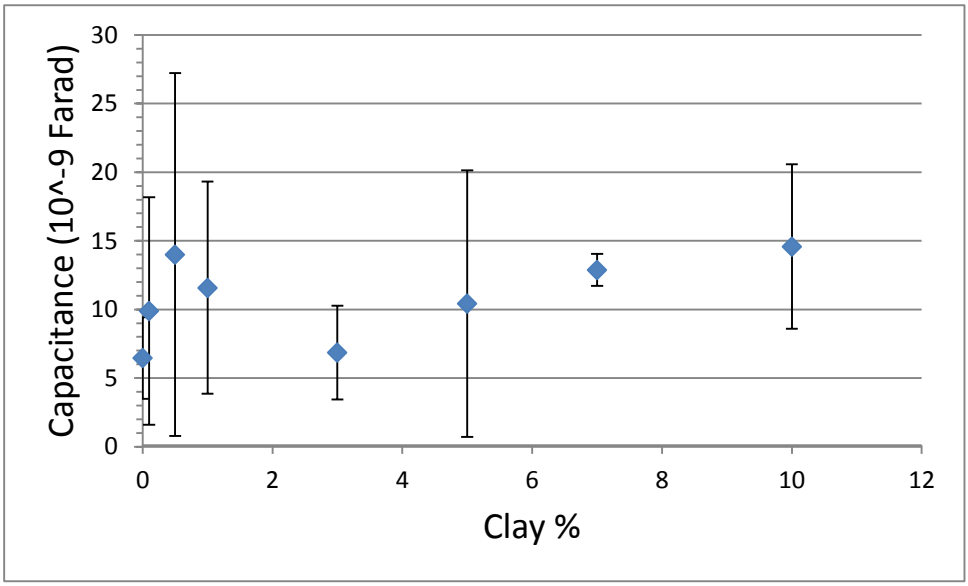


Figure 4.7. Change in the double layer capacitance with a variation of clay loading.

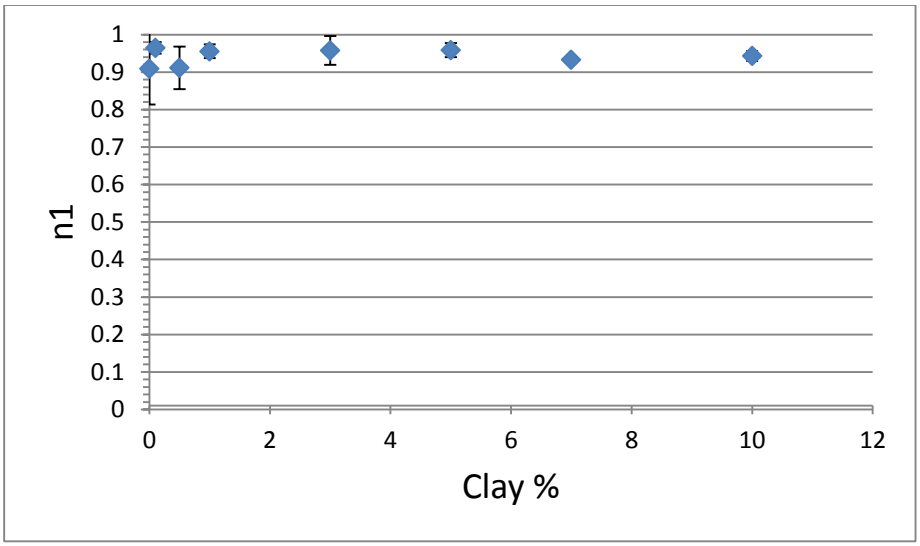


Figure 4.8. The change in the exponent corresponding to the phase change, n1 with a change in the loading of clay.

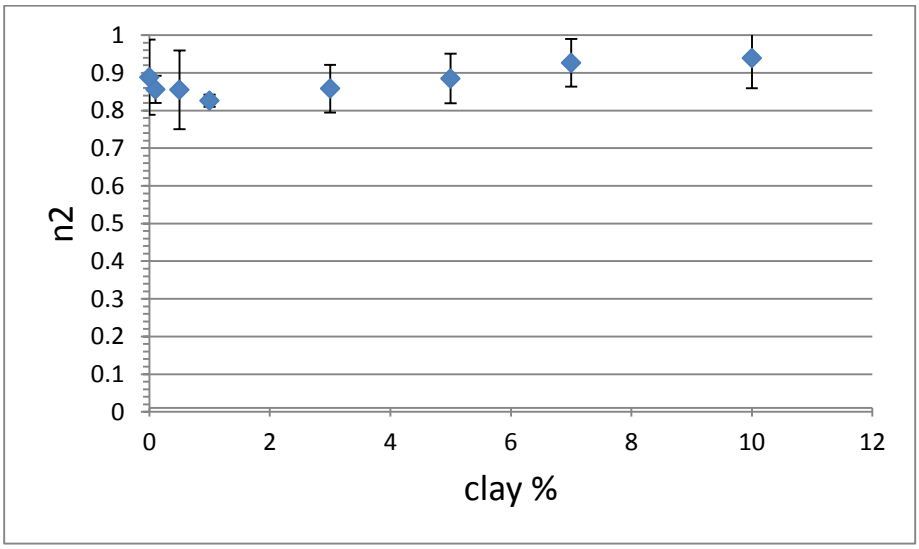


Figure 4.9. The change in the exponent corresponding to the phase change, n2 with a change in the loading of clay.

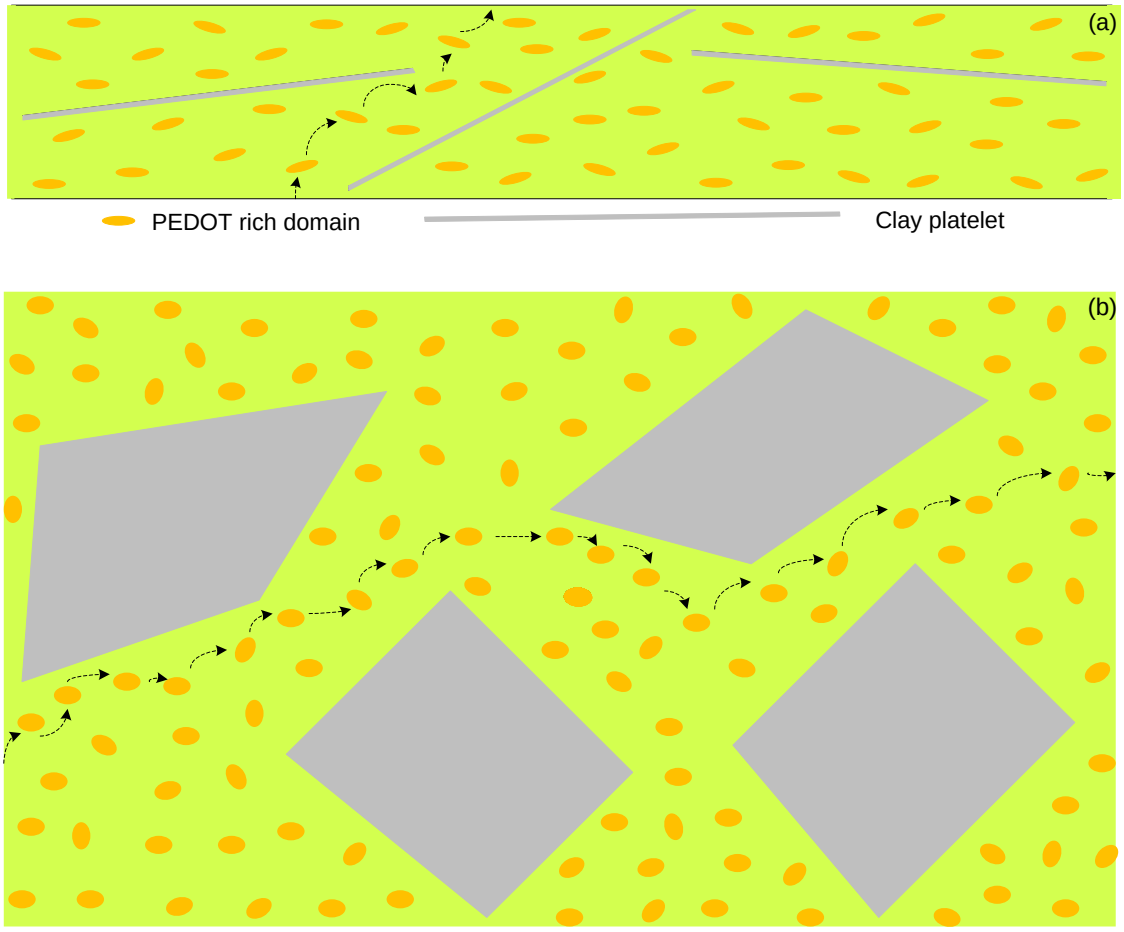


Figure 4.10. (a) Schematic of PEDOT:PSS and clay thin film when viewed from the side (b) Schematic of PEDOT:PSS and clay thin film when viewed from the top.

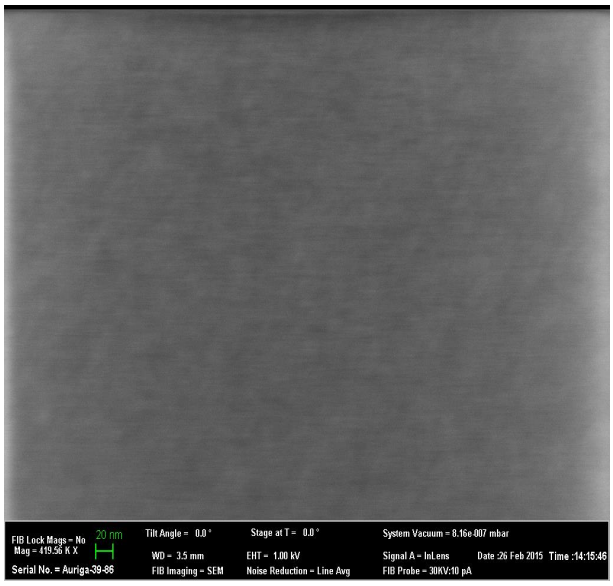
7% and 10%. The average charge transfer resistance across the film and at the electrode interface doesn't vary appreciably with clay loading, though the uncertainty in the data is high (Figure 4.5). As per Figure 4.6, the film capacitance lies in the narrow range of 0.7-1 nF with little variability with clay loading. Therefore, it can be concluded that the capacitance across the film is independent of clay loading. The data in Figure 4.7 shows that the double layer capacitance increases with clay loading from 0% to 0.5%, but decreases with increased clay loading up to 3%. On further increasing clay %, capacitance increases again. The large uncertainty in the data at low clay loadings suggests that this trend is also consistent with a modest increase at the lowest loadings, followed by a leveling off up to 5% clay, and a further increase at higher clay loadings. This pattern is consistent with behavior that is dominated by the percolation of the clay. The large variation in the double layer capacitance may be attributed to random deviation of the clay platelets' presence near interface. Based on Figure 4.8 and Figure 4.9, values of n1 lies between 0.9 and 1 for all samples, while the values of n2 lies between 0.8 and 0.9, both of which indicate that the constant phase elements are behaving nearly as ideal capacitors.

It was difficult to fit the EIS data obtained when measuring the current across the film. However, the resistances obtained from the low frequency intercept of Bode plots across the film were mostly in the range of 2-5 Ω, which may be attributed to a combination of the contact resistance and film resistance. Assuming an impedance of 3 Ω, the conductivity of the film (1.1 mm × 1.1 mm) across the plane is ~52 S/m. Moreover, the Bode plot for one electrode resembles that of the current across the plane. In some cases, the resistance across the film was very high, in the range of 100 kΩ to 100 MΩ, which may be attributed to the presence of large barriers to transport between the electrodes. It is interesting that previous studies monitored the conductivity across thin PEDOT:PSS films utilized films that were between 1 μm-100 μm,[98] suggesting that out-of-plane conductivity measurements require samples that are less than 100 μm in size. Given that our samples do not fit this requirement, the out of plane data was not further analyzed.

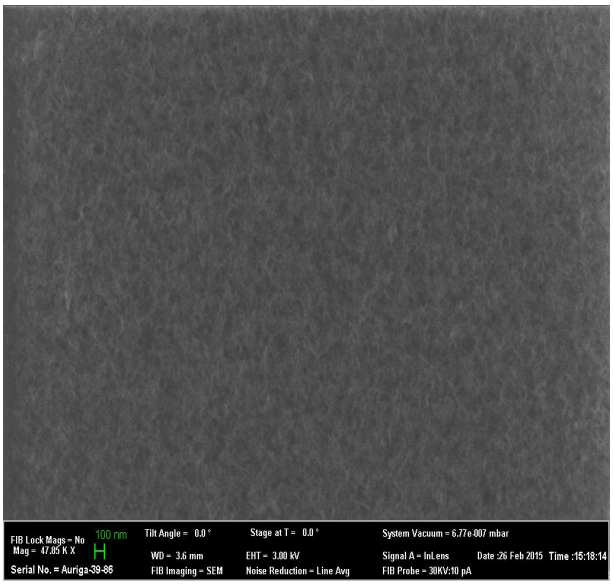
4.3.1 Morphology of the PEDOT:PSS clay Nanocomposites

To verify the dispersion of the clay in the PEDOT:PSS, SEM and x-ray diffraction experiments were completed. The SEM images of the measured PEDOT:PSS clay nanocomposites for the samples with 0, 0.5, 1, 5, and 10% clay loadings is shown in Figure 4.11. The scale bar in Figure 4.11(a) is 20 nm and any structural heterogeneity can be attributed to be

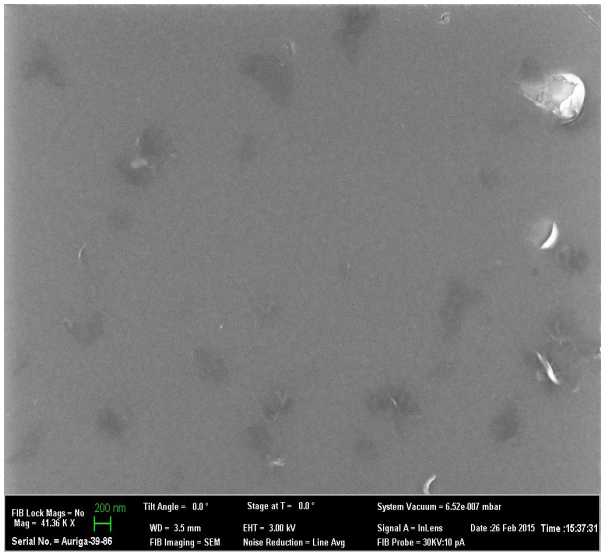
Figure 4.11. SEM images of the PEDOT:PSS films containing various clay loadings.



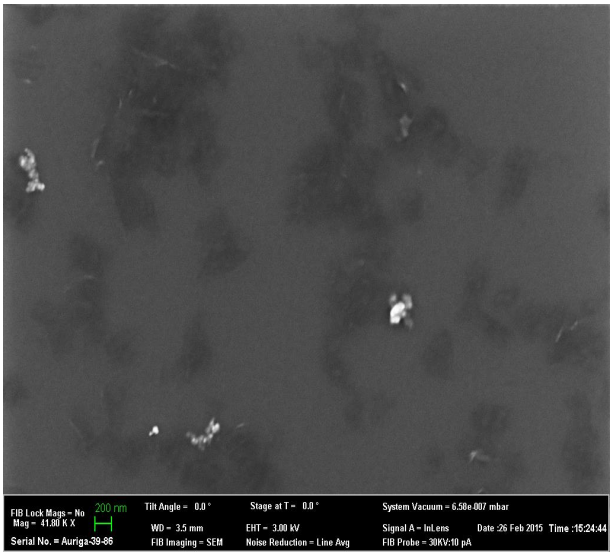
(a) The SEM image of the pure PEDOT:PSS film.



(b) The SEM image of the PEDOT:PSS film containing 0.5 wt% clay.

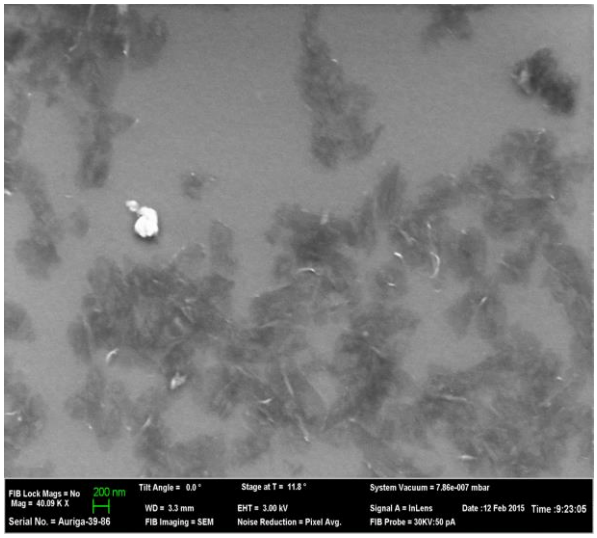


(c) The SEM image of the PEDOT:PSS film containing 1% clay.



(d) The SEM image of the PEDOT:PSS film containing 5 wt% clay.

Figure 4.11 continued.



(e) The SEM image of the PEDOT:PSS film containing 10 wt% clay.

Figure 4.11 continued

PEDOT rich domains and PSS rich domains. In Figure 4.11(b), the scale bar is 100 nm and while there is modest contrast between the PSS and PEDOT, there is no indication of clay aggregates. In Figures 4.11 (c), (d), and (e), the scale bar is 200 nm and both individual and small clay aggregates are visible, with more aggregates visible at higher clay loadings. Analysis of these images indicates that the approximate size of the platelets are ~200 nm × 200 nm, which is similar to the dimensions reported in previous studies.[111] The SEM images shows that even until 1% clay composition, clay platelets are almost in exfoliated state. PEDOT:PSS films with 5% and 10% clay loading show clay aggregation. However, as the SEM image gives information about the surface only, X-ray diffraction is required to provide a more accurate measure of the clay dispersion.

The x-ray diffraction plot of the pure clay and its nanocomposites with PEDOT:PSS at loadings of 1 and 10% is shown in Figure 4.12. The pure clay diffraction plot shows a clear peak at ~ 7°, which corresponds to a d-spacing of 12.6 Å. Figure 4.13 shows the diffraction patterns of the four samples with a focus on the peak position, which shows that there is small peak at ~ 6.4° corresponding to 13.9 Å d-spacing is evident for the sample with 10% clay loading. The increased d-spacing could be attributed to intercalated clay platelets. The lack of peak for 1% clay containing film is indicative of completely exfoliated clay platelets. Similar d-spacing have previously been reported for unmodified clay.[101, 118, 119]

4.3.2 Barrier properties of the PEDOT:PSS Nanocomposites

Previous studies have shown that a primary cause of degradation of polymer solar cells that incorporate PEDOT:PSS as a hole transport layer is water absorption by the hygroscopic PEDOT:PSS layer.[18, 120] Similarly, a pure thin clay film has been considered as a barrier to the diffusion of indium, oxygen and moisture between the PEDOT:PSS layer and the photoactive layer.[121] Therefore, one of the goals of incorporation of the clay into the PEDOT:PSS layer is to improve its barrier properties to gas diffusion esp. water vapor. Therefore, the impact of the exposure of PEDOT:PSS thin films to humidity was also monitored. Because the resistance of the films did not change much when varying the clay loading from 0.1% and 5%, the electrical performance of the films containing clay loadings of 0, 0.1%, 5% and 10% were determined via EIS with varying humidity. The parameters that derive from the analysis of the EIS data for these 4 samples with exposure to humidity are presented in Figures 4.14-4.18. Prior to exposure to the

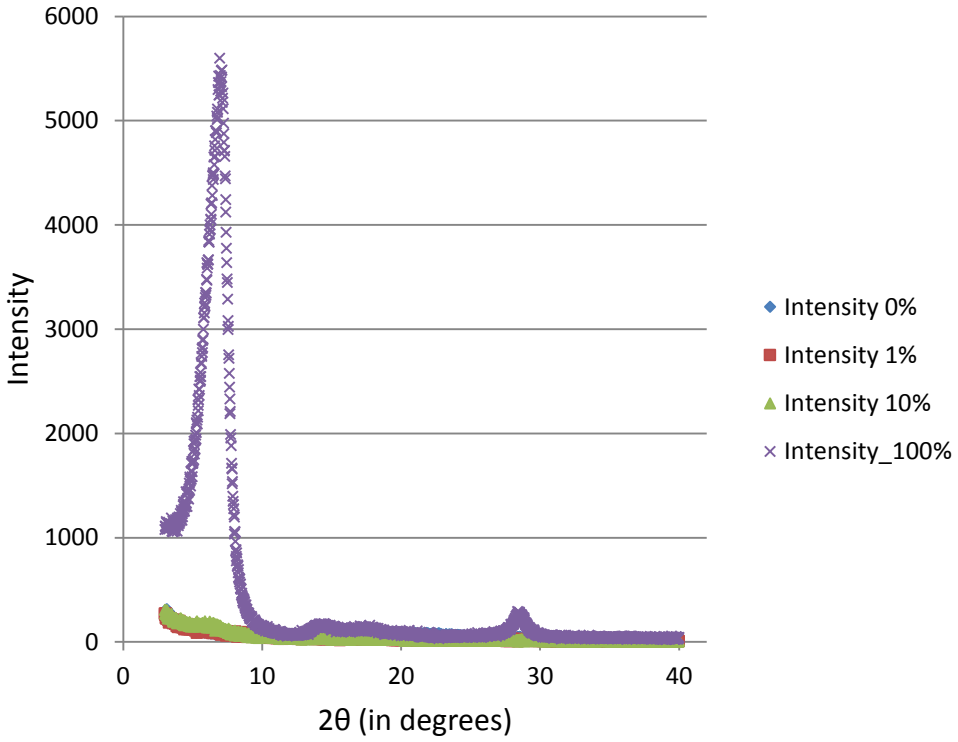


Figure 4.12. XRD plot of PEDOT:PSS film with 0%, 1%, 10% and 100% clay.

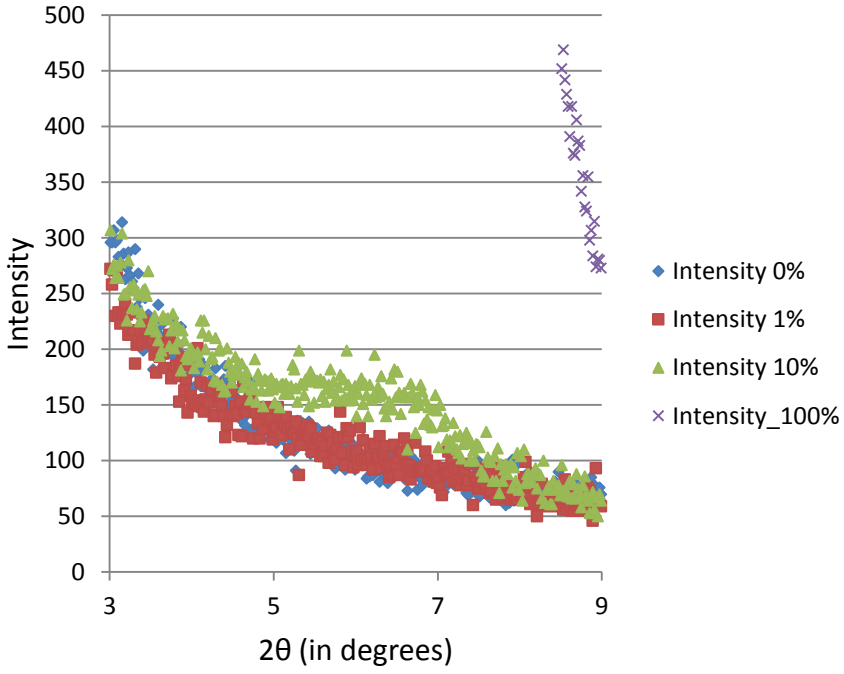


Figure 4.13. XRD plot of PEDOT:PSS film with 0%, 1%, 10% and 100% clay with a focus on the peak position.

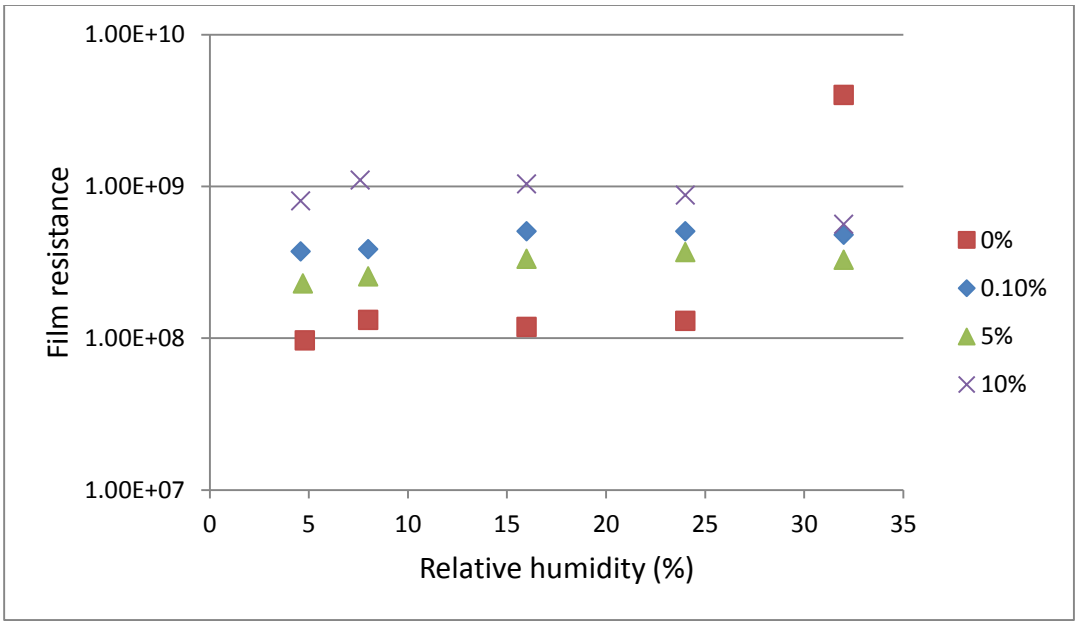


Figure 4.14. Change in PEDOT:PSS bulk film resistance with relative humidity for nanocomposites with 0%, 0.1%, 5%, and 10% clay loadings.

humidity chamber, the PEDOT:PSS nanocomposites were annealed at 120°C for ~40 hours under partial vacuum to eliminate any residual water in the film. As shown in Figure 4.14, the variation in the conductivity of the PEDOT:PSS films with clay loading mimic the behavior displayed in Figure 4.4 i.e. the film resistance for the pure PEDOT:PSS film is the lowest, while the film resistance of the nanocomposites with 0.1% and 5% clay are similar and slightly higher than that of the pure film, and the resistance of the film with 10% clay is quite high. The resistance for all the films has increased by an order of magnitude as a result of prolonged annealing at 120 °C. This is contrary to the result obtained in other studies where the conductivity increased as a result of annealing,[122, 123] though the duration of the heating was quite low in these previous studies, usually only minutes compared to the many hours here. Moreover, the glass transition temperature of PSS is ~109 °C[124] which might lead to an increase in an increase in PSS phase separation over these extended annealing times.

The results in Figure 4.14 show that increasing the relative humidity up to 25%, results in a gradual increase in the resistance of the films with 0%, 0.1% or 5% clay, which is in agreement with previous studies.[99, 122] This increase has been attributed to increase in distances between PEDOT domains as a result of the swelling of the film by water uptake. However, the resistance

of the 10% clay film changes very little with the increase in relative humidity. Upon increasing the relative humidity to > 30%, the resistance of the pure PEDOT:PSS film increases by an order of magnitude, whereas the resistance of all clay containing nanocomposite films decrease. The increase in the resistance of pure PEDOT:PSS film may be attributed to the reduction in the number of percolating [PEDOT] pathways that are possible due to the swelling of the PSS. For clay containing nanocomposite films, the reduction of resistance may be the result of the participation of ions from clay in the conduction process, which may be induced by the exfoliation of clay aggregates by additional water present in the thin film.

The data in Figure 4.15 indicates that the charge transfer resistance increases with clay loading in each film up to 25% relative humidity (RH). Moreover, the charge transfer resistance increases gradually with relative humidity for the 0, 0.1% and 5% clay loaded films up to 25% RH. Similar to the resistance data shown in Figure 4.14, above 30% RH, the charge transfer resistance for the pure PEDOT:PSS film increases significantly, while it decreases slightly for all of the nanocomposite films. This behavior is consistent with the explanation described above, i.e. the increase in the charge transfer resistance of the pure PEDOT:PSS film is attributed to reduced amount of PEDOT domains in contact with electrode due to swelling by water.

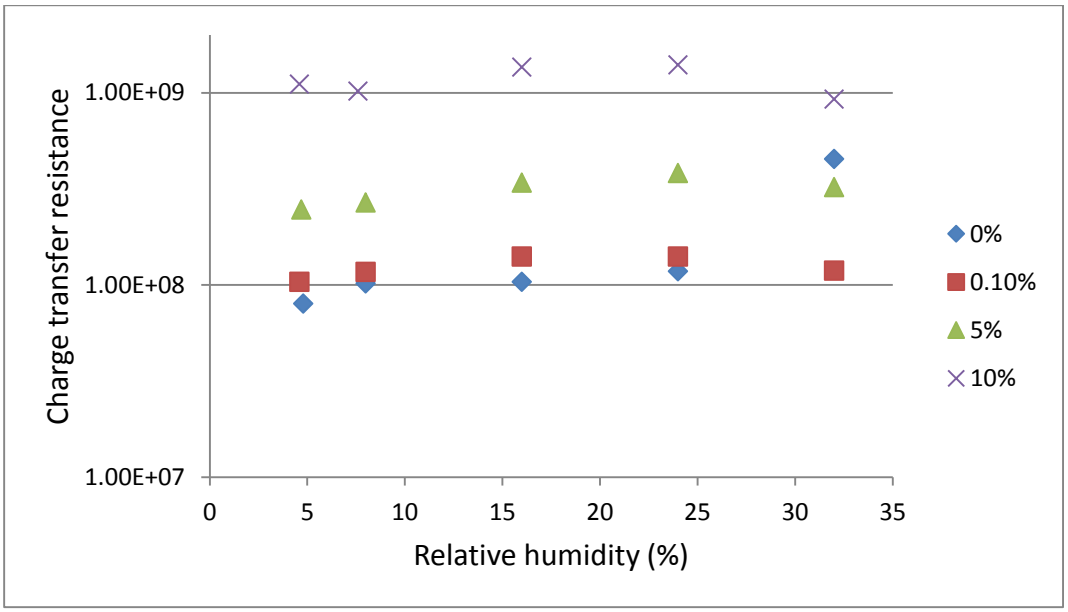


Figure 4.15. Change in PEDOT:PSS charge transfer resistance with relative humidity for nanocomposites with 0%, 0.1%, 5%, and 10% clay loadings.

The data presented in Figure 4.16 shows that the film capacitance remains nearly constant with clay loading and exposure to a humid environment, which is a similar trend to that which was observed in Figure 4.6. However, as in Figure 4.14 and 4.15, this data shows that the electrical behavior of the pure PEDOT:PSS sample changes dramatically when exposed to a RH that is greater than 30%. This decrease of capacitance is also consistent with an increased distance between PEDOT rich domains due to swelling.

It is difficult, however, to explain the dependence of the double layer capacitance with relative humidity as shown in Figure 4.17. This data shows that the double layer capacitance increases for 0.1% clay loading, but decreases below that of the pure PEDOT:PSS film for the 5% and 10% clay loaded samples, but changes little with exposure to humidity. One explanation may be that there is a random distribution of clay near the surface irrespective of clay loading.

The data presented in Figure 4.18 shows that the values of n1 for all samples and all humidity levels are in the range of 0.95-1, indicating that these films are nearly behaving as ideal capacitors. The values of n2 are also in the range of 0.79-0.83 for all the 0.1% and 5% clay nanocomposite films at all relative humidities, while the 10% clay nanocomposites shows an n2 value of 0.85-0.95 for all humidities. As observed in previous parameters, the pure PEDOT:PSS film that is exposed to > 30 % relative humidity exhibits a different response, n2 is 0.63.

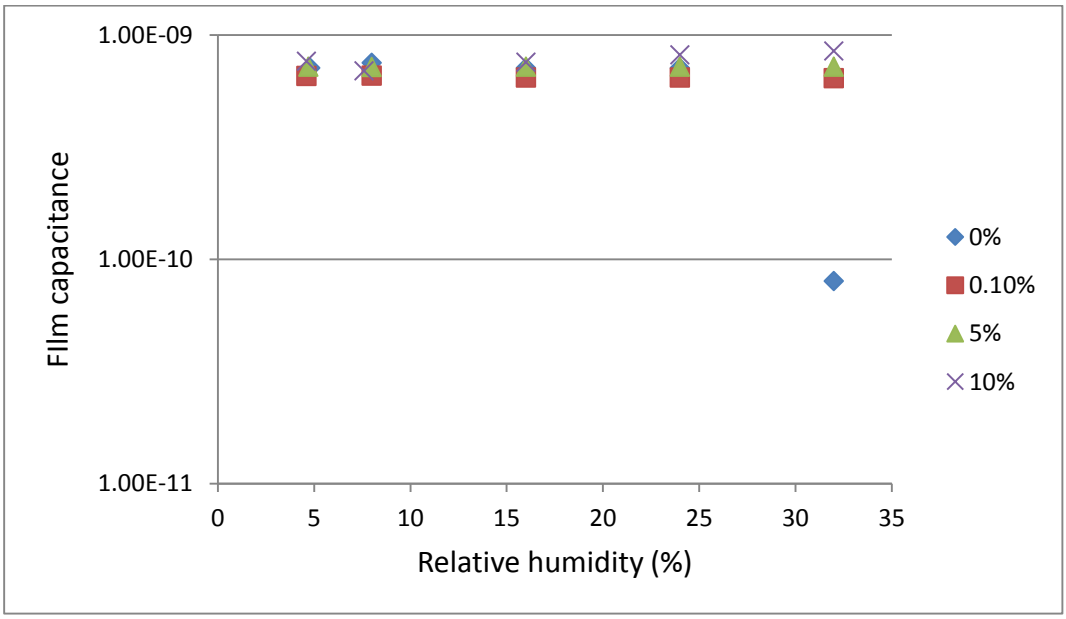


Figure 4.16. Change in PEDOT:PSS film capacitance with relative humidity for nanocomposites with 0%, 0.1%, 5%, and 10% clay loadings.

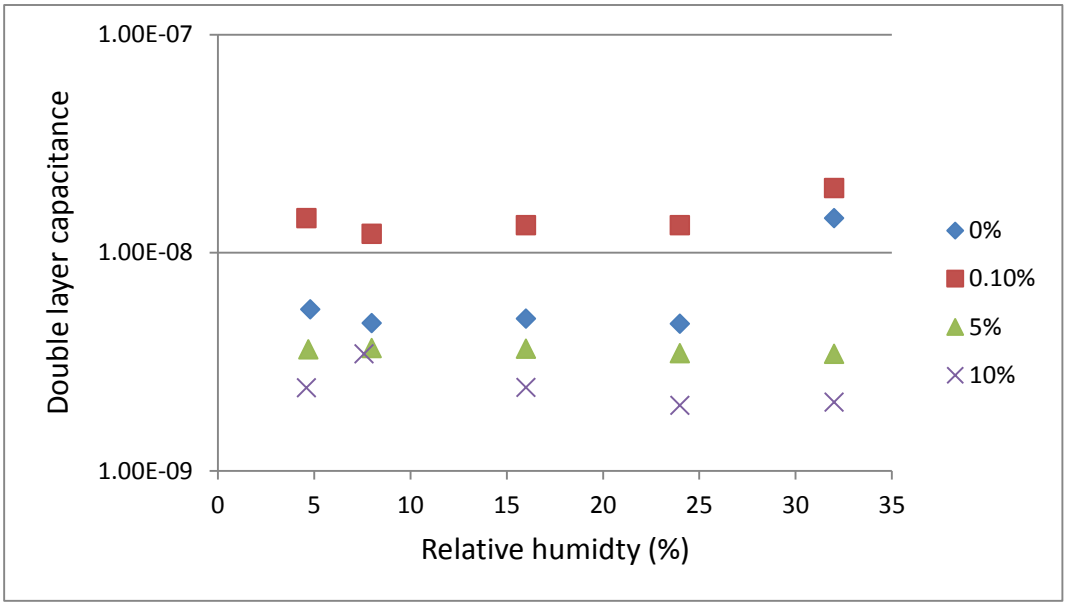


Figure 4.17. Change in PEDOT:PSS double layer capacitance with relative humidity for nanocomposites with 0%, 0.1%, 5%, and 10% clay loadings.

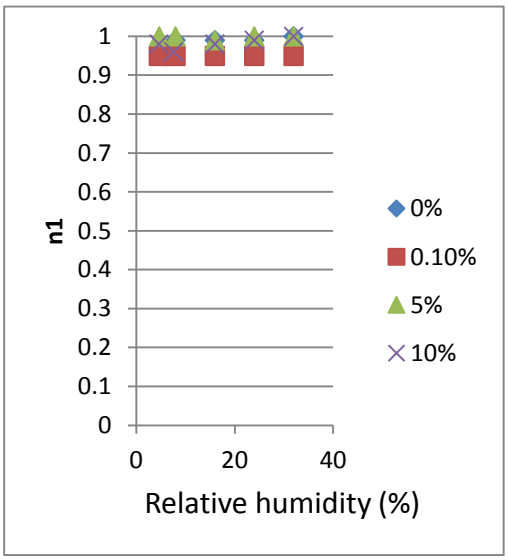
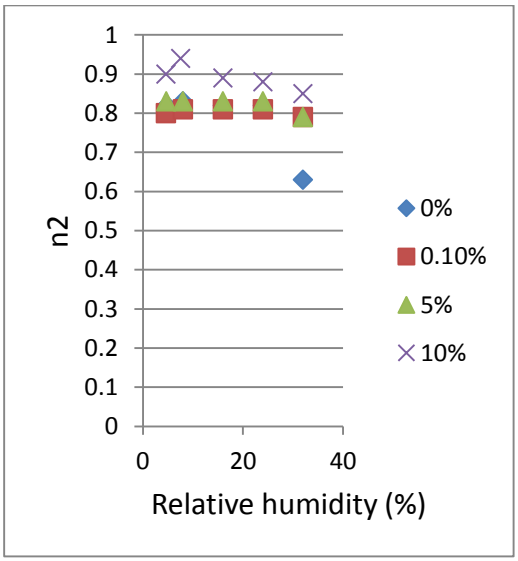


Figure 4.18. (a) Change in the n1 value of PEDOT:PSS with relative humidity for nanocomposites with 0%, 0.1%, 5%, and 10% clay loadings.



(b) Changes in the n2 value of the PEDOT:PSS with relative humidity for nanocomposites with 0%, 0.1%, 5% and 10% clay loadings.

Finally, the time response of the PEDOT:PSS thin films and the clay nanocomposites to an applied pulse of humidity was monitored. In this experiment, a pulse of humidity is introduced into the measurement chamber for ~20 minutes followed by a ~80 minutes delay before the next pulse. The magnitude of humidity pulse increases with each consecutive humidity pulse as shown in Figure 4.19.

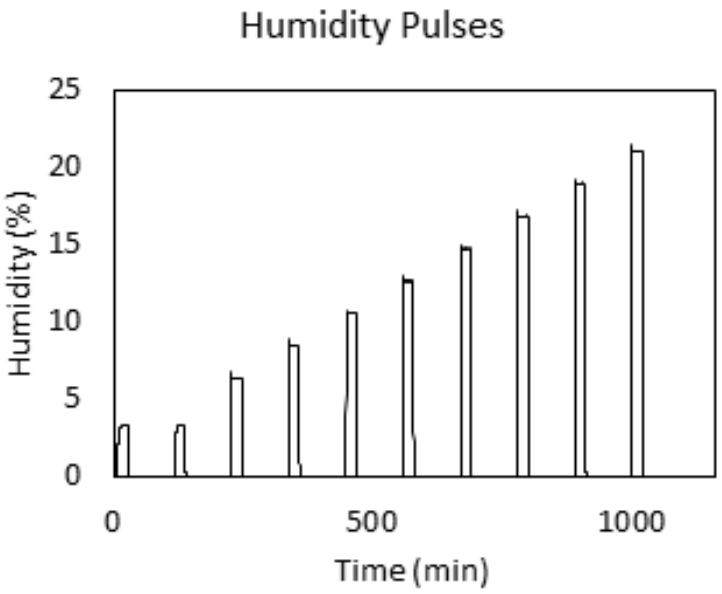


Figure 4.19. Time evolution of the humidity in the pulsed sequence.

The change in the mass of the pure PEDOT:PSS and the 10% clay PEDOT:PSS nanocomposite was monitored during this humidity sequence, where these results are shown in Figure 4.20. The resistance of these two films was also followed as a function of the exposure to humidity, where this data is shown in Figure 4.21. Figures 4.20 and 4.21 show that the mass and resistance of both films increases with exposure to humidity for both films. It is surprising that the relative increase in the mass of the 10% clay film is greater than that of the pure PEDOT:PSS film during the humidity pulse. It is interesting, however, that the mass of the 10% clay loading nanocomposite decreases to a lower value than the pure film, suggesting that the water is not able to penetrate the film as thoroughly in the nanocomposite film. Another surprising result was that the relative increase in resistance is higher in the 10% clay film. It is difficult to explain these observations. Further experiments may be conducted with varying humidity pulses in order to more thoroughly understand these results.

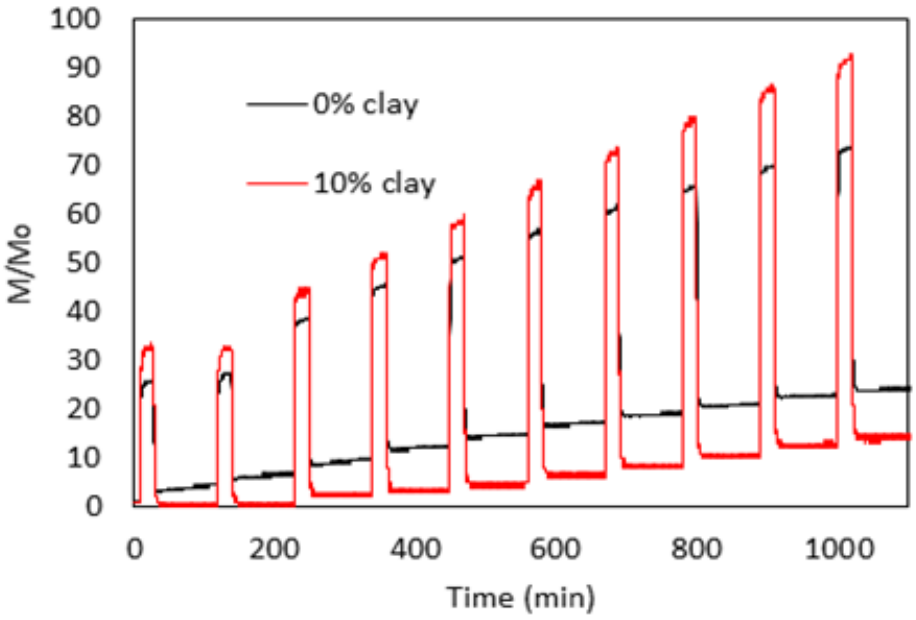


Figure 4.20. Mass change of the PEDOT:PSS thin film and 10% clay nanocomposite with time due to the introduction of humidity.

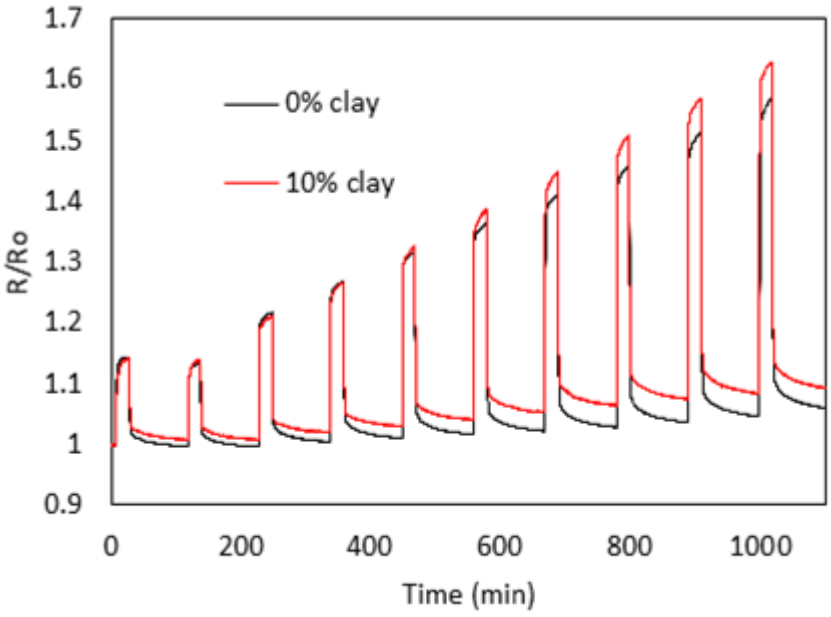


Figure 4.21. Resistance change with time due to humidity.

4.4 Conclusion

As the weight of PEDOT:PSS increases by ~20%[123] from exposure to an ambient environment, incorporating clay into the film could be an effective solution that will improve the longevity of electronic devices that incorporate of PEDOT:PSS films. The results reported in this chapter show that the incorporation of clay in the PEDOT:PSS films up to ~ 5% does not alter the resistance of the film appreciably. This may be due to the fact that the percolation limit of the clay platelets is around 5%, where an increase in clay aggregation is observed at 10% with XRD. The data also show that the film resistance increases with humidity for all the films studied up to 25% relative humidity. The importance of the clay, however, becomes clear when the humidity increases above 30%, where the pure PEDOT:PSS film shows a dramatic decline in performance and that this is not observed in the PEDOT:PSS clay nanocomposite thin films. Film capacitance and double layer capacitance behaved nearly as an ideal capacitor irrespective of clay loading. Film capacitance varied negligibly with clay loadings. PEDOT:PSS film with 10% clay loading showed less water absorption with humidity pulses. Further mechanical tests of the film can provide additional insights into the effect of clay and relative humidity on the change in the mechanical strength and film flexibility with clay inclusion.

References

1. Shafiee, S. and E. Topal, *When will fossil fuel reserves be diminished?* Energy policy, 2009. **37**(1): p. 181-189.
2. Lewis, N.S., *Toward cost-effective solar energy use.* science, 2007. **315**(5813): p. 798-801.
3. Kalowekamo, J. and E. Baker, *Estimating the manufacturing cost of purely organic solar cells.* Solar Energy, 2009. **83**(8): p. 1224-1231.
4. Krebs, F.C., H. Spanggard, T. Kjær, M. Biancardo, and J. Alstrup, *Large area plastic solar cell modules.* Materials Science and Engineering: B, 2007. **138**(2): p. 106-111.
5. Krebs, F.C., *Roll-to-roll fabrication of monolithic large-area polymer solar cells free from indium-tin-oxide.* Solar Energy Materials and Solar Cells, 2009. **93**(9): p. 1636-1641.
6. Krebs, F.C., T. Tromholt, and M. Jørgensen, *Upscaling of polymer solar cell fabrication using full roll-to-roll processing.* Nanoscale, 2010. **2**(6): p. 873-886.
7. Coakley, K.M. and M.D. McGehee, *Conjugated polymer photovoltaic cells.* Chemistry of materials, 2004. **16**(23): p. 4533-4542.
8. Krebs, F.C., M. Jørgensen, K. Norrman, O. Hagemann, J. Alstrup, T.D. Nielsen, J. Fyenbo, K. Larsen, and J. Kristensen, *A complete process for production of flexible large area polymer solar cells entirely using screen printing—first public demonstration.* Solar Energy Materials and Solar Cells, 2009. **93**(4): p. 422-441.
9. Scharber, M. and N. Sariciftci, *Efficiency of bulk-heterojunction organic solar cells.* Progress in polymer science, 2013. **38**(12): p. 1929-1940.
10. Li, G., R. Zhu, and Y. Yang, *Polymer solar cells.* Nature Photonics, 2012. **6**(3): p. 153-161.
11. Scharber, M.C., D. Mühlbacher, M. Koppe, P. Denk, C. Waldauf, A.J. Heeger, and C.J. Brabec, *Design rules for donors in bulk-heterojunction solar cells—Towards 10% energy-conversion efficiency.* Advanced Materials, 2006. **18**(6): p. 789-794.
12. Credgington, D., F.C. Jamieson, B. Walker, T.Q. Nguyen, and J.R. Durrant, *Quantification of Geminate and Non-Geminate Recombination Losses within a Solution-Processed Small-Molecule Bulk Heterojunction Solar Cell.* Advanced Materials, 2012. **24**(16): p. 2135-2141.
13. Cowan, S.R., A. Roy, and A.J. Heeger, *Recombination in polymer-fullerene bulk heterojunction solar cells.* Physical Review B, 2010. **82**(24): p. 245207.
14. Pal, S.K., T. Kesti, M. Maiti, F. Zhang, O. Inganäs, S. Hellström, M.R. Andersson, F. Oswald, F. Langa, and T. Österman, *Geminate charge recombination in polymer/fullerene bulk heterojunction films and*

implications for solar cell function. Journal of the American Chemical Society, 2010. **132**(35): p. 12440-12451.
15. Pivrikas, A., N. Sariciftci, G. Juška, and R. Österbacka, *A review of charge transport and recombination in polymer/fullerene organic solar cells.* Progress in Photovoltaics: Research and Applications, 2007. **15**(8): p. 677-696.
16. Blom, P.W., V.D. Mihailetchi, L.J.A. Koster, and D.E. Markov, *Device physics of polymer: fullerene bulk heterojunction solar cells.* Advanced Materials, 2007. **19**(12): p. 1551-1566.
17. Mayer, A.C., S.R. Scully, B.E. Hardin, M.W. Rowell, and M.D. McGehee, *Polymer-based solar cells.* Materials today, 2007. **10**(11): p. 28-33.
18. Nikiforov, M.P., J. Strzalka, and S.B. Darling, *Delineation of the effects of water and oxygen on the degradation of organic photovoltaic devices.* Solar Energy Materials and Solar Cells, 2013. **110**: p. 36-42.
19. Chen, H.-Y., J. Hou, S. Zhang, Y. Liang, G. Yang, Y. Yang, L. Yu, Y. Wu, and G. Li, *Polymer solar cells with enhanced open-circuit voltage and efficiency.* Nature Photonics, 2009. **3**(11): p. 649-653.
20. Duan, C., F. Huang, and Y. Cao, *Recent development of push–pull conjugated polymers for bulk-heterojunction photovoltaics: rational design and fine tailoring of molecular structures.* Journal of Materials Chemistry, 2012. **22**(21): p. 10416-10434.
21. Chen, H., J. Peet, S. Hu, J. Azoulay, G. Bazan, and M. Dadmun, *The Role of Fullerene Mixing Behavior in the Performance of Organic Photovoltaics: PCBM in Low-Bandgap Polymers.* Advanced Functional Materials, 2014. **24**(1): p. 140-150.
22. Treat, N.D., M.A. Brady, G. Smith, M.F. Toney, E.J. Kramer, C.J. Hawker, and M.L. Chabinyc, *Interdiffusion of PCBM and P3HT reveals miscibility in a photovoltaically active blend.* Advanced Energy Materials, 2011. **1**(1): p. 82-89.
23. Thompson, B.C. and J.M. Frechet, *Polymer–fullerene composite solar cells.* Angewandte chemie international edition, 2008. **47**(1): p. 58-77.
24. Hoppe, H. and N.S. Sariciftci, *Morphology of polymer/fullerene bulk heterojunction solar cells.* Journal of Materials Chemistry, 2006. **16**(1): p. 45-61.
25. Chen, H., Y.-C. Hsiao, B. Hu, and M. Dadmun, *Control of morphology and function of low band gap polymer–bis-fullerene mixed heterojunctions in organic photovoltaics with selective solvent vapor annealing.* Journal of Materials Chemistry A, 2014. **2**(25): p. 9883-9890.
26. Chen, H., Y.C. Hsiao, B. Hu, and M. Dadmun, *Tuning the Morphology and Performance of Low Bandgap Polymer: Fullerene Heterojunctions via*

Solvent Annealing in Selective Solvents. Advanced Functional Materials, 2014. **24**(32): p. 5129-5136.
27. Yin, W. and M. Dadmun, *A New Model for the Morphology of P3HT/PCBM Organic Photovoltaics from Small-Angle Neutron Scattering: Rivers and Streams.* ACS Nano, 2011. **5**(6): p. 4756-4768.
28. Schmidt-Hansberg, B., M. Sanyal, M.F. Klein, M. Pfaff, N. Schnabel, S. Jaiser, A. Vorobiev, E. Müller, A. Colsmann, and P. Scharfer, *Moving through the phase diagram: morphology formation in solution cast polymer–fullerene blend films for organic solar cells.* Acs Nano, 2011. **5**(11): p. 8579-8590.
29. Zhao, J., A. Swinnen, G. Van Assche, J. Manca, D. Vanderzande, and B.V. Mele, *Phase diagram of P3HT/PCBM blends and its implication for the stability of morphology.* The Journal of Physical Chemistry B, 2009. **113**(6): p. 1587-1591.
30. Liao, H.-C., C.-S. Tsao, Y.-T. Shao, S.-Y. Chang, Y.-C. Huang, C.-M. Chuang, T.-H. Lin, C.-Y. Chen, C.-J. Su, and U.-S. Jeng, *Bi-hierarchical nanostructures of donor–acceptor copolymer and fullerene for high efficient bulk heterojunction solar cells.* Energy & Environmental Science, 2013. **6**(6): p. 1938-1948.
31. Scharsich, C., R.H. Lohwasser, M. Sommer, U. Asawapirom, U. Scherf, M. Thelakkat, D. Neher, and A. Köhler, *Control of aggregate formation in poly (3-hexylthiophene) by solvent, molecular weight, and synthetic method.* Journal of Polymer Science Part B: Polymer Physics, 2012. **50**(6): p. 442-453.
32. Wu, W.-R., U.-S. Jeng, C.-J. Su, K.-H. Wei, M.-S. Su, M.-Y. Chiu, C.-Y. Chen, W.-B. Su, C.-H. Su, and A.-C. Su, *Competition between fullerene aggregation and poly (3-hexylthiophene) crystallization upon annealing of bulk heterojunction solar cells.* Acs Nano, 2011. **5**(8): p. 6233-6243.
33. Bundgaard, E. and F.C. Krebs, *Low band gap polymers for organic photovoltaics.* Solar Energy Materials and Solar Cells, 2007. **91**(11): p. 954-985.
34. Dang, M.T., G. Wantz, H. Bejbouji, M. Urien, O.J. Dautel, L. Vignau, and L. Hirsch, *Polymeric solar cells based on P3HT: PCBM: Role of the casting solvent.* Solar Energy Materials and Solar Cells, 2011. **95**(12): p. 3408-3418.
35. Kim, D.H., J. Mei, A.L. Ayzner, K. Schmidt, G. Giri, A.L. Appleton, M.F. Toney, and Z. Bao, *Sequentially solution-processed, nanostructured polymer photovoltaics using selective solvents.* Energy & Environmental Science, 2014.
36. Lee, J.K., W.L. Ma, C.J. Brabec, J. Yuen, J.S. Moon, J.Y. Kim, K. Lee, G.C. Bazan, and A.J. Heeger, *Processing additives for improved efficiency from*

bulk heterojunction solar cells. Journal of the American Chemical Society, 2008. **130**(11): p. 3619-3623.
37. van Bavel, S.S., M. Bärenklau, G. de With, H. Hoppe, and J. Loos, *P3HT/PCBM Bulk Heterojunction Solar Cells: Impact of Blend Composition and 3D Morphology on Device Performance.* Advanced Functional Materials, 2010. **20**(9): p. 1458-1463.
38. Chen, F.-C., C.-J. Ko, J.-L. Wu, and W.-C. Chen, *Morphological study of P3HT:PCBM blend films prepared through solvent annealing for solar cell applications.* Solar Energy Materials and Solar Cells, 2010. **94**(12): p. 2426-2430.
39. Tang, H., G. Lu, L. Li, J. Li, Y. Wang, and X. Yang, *Precise construction of PCBM aggregates for polymer solar cells via multi-step controlled solvent vapor annealing.* Journal of Materials Chemistry, 2010. **20**(4): p. 683-688.
40. Brédas, J., *Relationship between band gap and bond length alternation in organic conjugated polymers.* The Journal of chemical physics, 1985. **82**(8): p. 3808-3811.
41. Zhang, Z.G. and J. Wang, *Structures and properties of conjugated Donor–Acceptor copolymers for solar cell applications.* Journal of Materials Chemistry, 2012. **22**(10): p. 4178-4187.
42. Zhang, Q.T. and J.M. Tour, *Alternating Donor/Acceptor Repeat Units in Polythiophenes. Intramolecular Charge Transfer for Reducing Band Gaps in Fully Substituted Conjugated Polymers.* Journal of the American Chemical Society, 1998. **120**(22): p. 5355-5362.
43. Zhang, Y., S.K. Hau, H.-L. Yip, Y. Sun, O. Acton, and A.K.-Y. Jen, *Efficient polymer solar cells based on the copolymers of benzodithiophene and thienopyrroledione.* Chemistry of Materials, 2010. **22**(9): p. 2696-2698.
44. Hou, J., H.-Y. Chen, S. Zhang, R.I. Chen, Y. Yang, Y. Wu, and G. Li, *Synthesis of a low band gap polymer and its application in highly efficient polymer solar cells.* Journal of the American Chemical Society, 2009. **131**(43): p. 15586-15587.
45. He, Z., C. Zhong, X. Huang, W.Y. Wong, H. Wu, L. Chen, S. Su, and Y. Cao, *Simultaneous enhancement of open-circuit voltage, short-circuit current density, and fill factor in polymer solar cells.* Advanced Materials, 2011. **23**(40): p. 4636-4643.
46. He, Z., C. Zhong, S. Su, M. Xu, H. Wu, and Y. Cao, *Enhanced power-conversion efficiency in polymer solar cells using an inverted device structure.* Nat Photon, 2012. **6**(9): p. 591-595.
47. Pan, H., Y. Li, Y. Wu, P. Liu, B.S. Ong, S. Zhu, and G. Xu, *Low-Temperature, Solution-Processed, High-Mobility Polymer Semiconductors*

for Thin-Film Transistors. Journal of the American Chemical Society, 2007. **129**(14): p. 4112-4113.
48. Laquindanum, J.G., H.E. Katz, A.J. Lovinger, and A. Dodabalapur, *Benzodithiophene rings as semiconductor building blocks.* Advanced Materials, 1997. **9**(1): p. 36-39.
49. Pron, A., P. Berrouard, and M. Leclerc, *Thieno [3, 4-c] pyrrole-4, 6-dione-Based Polymers for Optoelectronic Applications.* Macromolecular Chemistry and Physics, 2013. **214**(1): p. 7-16.
50. Zou, Y., A. Najari, P. Berrouard, S. Beaupré, B. Réda Aïch, Y. Tao, and M. Leclerc, *A Thieno[3,4-c]pyrrole-4,6-dione-Based Copolymer for Efficient Solar Cells.* Journal of the American Chemical Society, 2010. **132**(15): p. 5330-5331.
51. Li, Z., S.W. Tsang, X. Du, L. Scoles, G. Robertson, Y. Zhang, F. Toll, Y. Tao, J. Lu, and J. Ding, *Alternating Copolymers of Cyclopenta [2, 1-b; 3, 4-b'] dithiophene and Thieno [3, 4-c] pyrrole-4, 6-dione for High-Performance Polymer Solar Cells.* Advanced Functional Materials, 2011. **21**(17): p. 3331-3336.
52. Chu, T.-Y., J. Lu, S. Beaupré, Y. Zhang, J.-R. Pouliot, S. Wakim, J. Zhou, M. Leclerc, Z. Li, and J. Ding, *Bulk heterojunction solar cells using thieno [3, 4-c] pyrrole-4, 6-dione and dithieno [3, 2-b: 2', 3'-d] silole copolymer with a power conversion efficiency of 7.3%.* Journal of the American Chemical Society, 2011. **133**(12): p. 4250-4253.
53. Chen, H.-C., Y.-H. Chen, C.-C. Liu, Y.-C. Chien, S.-W. Chou, and P.-T. Chou, *Prominent short-circuit currents of fluorinated quinoxaline-based copolymer solar cells with a power conversion efficiency of 8.0%.* Chemistry of Materials, 2012. **24**(24): p. 4766-4772.
54. Zhang, Y., J. Zou, H.-L. Yip, Y. Sun, J.A. Davies, K.-S. Chen, O. Acton, and A.K.-Y. Jen, *Conjugated polymers based on C, Si and N-bridged dithiophene and thienopyrroledione units: synthesis, field-effect transistors and bulk heterojunction polymer solar cells.* Journal of Materials Chemistry, 2011. **21**(11): p. 3895-3902.
55. Yuan, M.-C., M.-Y. Chiu, S.-P. Liu, C.-M. Chen, and K.-H. Wei, *A Thieno [3, 4-c] pyrrole-4, 6-dione-Based Donor− Acceptor Polymer Exhibiting High Crystallinity for Photovoltaic Applications.* Macromolecules, 2010. **43**(17): p. 6936-6938.
56. Wu, Y., Y. Jing, X. Guo, S. Zhang, M. Zhang, L. Huo, and J. Hou, *A thieno [3, 4-f] isoindole-5, 7-dione based copolymer for polymer solar cells.* Polymer Chemistry, 2013. **4**(3): p. 536-541.
57. Owczarczyk, Z.R., W.A. Braunecker, S.D. Oosterhout, N. Kopidakis, R.E. Larsen, D.S. Ginley, and D.C. Olson, *Cyclopenta [c] thiophene-4,*

6-dione-Based Copolymers as Organic Photovoltaic Donor Materials. Advanced Energy Materials, 2014.
58. Szarko, J.M., J. Guo, Y. Liang, B. Lee, B.S. Rolczynski, J. Strzalka, T. Xu, S. Loser, T.J. Marks, and L. Yu, *When function follows form: effects of donor copolymer side chains on film morphology and BHJ solar cell performance.* Advanced Materials, 2010. **22**(48): p. 5468-5472.
59. Gadisa, A., W.D. Oosterbaan, K. Vandewal, J.C. Bolsée, S. Bertho, J. D'Haen, L. Lutsen, D. Vanderzande, and J.V. Manca, *Effect of Alkyl Side-Chain Length on Photovoltaic Properties of Poly (3-alkylthiophene)/PCBM Bulk Heterojunctions.* Advanced Functional Materials, 2009. **19**(20): p. 3300-3306.
60. Yang, L., H. Zhou, and W. You, *Quantitatively analyzing the influence of side chains on photovoltaic properties of polymer− fullerene solar cells.* The Journal of Physical Chemistry C, 2010. **114**(39): p. 16793-16800.
61. Wu, Q., M. Wang, X. Qiao, Y. Xiong, Y. Huang, X. Gao, and H. Li, *Thieno [3, 4-c] pyrrole-4, 6-dione Containing Copolymers for High Performance Field-Effect Transistors.* Macromolecules, 2013. **46**(10): p. 3887-3894.
62. Shi, Q., H. Fan, Y. Liu, W. Hu, Y. Li, and X. Zhan, *A copolymer of benzodithiophene with TIPS side chains for enhanced photovoltaic performance.* Macromolecules, 2011. **44**(23): p. 9173-9179.
63. Chen, H., J. Peet, Y.-C. Hsiao, B. Hu, and M. Dadmun, *The Impact of Fullerene Structure on Its Miscibility with P3HT and Its Correlation of Performance in Organic Photovoltaics.* Chemistry of Materials, 2014. **26**(13): p. 3993-4003.
64. Debye, P., H. Anderson Jr, and H. Brumberger, *Scattering by an inhomogeneous solid. II. The correlation function and its application.* Journal of applied Physics, 1957. **28**(6): p. 679-683.
65. Debye, P. and A. Bueche, *Scattering by an inhomogeneous solid.* Journal of Applied Physics, 1949. **20**(6): p. 518-525.
66. Lee, C.S. and M.D. Dadmun, *Important thermodynamic characteristics of poly (3-hexyl thiophene).* Polymer, 2014. **55**(1): p. 4-7.
67. Blouin, N., A. Michaud, D. Gendron, S. Wakim, E. Blair, R. Neagu-Plesu, M. Belletete, G. Durocher, Y. Tao, and M. Leclerc, *Toward a rational design of poly (2, 7-carbazole) derivatives for solar cells.* Journal of the American Chemical Society, 2008. **130**(2): p. 732-742.
68. Brandrup, J.I., E. H.; Grulke, E. A.; Bloch, D., 1999.
69. Debye, P., H. Anderson Jr, and H. Brumberger, *Scattering by an inhomogeneous solid. II. The correlation function and its application.* Journal of applied Physics, 2004. **28**(6): p. 679-683.

70. Braunecker, W.A., Z.R. Owczarczyk, A. Garcia, N. Kopidakis, R.E. Larsen, S.R. Hammond, D.S. Ginley, and D.C. Olson, *Benzodithiophene and Imide-Based Copolymers for Photovoltaic Applications.* Chemistry of Materials, 2012. **24**(7): p. 1346-1356.
71. Chen, H., R. Hegde, J. Browning, and M.D. Dadmun, *The miscibility and depth profile of PCBM in P3HT: thermodynamic information to improve organic photovoltaics.* Physical Chemistry Chemical Physics, 2012. **14**(16): p. 5635-5641.
72. Kim, Y., S. Cook, S.M. Tuladhar, S.A. Choulis, J. Nelson, J.R. Durrant, D.D. Bradley, M. Giles, I. McCulloch, and C.-S. Ha, *A strong regioregularity effect in self-organizing conjugated polymer films and high-efficiency polythiophene: fullerene solar cells.* Nature Materials, 2006. **5**(3): p. 197-203.
73. Al-Ibrahim, M., O. Ambacher, S. Sensfuss, and G. Gobsch, *Effects of solvent and annealing on the improved performance of solar cells based on poly (3-hexylthiophene): fullerene.* Applied Physics Letters, 2005. **86**(20): p. 201120.
74. Park, J.H., J.S. Kim, J.H. Lee, W.H. Lee, and K. Cho, *Effect of annealing solvent solubility on the performance of poly (3-hexylthiophene)/methanofullerene solar cells.* The Journal of Physical Chemistry C, 2009. **113**(40): p. 17579-17584.
75. Peet, J., J. Kim, N.E. Coates, W.L. Ma, D. Moses, A.J. Heeger, and G.C. Bazan, *Efficiency enhancement in low-bandgap polymer solar cells by processing with alkane dithiols.* Nature materials, 2007. **6**(7): p. 497-500.
76. Gu, Y., C. Wang, and T.P. Russell, *Multi-Length-Scale Morphologies in PCPDTBT/PCBM Bulk-Heterojunction Solar Cells.* Advanced Energy Materials, 2012. **2**(6): p. 683-690.
77. Wang, T., A.J. Pearson, A.D. Dunbar, P.A. Staniec, D.C. Watters, H. Yi, A.J. Ryan, R.A. Jones, A. Iraqi, and D.G. Lidzey, *Correlating structure with function in thermally annealed PCDTBT: PC70BM photovoltaic blends.* Advanced Functional Materials, 2012. **22**(7): p. 1399-1408.
78. Beiley, Z.M., E.T. Hoke, R. Noriega, J. Dacuña, G.F. Burkhard, J.A. Bartelt, A. Salleo, M.F. Toney, and M.D. McGehee, *Morphology-Dependent Trap Formation in High Performance Polymer Bulk Heterojunction Solar Cells.* Advanced Energy Materials, 2011. **1**(5): p. 954-962.
79. Bartelt, J.A., Z.M. Beiley, E.T. Hoke, W.R. Mateker, J.D. Douglas, B.A. Collins, J.R. Tumbleston, K.R. Graham, A. Amassian, and H. Ade, *The importance of fullerene percolation in the mixed regions of polymer–fullerene bulk heterojunction solar cells.* Advanced Energy Materials, 2013. **3**(3): p. 364-374.

80. Chen, H., S. Hu, H. Zang, B. Hu, and M. Dadmun, *Precise structural development and its correlation to function in conjugated polymer: fullerene thin films by controlled solvent annealing.* Advanced Functional Materials, 2013. **23**(13): p. 1701-1710.
81. J.Krank, *The mathematics of diffusion*, 1973.
82. Kim, Y., A.M. Ballantyne, J. Nelson, and D.D. Bradley, *Effects of thickness and thermal annealing of the PEDOT: PSS layer on the performance of polymer solar cells.* Organic Electronics, 2009. **10**(1): p. 205-209.
83. Kirchmeyer, S. and K. Reuter, *Scientific importance, properties and growing applications of poly (3, 4-ethylenedioxythiophene).* Journal of Materials Chemistry, 2005. **15**(21): p. 2077-2088.
84. Möller, S., C. Perlov, W. Jackson, C. Taussig, and S.R. Forrest, *A polymer/semiconductor write-once read-many-times memory.* Nature, 2003. **426**(6963): p. 166-169.
85. Collazos-Castro, J.E., J.L. Polo, G.R. Hernández-Labrado, V. Padial-Cañete, and C. García-Rama, *Bioelectrochemical control of neural cell development on conducting polymers.* Biomaterials, 2010. **31**(35): p. 9244-9255.
86. Cao, Y., G. Yu, C. Zhang, R. Menon, and A. Heeger, *Polymer light-emitting diodes with polyethylene dioxythiophene–polystyrene sulfonate as the transparent anode.* Synthetic Metals, 1997. **87**(2): p. 171-174.
87. Ouyang, J., C.W. Chu, F.C. Chen, Q. Xu, and Y. Yang, *High-Conductivity Poly (3, 4-ethylenedioxythiophene): Poly (styrene sulfonate) Film and Its Application in Polymer Optoelectronic Devices.* Advanced Functional Materials, 2005. **15**(2): p. 203-208.
88. Hwang, J., F. Amy, and A. Kahn, *Spectroscopic study on sputtered PEDOT· PSS: Role of surface PSS layer.* Organic electronics, 2006. **7**(5): p. 387-396.
89. Greczynski, G., T. Kugler, and W. Salaneck, *Characterization of the PEDOT-PSS system by means of X-ray and ultraviolet photoelectron spectroscopy.* Thin Solid Films, 1999. **354**(1): p. 129-135.
90. Kemerink, M., S. Timpanaro, M. De Kok, E. Meulenkamp, and F. Touwslager, *Three-dimensional inhomogeneities in PEDOT: PSS films.* The Journal of Physical Chemistry B, 2004. **108**(49): p. 18820-18825.
91. Crispin, X., S. Marciniak, W. Osikowicz, G. Zotti, A. van der Gon, F. Louwet, M. Fahlman, L. Groenendaal, F. De Schryver, and W.R. Salaneck, *Conductivity, morphology, interfacial chemistry, and stability of poly (3, 4-ethylene dioxythiophene)–poly (styrene sulfonate): A photoelectron spectroscopy study.* Journal of Polymer Science Part B: Polymer Physics, 2003. **41**(21): p. 2561-2583.
92. Nardes, A.M., M. Kemerink, R.A. Janssen, J.A. Bastiaansen, N.M. Kiggen, B.M. Langeveld, A.J. van Breemen, and M.M. de Kok, *Microscopic*

understanding of the anisotropic conductivity of PEDOT: PSS thin films. Advanced Materials, 2007. **19**(9): p. 1196-1200.
93. Nardes, A.M., R.A. Janssen, and M. Kemerink, *A Morphological Model for the Solvent-Enhanced Conductivity of PEDOT: PSS Thin Films.* Advanced Functional Materials, 2008. **18**(6): p. 865-871.
94. Takano, T., H. Masunaga, A. Fujiwara, H. Okuzaki, and T. Sasaki, *PEDOT nanocrystal in highly conductive PEDOT: PSS polymer films.* Macromolecules, 2012. **45**(9): p. 3859-3865.
95. Jukes, P.C., S.J. Martin, A.M. Higgins, M. Geoghegan, R.A. Jones, S. Langridge, A. Wehrum, and S. Kirchmeyer, *Controlling the Surface Composition of Poly (3, 4-ethylene dioxythiophene)–Poly (styrene sulfonate) Blends by Heat Treatment.* Advanced Materials, 2004. **16**(9-10): p. 807-811.
96. Aleshin, A., S. Williams, and A. Heeger, *Transport properties of poly (3, 4-ethylenedioxythiophene)/poly (styrenesulfonate).* Synthetic Metals, 1998. **94**(2): p. 173-177.
97. van de Ruit, K., R.I. Cohen, D. Bollen, T. van Mol, R. Yerushalmi-Rozen, R.A. Janssen, and M. Kemerink, *Quasi-One Dimensional in-Plane Conductivity in Filamentary Films of PEDOT: PSS.* Advanced Functional Materials, 2013. **23**(46): p. 5778-5786.
98. van de Ruit, K., I. Katsouras, D. Bollen, T. van Mol, R.A. Janssen, D.M. de Leeuw, and M. Kemerink, *The Curious Out-of-Plane Conductivity of PEDOT: PSS.* Advanced Functional Materials, 2013. **23**(46): p. 5787-5793.
99. Nardes, A.M., M. Kemerink, M. De Kok, E. Vinken, K. Maturova, and R. Janssen, *Conductivity, work function, and environmental stability of PEDOT: PSS thin films treated with sorbitol.* Organic Electronics, 2008. **9**(5): p. 727-734.
100. Han, Y. and Y. Lu, *Preparation and characterization of exfoliated organic montmorillonite/poly (3, 4-ethyldioxythiophene) nanocomposites.* Journal of Applied Polymer Science, 2009. **111**(5): p. 2400-2407.
101. Kuila, B.K. and A.K. Nandi, *Physical, mechanical, and conductivity properties of poly (3-hexylthiophene)-montmorillonite clay nanocomposites produced by the solvent casting method.* Macromolecules, 2004. **37**(23): p. 8577-8584.
102. Ma, J., J. Xu, J.-H. Ren, Z.-Z. Yu, and Y.-W. Mai, *A new approach to polymer/montmorillonite nanocomposites.* Polymer, 2003. **44**(16): p. 4619-4624.
103. Dasari, A., Z.-Z. Yu, Y.-W. Mai, and S. Liu, *Flame retardancy of highly filled polyamide 6/clay nanocomposites.* Nanotechnology, 2007. **18**(44): p. 445602.

104. Priolo, M.A., K.M. Holder, D. Gamboa, and J.C. Grunlan, *Influence of clay concentration on the gas barrier of clay–polymer nanobrick wall thin film assemblies.* Langmuir, 2011. **27**(19): p. 12106-12114.
105. Priolo, M.A., D. Gamboa, K.M. Holder, and J.C. Grunlan, *Super gas barrier of transparent polymer− clay multilayer ultrathin films.* Nano letters, 2010. **10**(12): p. 4970-4974.
106. Grunlan, J.C., A. Grigorian, C.B. Hamilton, and A.R. Mehrabi, *Effect of clay concentration on the oxygen permeability and optical properties of a modified poly (vinyl alcohol).* Journal of applied polymer science, 2004. **93**(3): p. 1102-1109.
107. Li, Y.-C., J. Schulz, S. Mannen, C. Delhom, B. Condon, S. Chang, M. Zammarano, and J.C. Grunlan, *Flame retardant behavior of polyelectrolyte− clay thin film assemblies on cotton fabric.* Acs Nano, 2010. **4**(6): p. 3325-3337.
108. Gopakumar, T., J. Lee, M. Kontopoulou, and J. Parent, *Influence of clay exfoliation on the physical properties of montmorillonite/polyethylene composites.* Polymer, 2002. **43**(20): p. 5483-5491.
109. Lan, T. and T.J. Pinnavaia, *Clay-reinforced epoxy nanocomposites.* Chemistry of Materials, 1994. **6**(12): p. 2216-2219.
110. Secor, R. and C. Radke, *Spillover of the diffuse double layer on montmorillonite particles.* Journal of colloid and Interface Science, 1985. **103**(1): p. 237-244.
111. Cadene, A., S. Durand-Vidal, P. Turq, and J. Brendle, *Study of individual Na-montmorillonite particles size, morphology, and apparent charge.* Journal of Colloid and Interface Science, 2005. **285**(2): p. 719-730.
112. *Clay*.
113. Stöcker, T., A. Köhler, and R. Moos, *Why does the electrical conductivity in PEDOT: PSS decrease with PSS content? A study combining thermoelectric measurements with impedance spectroscopy.* Journal of polymer science part B: polymer physics, 2012. **50**(14): p. 976-983.
114. Yin, X., K. Kobayashi, K. Yoshino, H. Yamamoto, T. Watanuki, and I. Isa, *Percolation conduction in polymer composites containing polypyrrole coated insulating polymer fiber and conducting polymer*. Synthetic Metals, 1995. **69**(1): p. 367-368.
115. Hamaide, T. and C. Le Deore, *Cationic conductivity and relaxation processes in solid polymer electrolytes with lithium perfluoroalkyl sulfonate or sulfonato end-capped poly (ethylene oxide).* Polymer, 1993. **34**(5): p. 1038-1046.

116. Bidadi, H., P. Schroeder, and T.J. Pinnavaia, *Dielectric properties of montmorillonite clay films: Effects of water and layer charge reduction.* Journal of Physics and Chemistry of Solids, 1988. **49**(12): p. 1435-1440.
117. Hernández-Labrado, G., R. Contreras-Donayre, J. Collazos-Castro, and J. Polo, *Subdiffusion behavior in poly (3, 4-ethylenedioxythiophene): polystyrene sulfonate (PEDOT: PSS) evidenced by electrochemical impedance spectroscopy.* Journal of Electroanalytical Chemistry, 2011. **659**(2): p. 201-204.
118. Rizvi, T.Z. and A. Shakoor, *Electrical conductivity and dielectric properties of polypyrrole/Na+–montmorillonite (PPy/Na+–MMT) clay nanocomposites.* Journal of Physics D: Applied Physics, 2009. **42**(9): p. 095415.
119. Arroyo, M., M. Lopez-Manchado, and B. Herrero, *Organo-montmorillonite as substitute of carbon black in natural rubber compounds.* Polymer, 2003. **44**(8): p. 2447-2453.
120. Kawano, K., R. Pacios, D. Poplavskyy, J. Nelson, D.D. Bradley, and J.R. Durrant, *Degradation of organic solar cells due to air exposure.* Solar energy materials and solar cells, 2006. **90**(20): p. 3520-3530.
121. Kim, J.K., H.S. Park, D.K. Rhee, S.-J. Ham, K.-J. Lee, P.J. Yoo, and J.H. Park, *Ultrathin nanoclay films with tunable thickness as barrier layers in organic light emitting devices.* Journal of Materials Chemistry, 2012. **22**(16): p. 7718-7723.
122. Kuş, M. and S. Okur, *Electrical characterization of PEDOT: PSS beyond humidity saturation.* Sensors and Actuators B: Chemical, 2009. **143**(1): p. 177-181.
123. Zhou, J., D.H. Anjum, L. Chen, X. Xu, I.A. Ventura, L. Jiang, and G. Lubineau, *The temperature-dependent microstructure of PEDOT/PSS films: insights from morphological, mechanical and electrical analyses.* Journal of Materials Chemistry C, 2014. **2**(46): p. 9903-9910.
124. Atorngitjawat, P., R.J. Klein, and J. Runt, *Dynamics of sulfonated polystyrene copolymers using broadband dielectric spectroscopy.* Macromolecules, 2006. **39**(5): p. 1815-1820.

Appendix

In the images corresponding to small angle neutron scattering (SANS) fit, blue color corresponds to thermally annealed bulk heterojunction (BHJ) sample and maroon color corresponds to as-cast sample.

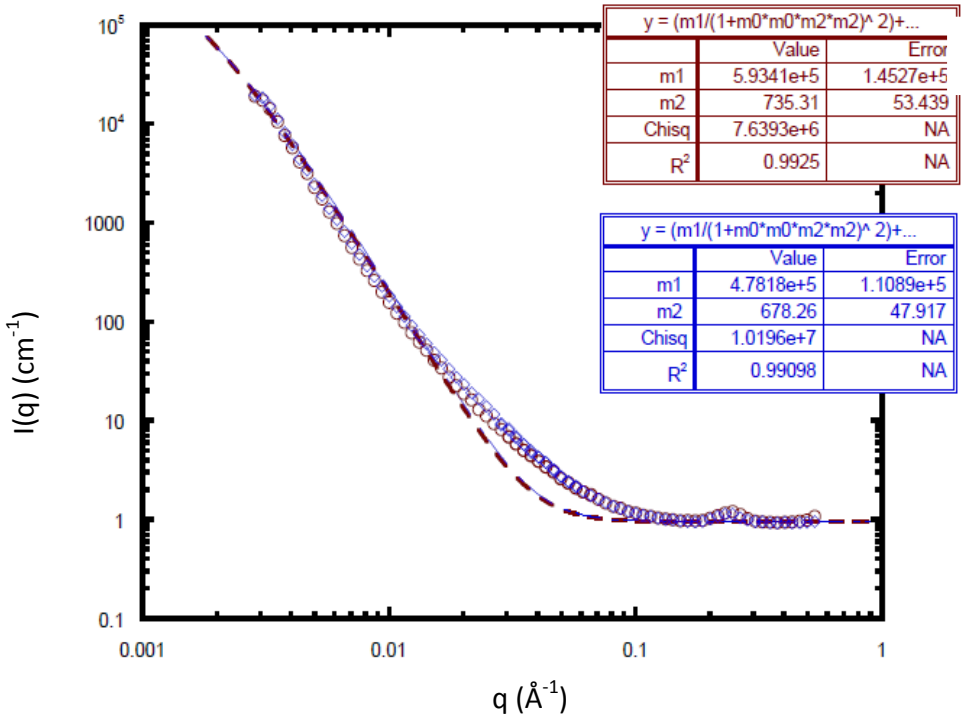


Figure A.1. SANS fit for P-CTD-BBDT(C12) based BHJ at large length scale.

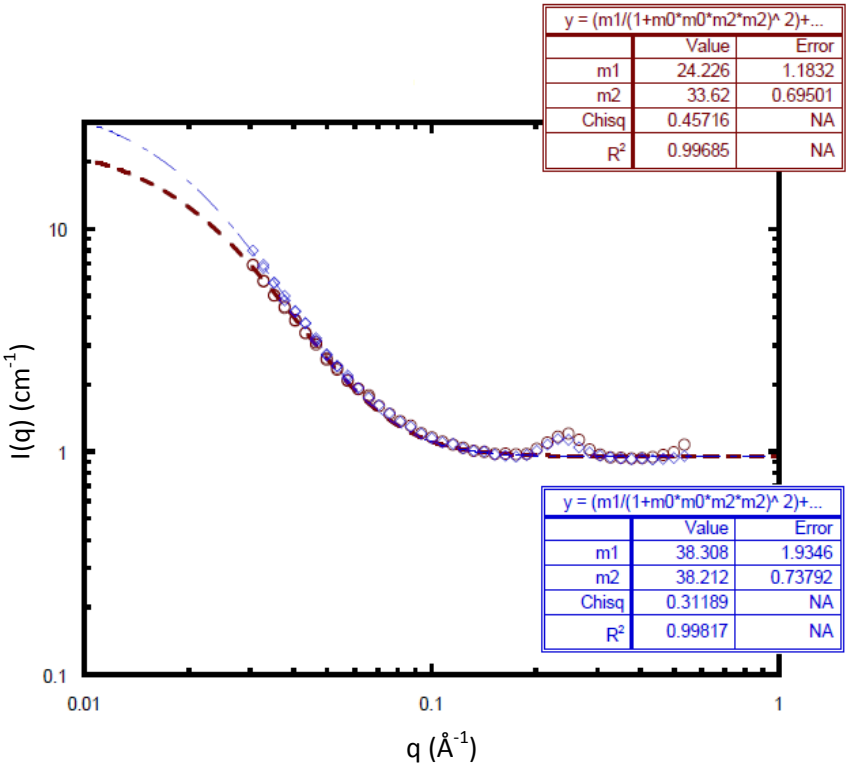


Figure A.2. SANS fit for P-CTD-BBDT(C12) based BHJ at small length scale.

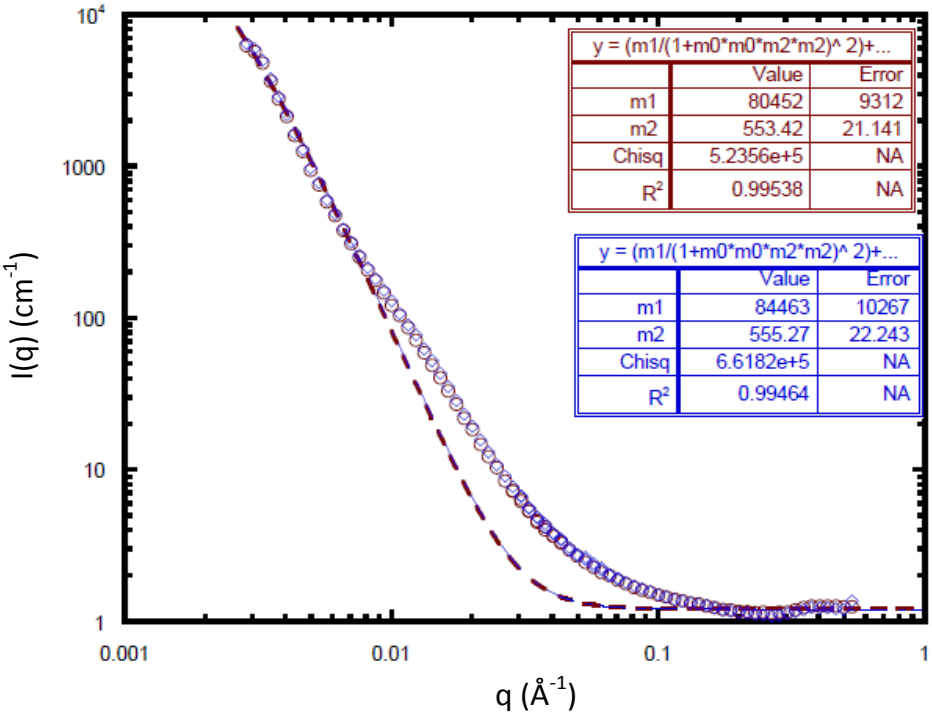


Figure A.3. SANS fit for P-CTD-BBDT(EH) based BHJ at large length scale.

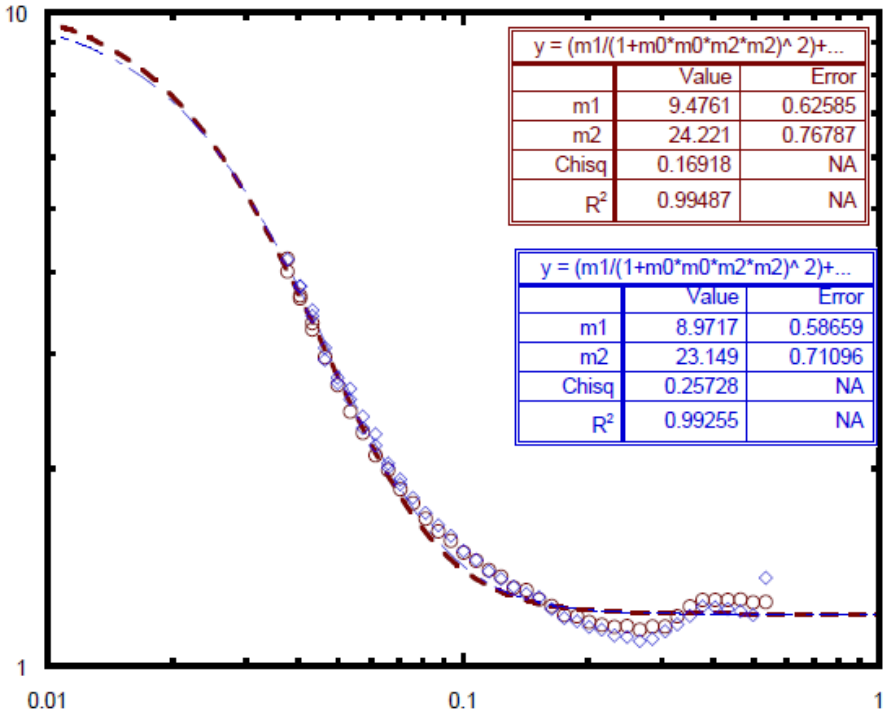


Figure A.4. SANS fit for P-CTD-BBDT(EH) based BHJ at small length scale.

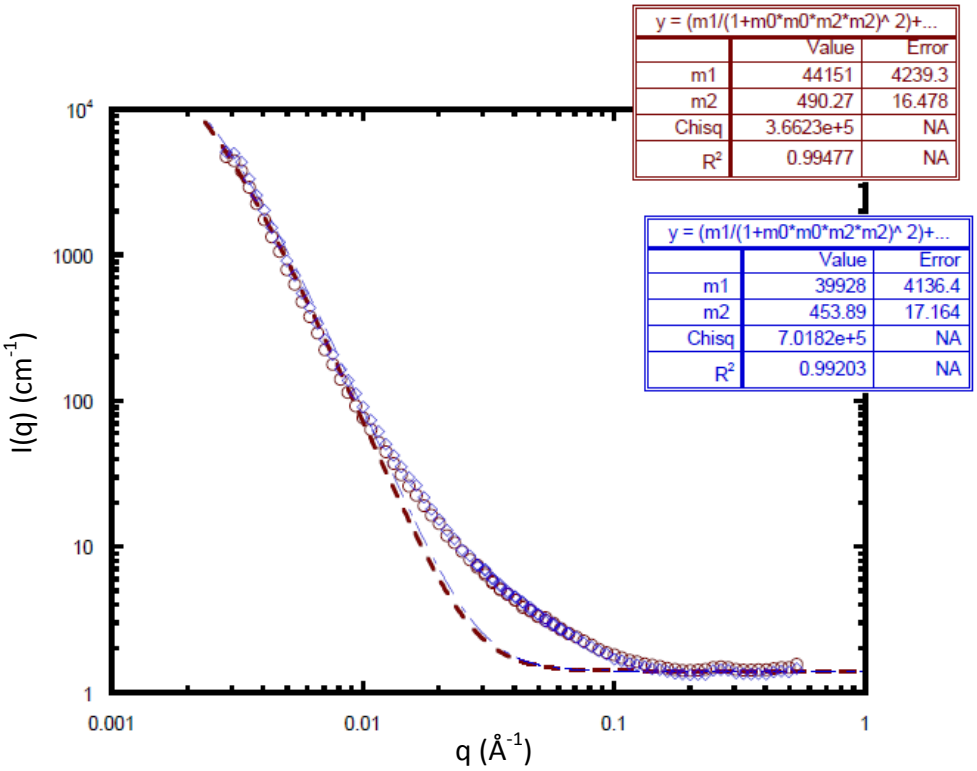


Figure A.5. SANS fit for P-CTD-BDT(C12) based BHJ at large length scale.

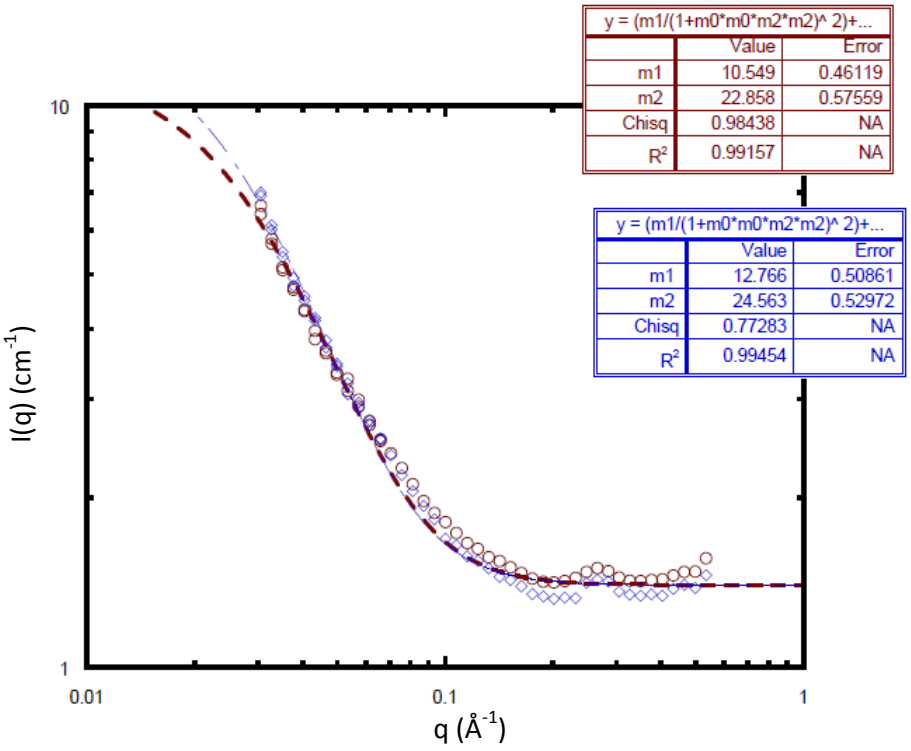


Figure A.6. SANS fit for P-CTD-BDT(C12) based BHJ at small length scale.

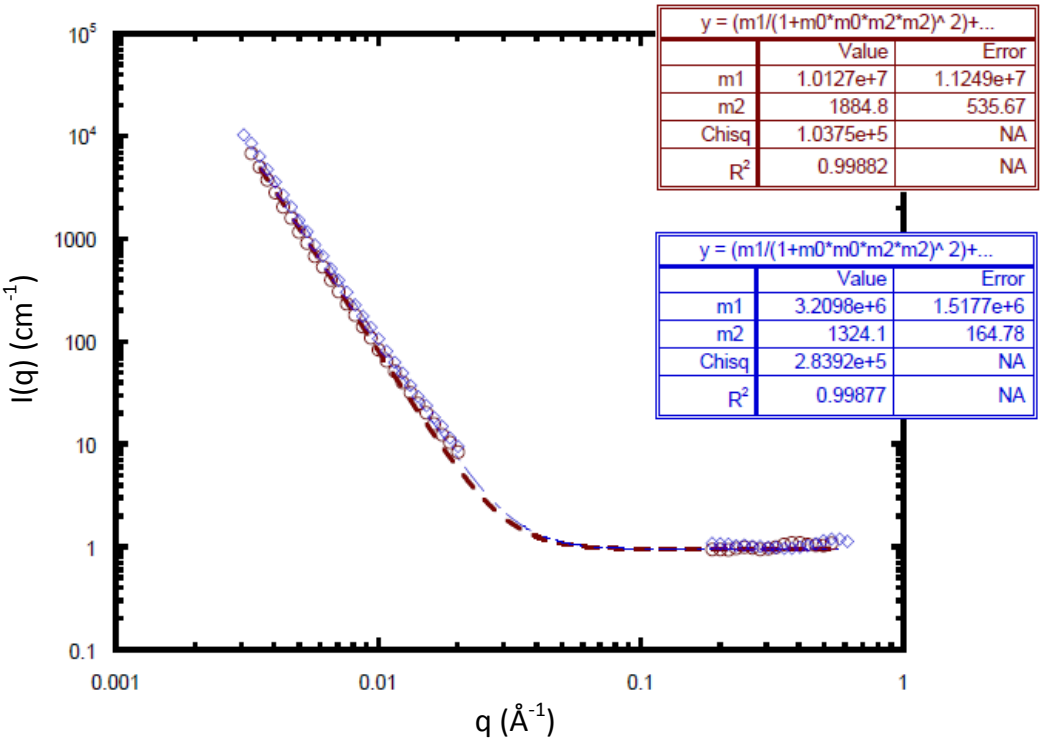


Figure A.7. SANS fit for P-CTD-BDT(EH) based BHJ at large length scale.

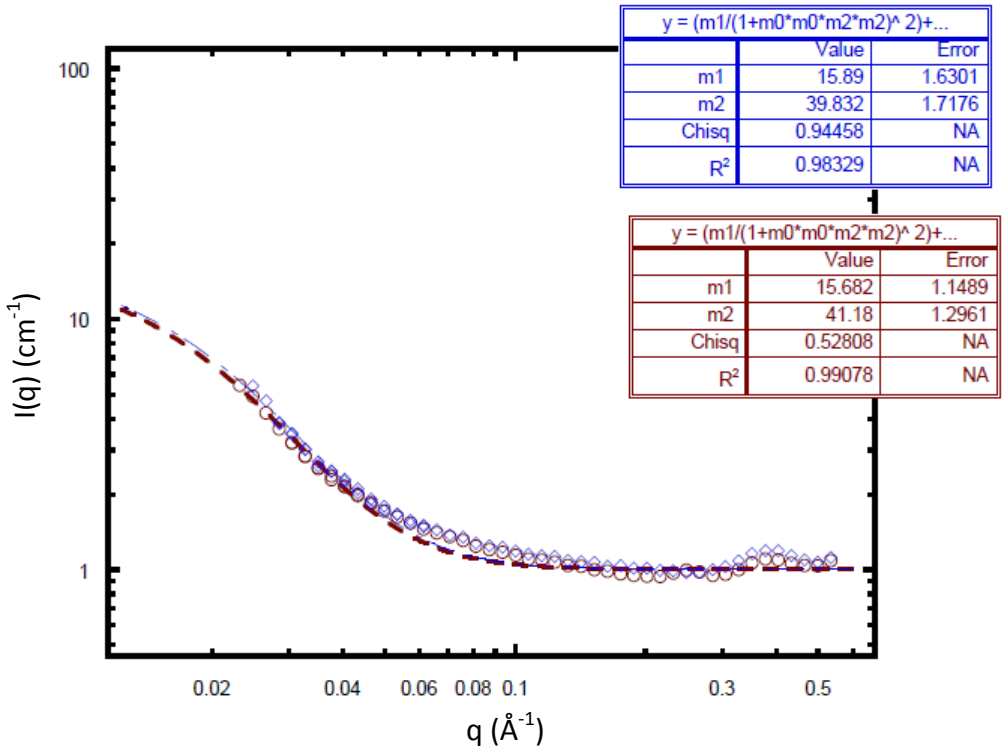


Figure A.8. SANS fit for P-CTD-BDT(EH) based BHJ at small length scale.

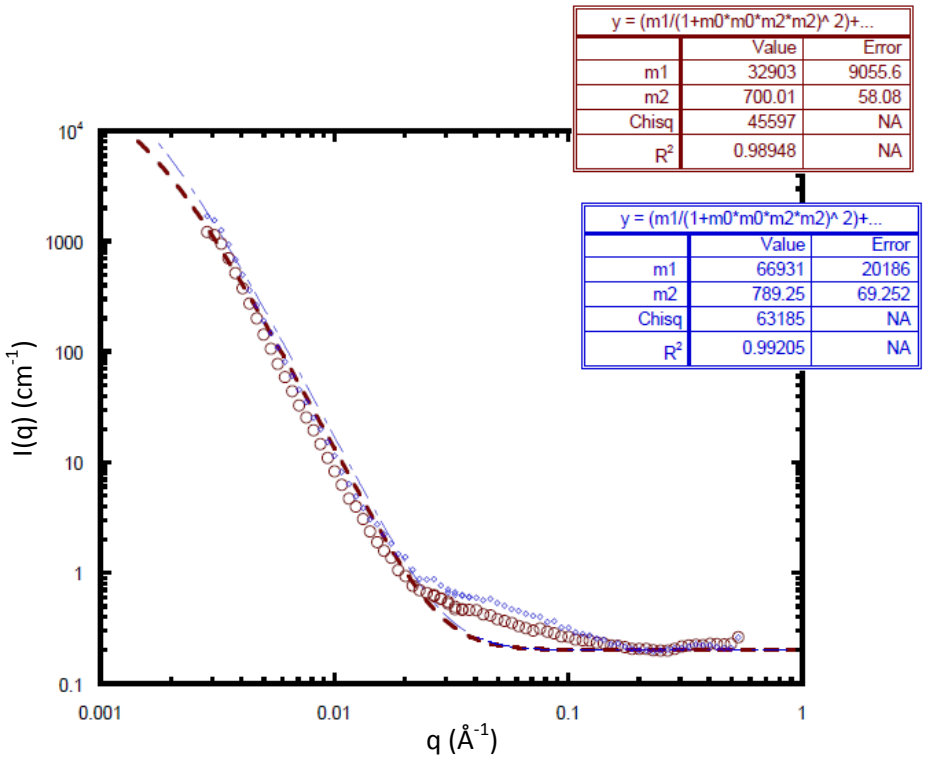


Figure A.9. SANS fit for P-TID-BDT(EH) based BHJ at large length scale.

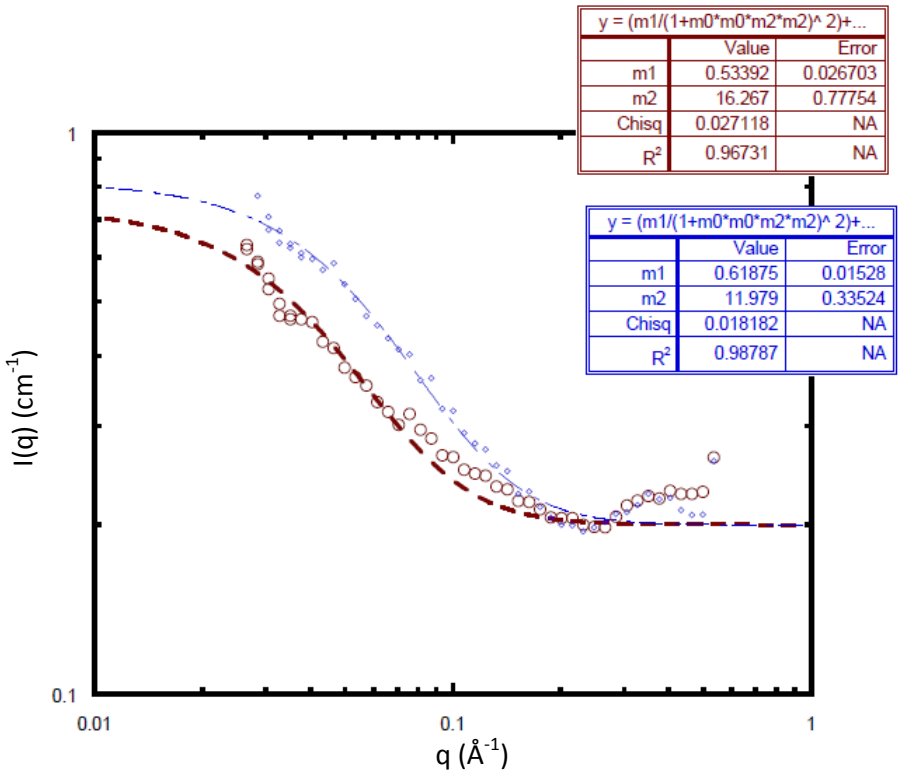


Figure A.10. SANS fit for P-TID-BDT(EH) based BHJ at small length scale.

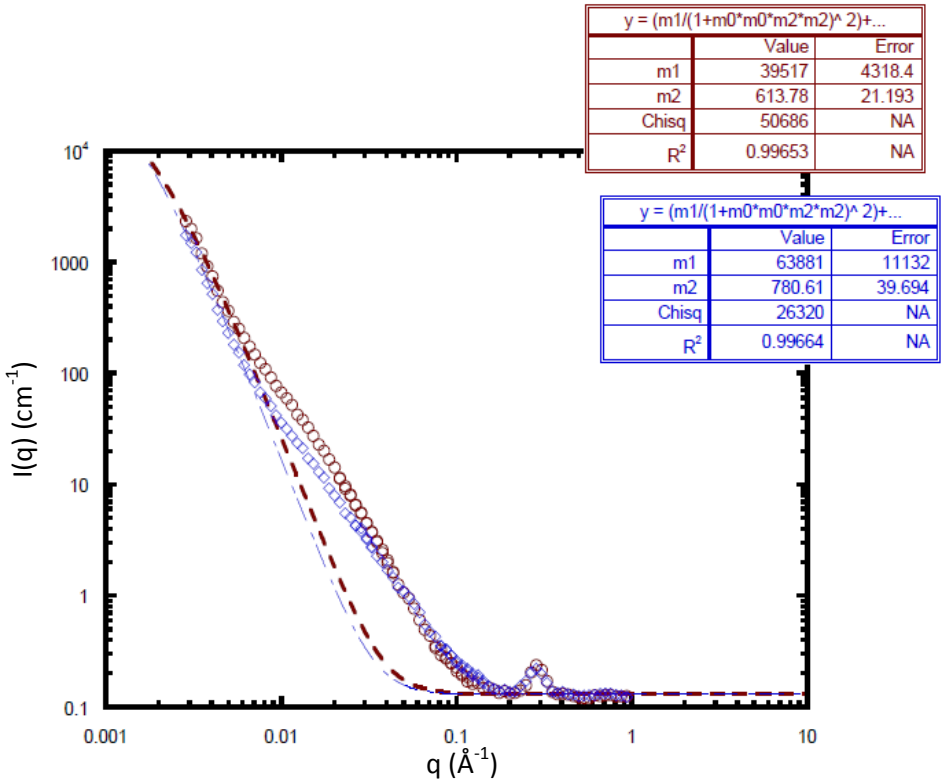


Figure A.11. SANS fit for P-TPD-BDT(EH) based BHJ at large length scale.

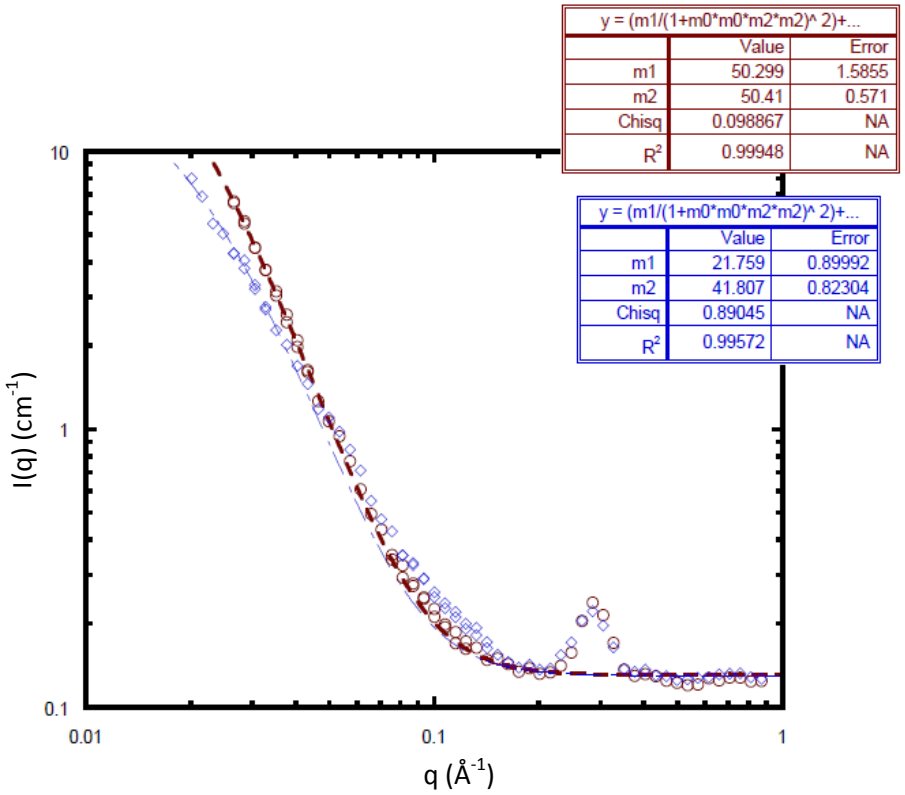


Figure A.12. SANS fit for P-TPD-BDT(EH) based BHJ at small length scale.

VITA

Siddharth Pradhan was born in Bhurkunda, Jharkhand, India to the parents of Mr. Pradip Kumar Pradhan and Mrs. Jayashree Pradhan. He received an undergraduate degree (Bachelor of Technology) in Chemical Engineering from Indian Institute of Technology - Banaras Hindu University, Varanasi, India in May, 2008. Then, he worked in Gold Star, Engineering and Construction for a year as an engineering trainee and got promoted to assistant process engineer. In September 2009, he moved to Cincinnati, USA to pursue Masters degree in Materials Science and Engineering and completed it by May 2012. He worked on graphene oxide and dye-sensitized solar cells. In August 2012, he joined University of Tennessee - Knoxville. He completed his second Masters degree in Chemistry in July 2015. He worked on thin films of polymer composites.